Universidad de Vigo

SPECTRAL SHAPING TECHNIQUES FOR ADVANCED MULTICARRIER COMMUNICATION SYSTEMS

2023 DOCTORAL DISSERTATION
Khawar Hussain

DOCTORAL DISSERTATION

Spectrum Shaping Techniques for Advanced Multicarrier Communication Systems

Author:
Khawar Hussain

Supervisor:
Roberto Lopez-Valcarce

2023

Universidad de Vigo

EIDO
Escola Internacional
de Doutoramento

Universidade Vigo

International Doctoral School

Khawar Hussian

DOCTORAL DISSERTATION

Spectrum Shaping Techniques for Advanced Multicarrier Communication Systems

Supervised by:

Roberto López-Valcarce

2023

Universidade Vigo

International Doctoral School

Roberto López Valcarce,

DECLARES that the present work, entitled "Spectrum Shaping Techniques for Advanced Multicarrier Communication Systems", submitted by Khawar Hussain to obtain the title of Doctor, was carried out under his supervision in the PhD programme "PhD Programme in Information and Communications Technology".

Vigo, 2023.

The supervisor,

LOPEZ VALCARCE ROBERTO - 10082556T

Firmado digitalmente por LOPEZ VALCARCE ROBERTO - 10082556T
Fecha: 2023.05.04 16:40:52 +02'00'

Dr. Roberto López Valcarce

This work is supported by Agencia Estatal de Investigación (Spain) and the European Regional Development Fund (ERDF) under projects WINTER (TEC2016-76409-C2-2-R, BES-2017-080305) and RODIN (PID2019-105717RB-C21), and by Xunta de Galicia (Agrupación Estratéxica Consolidada de Galicia accreditation 2016-2019 and 2020-2023 Grupo de Referencia ED431C2017/53).

UNIÓN EUROPEA

FONDO SOCIAL EUROPEO

"O FSE inviste no teu futuro"

XUNTA DE GALICIA

CONSELLERÍA DE CULTURA, EDUCACIÓN E ORDENACIÓN UNIVERSITARIA

Secretaría Xeral de Universidades

Abstract

Mobile communication has evolved from 1G voice-focused systems to 4G data and mobile broadband services, with the exponential increase in mobile data volume and connected devices leading to the development of the Fifth Generation (5G) mobile network. The 5G network is expected to improve key performance indicators such as data rate, massive connectivity, latency, network reliability, and energy efficiency. To meet these requirements, the 5G air interface must be highly flexible, spectrally efficient, reliable, scalable, and energy-efficient.

Among various waveforms proposed for the 5G radio interface, CP-OFDM was chosen due to its inherent advantages such as robustness to multipath, compatibility with MIMO, low complexity, and high spectral efficiency. However, it suffers from large spectrum sidelobes, peak-to-average-power-ratio, and sensitivity to synchronization errors. The focus of this thesis is on the large spectrum sidelobes of OFDM that cause high out-of-band radiation resulting in adjacent channel interference. Therefore, reducing spectral leakage to adjacent channels is crucial for efficient spectrum utilization.

Numerous techniques for reducing out-of-band radiation (OBR) have been proposed in the literature, each with its advantages and drawbacks. The performance of an OBR reduction technique is not only measured by its ability to suppress out-of-band emission but also by key performance indicators (KPIs) such as computational complexity, spectral efficiency, in-band distortion, and spectrum overshoot. Balancing key performance indicators (KPIs) is crucial when reducing OBR since it typically involves a tradeoff between one or more performance parameters. However, the tradeoffs are not uniform across different OBR reduction techniques. Thus, it is essential to strike a balance between the KPIs to meet the varying requirements of different use-case scenarios.

The thesis presents multiple innovative designs for OBR suppression in multicarrier systems to prevent adjacent channel interference. These designs

offer the flexibility to select a frequency range through a spectral weighting function that prioritizes certain frequencies. Additionally, the proposed designs are adaptable enough to enable tradeoffs among the aforementioned KPIs to fulfill the diverse requirements of various applications and scenarios.

An effective time-domain windowing technique is proposed that that is both effective and simple, and transparent at the receiver. The proposed optimal window design has the flexibility to shape the power spectral density to focus on OBR at the frequency ranges of interest, unlike traditional windowing approaches. Additionally, the design optimizes OBR performance across different frequency regions based on the system's requirements. The thesis also presents novel frequency-domain spectral precoding approaches that can tradeoff between OBR performance and complexity, which is especially of interest for battery-operated or low-power devices. The proposed design allows for control over the amount of distortion on data subcarriers, which is determined by a user-selectable parameter, and influences receiver complexity.

A joint spectral precoding and windowing design is also presented that leverages the advantages of both approaches. By optimizing the precoder and window coefficients to reduce radiated power within a specified frequency range, the design achieves a superior trade-off between out-of-band radiation (OBR), throughput, and complexity compared to using these techniques individually. The results demonstrate the effectiveness of this approach. Finally, the thesis presents memory-based precoding approach to mitigate the issue of large sidelobes. By incorporating memory into the precoder, out-of-band radiation (OBR) performance can be improved without compromising spectral efficiency, albeit at the expense of increased computational complexity. The novel memory-based precoder is designed to minimize the total OBR within a user-defined frequency range. Additionally, this technique enables control over spectral peaks, thereby allowing for flexible OBR levels.

Resumen

La comunicación móvil ha experimentado un tremendo crecimiento en las últimas décadas, desde los sistemas de Primera Generación (1G) que se centraban principalmente en la voz hasta los sistemas de Cuarta Generación (4G), que se desplazaron hacia los datos y los servicios móviles de banda ancha. La evolución hacia la próxima generación es esencial para soportar el aumento masivo y exponencial del uso de datos y la conectividad de un gran número de dispositivos. En consecuencia, se han propuesto redes móviles de Quinta Generación (5G) para atender al crecimiento del tráfico y proporcionar una calidad de servicio mejorada a un enorme número de usuarios finales mediante la construcción de redes rentables.

La red móvil de Quinta Generación (5G) se concibió como un salto revolucionario y para proporcionar mejoras significativas en todos los indicadores clave de rendimiento, es decir, velocidad de datos, conectividad masiva, latencia, confiabilidad de la red y eficiencia energética. La Unión Internacional de Telecomunicaciones (ITU) ha clasificado los servicios ofrecidos por la red 5G principalmente en tres categorías: Banda Ancha Móvil Mejorada (eMBB), Comunicaciones Masivas de Tipo Máquina (mMTC) y Comunicaciones Ultraconfiables de Baja Latencia (URLLC).

La Banda Ancha Móvil Mejorada (eMBB) tiene como objetivo abordar los servicios impulsados por los datos y centrados en el ser humano, proporcionando un rendimiento mejorado en términos de altas velocidades de datos y una experiencia de usuario perfecta para aplicaciones como Realidad Virtual (VR), Realidad Aumentada (AR), aplicaciones basadas en la nube, videos de alta definición y acceso inalámbrico a internet. Las Comunicaciones Ultraconfiables de Baja Latencia (URLLC) imponen requisitos rigurosos en términos de latencia, confiabilidad y disponibilidad para aplicaciones de control en tiempo real y críticas para la misión. Ejemplos de tales aplicaciones incluyen aplicaciones de Internet Táctil, Conducción Automatizada, Cirugía Médica Remota, Seguridad en el Transporte, Robótica Industrial, Protección Pública, Redes Inteligentes, Ayuda en Caso de Desas-

tres y Comunicaciones Vehículo a Vehículo. Las Comunicaciones Masivas de Tipo Máquina (mMTC) atenderán a una gran cantidad de dispositivos de bajo costo con larga duración de batería. Las Ciudades Inteligentes, la Salud, la Manufactura, la Agricultura Inteligente, los Bienes de Consumo, las Comunicaciones Empresariales y el Transporte son algunos ejemplos de aplicaciones mMTC.

La red del futuro ofrecerá servicios para una amplia gama de escenarios y, para admitir eficientemente tales casos de uso diversos, la interfaz de aire 5G debe ser lo suficientemente flexible como para satisfacer los requisitos de los servicios existentes y futuros. Por lo tanto, la interfaz de aire 5G debe ser altamente flexible, robusta, espectralmente eficiente, confiable, escalable y eficiente en términos de energía para cumplir con los requisitos rigurosos de diversas aplicaciones.

En la búsqueda de encontrar la mejor forma de onda para la interfaz de radio 5G, se han propuesto varias formas de onda. Algunas de las principales contendientes para la interfaz de aire 5G incluyen Filter Bank multiportadora (FBMC), Universal Filtered multiportadora (UFMC), Generalized Frequency Division Multiplexing (GFDM) y Cyclic Prefix Orthogonal Frequency Division Multiplexing (CP-OFDM). Además, se estudiaron y sugirieron muchas otras formas de onda para la red 5G, incluyendo Constant Envelope Waveforms, DFT-Spread OFDM (DFT-S-OFDM), Zero-Tail DFT-Spread OFDM, Filtered-OFDM (F-OFDM) y Unique Word (UW-OFDM), por nombrar algunas.

Todas las formas de onda propuestas anteriores para la interfaz de aire 5G tienen sus propias ventajas y desventajas, y cada forma de onda es un formato de modulación preferible para un escenario específico. Sin embargo, se encontró que CP-OFDM era el candidato más apropiado para la interfaz de radio 5G. CP-OFDM mostró un mejor rendimiento en todos los indicadores clave: buena compatibilidad con MIMO, baja complejidad de implementación y alta eficiencia espectral. Está bien localizado en el dominio del tiempo y es más robusto contra el ruido de fase y los efectos Doppler que otras formas de onda multiportadora. Debido a estas ventajas, el Proyecto de Asociación de Tercera Generación (3GPP) acordó el uso de CP-OFDM para la nueva interfaz de radio 5G (5G-NR).

La modulación por división ortogonal de frecuencia (OFDM) es un caso especial de modulación multiportadora (MC) que se remonta a la década de 1960. Con el desarrollo de OFDM a lo largo de los años, se adoptó para el estándar de radiodifusión de audio digital europeo (DAB) y el estándar de televisión terrestre digital de transmisión (DVB). Además, OFDM ha sido utilizado por estándares como IEEE 802.16, IEEE 802.20 y los comités de

Red de Acceso a Radiodifusión (BRAN) del Instituto Europeo de Normas de Telecomunicaciones (ETSI). OFDM también se ha utilizado como técnica de transmisión para redes de área local de alto rendimiento (HIPERLAN) y el estándar de red de área local inalámbrica (WLAN) IEEE 802.11. Además, OFDM es la técnica de señalización para 4G LTE y 5G NR. OFDM también se introdujo en las comunicaciones de línea eléctrica (PLC) para abordar la naturaleza selectiva en frecuencia del canal de línea eléctrica, lo que puede causar una degradación significativa de la señal y bajas tasas de datos. Esto ha llevado a su adopción en estándares como IEEE 1901.2, ITU-T G.9903 y ITU-T G.9960.

OFDM divide toda la banda del canal en muchas bandas estrechas (también llamadas subcanales o subportadoras), las cuales se transmiten en paralelo para mantener una alta tasa de transmisión de datos y al mismo tiempo hacerla robusta contra el desvanecimiento selectivo en frecuencia. Se logra una alta eficiencia espectral al superponer y espaciar las subportadoras más cerca entre sí. Las subportadoras son ortogonales entre sí para evitar la interferencia entre portadoras muy cercanas. El uso del prefijo cíclico (CP) alivia efectivamente la interferencia intersímbolo (ISI) causada por la dispersión temporal del canal inalámbrico. Para evitar ISI, la longitud del CP debe ser mayor que la diferencia entre los tiempos de retraso máximo y mínimo de la respuesta impulsiva del canal. Debido a la larga duración del símbolo OFDM, el ancho de banda de la subportadora es menor que el ancho de banda de coherencia del canal, lo que da como resultado un desvanecimiento en frecuencia plana para cada subportadora, permitiendo el uso de un ecualizador de un solo tap en el lado del receptor. El uso de la transformada rápida de Fourier mejora significativamente la eficiencia de implementación.

No obstante, OFDM tiene algunas desventajas. La adición del CP al símbolo OFDM es una transmisión redundante, ya que es una copia de las muestras finales colocadas al inicio. Por lo tanto, el CP aumenta la duración total del símbolo OFDM, lo que reduce la eficiencia de OFDM. La ineficiencia inducida por el CP depende de la sobrecarga del CP y la duración del símbolo. La relación pico-potencia-promedio (PAPR) es la relación entre la potencia instantánea máxima y la potencia transmitida promedio de la señal. OFDM es la suma de muchas subportadoras individuales, y en cualquier instante, la potencia de salida puede provocar un pico alto. Un PAPR alto daría lugar a la intermodulación entre subportadoras y la radiación fuera de banda (también conocida como regeneración espectral). Para evitar la regeneración espectral, el amplificador de potencia de radiofrecuencia se opera en una región lineal para evitar la saturación del amplificador (es decir, con una gran reducción de la entrada), lo que resulta en una ineficiencia de potencia que reduce la vida útil de la batería de los dispositivos.

OFDM es susceptible a desfases de tiempo y frecuencia, por lo que se requiere una estricta sincronización. La ortogonalidad en OFDM se pierde cuando hay un desfase de frecuencia del portador (CFO) debido a una discrepancia del oscilador local entre el transmisor y el receptor, lo que resulta en Interferencia entre Portadores (ICI). El CFO se puede estimar y compensar con precisión utilizando varios métodos mediante la inserción de pilotos, preámbulos o secuencias de entrenamiento en el transmisor para ayudar a la sincronización en el lado del receptor. El desfase de tiempo ocurre cuando el receptor pierde el punto de inicio del símbolo OFDM, lo que resulta en interferencia entre símbolos (ISI) que degrada el rendimiento. OFDM utiliza pulsos tipo sinc para cada forma de onda de subportadora en el dominio de frecuencia. Estos pulsos tipo sinc tienen lóbulos laterales grandes que decaen lentamente. La gran fuga de lóbulo lateral causa una alta radiación fuera de banda (OBR), lo que resulta en niveles significativos de interferencia de canal adyacente.

OFDM tiene que superar estos problemas inherentes. Por un lado, se requiere minimizar la fuga espectral y el PAPR. Por otro lado, las tasas de datos y la eficiencia deben mejorarse para soportar el conjunto diverso de escenarios en 5G. La capacidad de OFDM se puede mejorar significativamente mediante el uso de múltiples antenas de transmisión y recepción para formar un canal de entrada múltiple-salida múltiple (MIMO). El problema de PAPR y errores de sincronización son temas bien estudiados en la literatura, y se han propuesto muchas técnicas de reducción.

5G services potencialmente utilizarán bandas de frecuencia desde menos de 1 GHz hasta 100 GHz. Diferentes servicios requerirán diferentes anchos de banda. Los servicios de baja velocidad, como la conectividad masiva de máquinas, operarán en el extremo inferior del espectro. Por otro lado, las aplicaciones de alta velocidad de banda ancha (como videos HD y servicios en la nube) necesitarán anchos de banda muy altos y utilizarán el extremo superior del espectro de frecuencia. En OFDM, el ruido de fase aumenta con la frecuencia del oscilador local. Este ruido de fase conduce al error de fase común (CPE) y a la interferencia entre portadoras (ICI). El CPE se puede mitigar a través de subportadoras piloto, y la ICI depende del espaciado de subportadoras. Tenga en cuenta que el espaciado de subportadoras (SCS) es el inverso de la duración útil del símbolo OFDM, por lo que si el SCS se incrementa, la duración útil del símbolo se reduce; como la longitud del CP debe permanecer igual (está dictada por el retraso máximo de canal), la ineficiencia relacionada con CP empeora. Por lo tanto, una sola numerología OFDM no puede satisfacer los requisitos en todos estos rangos de frecuencia y admitir estas diversas aplicaciones. Para abordar este problema, 3GPP ha acordado utilizar un conjunto de numerologías OFDM para manejar una amplia gama de frecuencias y opciones de implementación.

Otra desventaja de OFDM son los grandes lóbulos laterales del espectro que causan una alta radiación fuera de banda, lo que resulta en interferencia en canales adyacentes. Como el espectro de radio es un recurso limitado, la confinación espectral es esencial para utilizar eficientemente el espectro disponible. En la radio cognitiva (CR), los usuarios secundarios (SUs) (que son usuarios no licenciados) pueden utilizar los huecos de espectro no utilizados (también conocidos como espacio en blanco) de los usuarios primarios (PUs) en cualquier momento, siempre y cuando no causen interferencia perjudicial a los usuarios primarios y la fuga de espectro de los SUs debe ser inferior a cierto umbral. Por lo tanto, es necesario reducir drásticamente los lóbulos laterales de OFDM para operar en los espacios en blanco sin causar interferencias al usuario primario.

La supresión de los lóbulos laterales también es necesaria para la coexistencia de múltiples usuarios, servicios y escenarios en 5G. Dado que 5G ofrecerá diversos servicios y escenarios en un solo bloque de espectro, es crucial reducir la fuga espectral a los canales adyacentes para utilizar eficientemente el espectro.

Para aliviar el problema de la radiación fuera de banda (OBR) de OFDM, se han propuesto numerosas técnicas para reducir la OBR en la literatura, cada una con sus ventajas y desventajas. El rendimiento de una técnica de reducción de OBR no solo se mide por su capacidad para suprimir la emisión fuera de banda, sino también por indicadores clave de rendimiento (KPI) como la complejidad computacional, la eficiencia espectral, la distorsión dentro de banda y el exceso de espectro. Equilibrar los indicadores clave de rendimiento (KPI) es crucial al reducir la OBR, ya que generalmente implica un compromiso entre uno o más parámetros de rendimiento. Sin embargo, los compromisos no son uniformes en diferentes técnicas de reducción de OBR. Por lo tanto, es esencial encontrar un equilibrio entre los KPI para satisfacer los requisitos variables de diferentes escenarios de uso.

Las técnicas de reducción de OBR se pueden clasificar ampliamente como técnicas de dominio de frecuencia y técnicas de dominio de tiempo.

Las técnicas de dominio de frecuencia operan en la entrada de la transformada inversa de Fourier rápida (IFFT) y modifican las muestras antes de la operación de IFFT. La inserción de banda de protección es uno de los métodos más simples para reducir la OBR simplemente desactivando subportadoras en los extremos de la banda espectral. Sin embargo, esto degrada significativamente la eficiencia.

La cancelación activa de interferencias (AIC) es otro método que modula algunas subportadoras reservadas con combinaciones adecuadas de los

símbolos transmitidos en las subportadoras de datos. Las técnicas de AIC son transparentes para el receptor; por lo tanto, el receptor simplemente descarta las portadoras de cancelación y las subportadoras de datos se demodulan. Por otro lado, las técnicas de AIC tienen un rendimiento limitado en términos de reducción de la relación de banda ocupada (OBR) y pueden sufrir picos espectrales.

La precodificación espectral es otra técnica popular para suprimir los lóbulos laterales en OFDM. La precodificación espectral se puede considerar como una generalización de los métodos de AIC en los que todas las subportadoras disponibles (y no solo las reservadas) se modulan con alguna función de los símbolos de datos. En general, la precodificación espectral es más efectiva que la AIC para suprimir la emisión fuera de banda; sin embargo, la operación de precodificación no es transparente para el receptor ya que introduce cierta distorsión en banda, por lo que puede ser necesario realizar una decodificación apropiada en el extremo del receptor para evitar la degradación de la tasa de error de símbolo (SER).

Basado en la estructura de los precodificadores, se pueden clasificar como lineales o no lineales. Un precodificador no lineal modula las subportadoras con alguna función no lineal de los datos para reducir la OBR. Por otro lado, con la precodificación lineal, las muestras moduladas en las subportadoras disponibles son funciones lineales de los símbolos de datos. En esta tesis, nos centraremos en esquemas de precodificación lineal. En términos generales, los precodificadores lineales se pueden clasificar en *ortogonales* o *no ortogonales* según la estructura de la matriz de precodificación. En la precodificación ortogonal, la matriz de precodificación tiene columnas ortogonales, lo que ayuda a evitar el aumento de ruido. Sin embargo, los precodificadores ortogonales generalmente son más complejos. Por otro lado, todas las técnicas de dominio de frecuencia que no tienen una estructura ortogonal en la matriz de precodificación se pueden denominar precodificadores no ortogonales. En general, las técnicas de precodificación no ortogonales pueden sufrir alguna distorsión en banda que puede degradar la tasa de error de símbolo (SER) del sistema.

Las estructuras de precodificación espectrales mencionadas anteriormente pueden tener diferentes criterios de diseño para suprimir las lóbulos laterales del OFDM; por lo tanto, las técnicas también pueden clasificarse según el criterio de diseño. Los precodificadores basados en notches colocan nulos espectrales en algunas frecuencias seleccionadas fuera de banda para reducir los lóbulos laterales. La selección de las frecuencias de los notches se realiza manualmente, y puede no ser sencillo elegirlas ya que no se garantiza la supresión espectral de otras frecuencias. Sin embargo, los precodificadores basados en notches logran una mejor eficiencia espectral, pero sufren

de distorsión en banda, y la cantidad de distorsión aumenta con el número de frecuencias de notch. En general, los precodificadores basados en notch logran la reducción de OBR a costa de la degradación y/o complejidad de la SER.

Otro criterio de diseño de precodificadores espectrales es la continuidad-N, que se basa en la observación de que la lenta disminución de los lóbulos laterales del PSD multiportadora se debe principalmente a las discontinuidades de la señal en el dominio temporal en los límites entre bloques consecutivos. Por lo tanto, de manera intuitiva, imponer la continuidad de la señal y sus primeras N derivadas en estos instantes de tiempo debería resultar en lóbulos laterales que decaen más rápidamente. Estas técnicas logran una considerable reducción de OBR a costa de alta complejidad, degradación de SER y/o señales espurias espectrales.

En lugar de colocar nulos en frecuencias predefinidas o imponer continuidad, el criterio de diseño de *supresión total* (TSC) tiene como objetivo minimizar la potencia total transmitida fuera de banda en OFDM. Los precodificadores basados en TSC minimizan la fuga de radiación fuera de banda en la región de frecuencia fuera de banda. Además, ofrece flexibilidad adicional porque permite ajustar finamente el precodificador a diferentes situaciones (por ejemplo, en sistemas CR puede ser necesario evacuar diferentes partes de la banda).

Esquemas de dominio temporal modifican directamente las muestras en la salida de la operación IFFT. Tradicionalmente, se utiliza filtrado para suprimir la emisión fuera de banda, pero normalmente requiere filtros con largas respuestas de impulso, lo que reduce significativamente el intervalo de guarda efectivo de los símbolos OFDM. En lugar de usar un filtro fijo, la transición adaptativa de símbolos (AST) optimiza de manera adaptativa la transición de la señal en función de los datos transmitidos. AST sufre de una optimización computacionalmente pesada ya que necesita resolver un problema de optimización para cada símbolo OFDM. Además, el aumento en la duración del símbolo reduce la eficiencia. Para mejorar la eficiencia y el rendimiento de datos, se propuso un enfoque de ajuste de fase. Sin embargo, tiene un rendimiento limitado en OBR y, similar a AST, el enfoque de ajuste de fase también sufre de una alta complejidad en línea. Otro enfoque efectivo en el dominio temporal para minimizar la emisión no deseada es la técnica de ventana, también conocida como superposición aditiva ponderada (WOLA) o OFDM con ventana (W-OFDM). El objetivo de estas técnicas es reemplazar el pulso rectangular estándar típico en CP-OFDM por una ventana con bordes suaves, reduciendo gradualmente la amplitud de los dos bordes de un símbolo OFDM y haciendo una transición suave entre dos símbolos OFDM, lo que resulta en una reducción de la envolvente

lateral mucho más aguda en el dominio de frecuencia. Las técnicas de ventana mencionadas anteriormente obtienen la reducción de OBR a costa de la eficiencia debido a un aumento en la duración del símbolo. Para mejorar la supresión de los lóbulos secundarios, es posible combinar diversas técnicas en los dominios del tiempo y de la frecuencia. Un enfoque propuesto implica combinar métodos en el dominio de la frecuencia, como secuencias de múltiples opciones (MCS), portadora de cancelación (CC) o ponderación de subportadora (SW), con ventaneo en el dominio del tiempo. La combinación de SW y ventaneo proporciona una mejora modesta en la reducción de la relación de banda exterior (OBR), mientras que la combinación de CC y ventaneo ha demostrado ofrecer los mejores resultados; sin embargo, puede reducir la eficiencia espectral debido al uso de técnicas de CC y ventaneo. Otro enfoque propuesto para suprimir los lóbulos secundarios de OFDM implica combinar el método de AIC en el dominio de la frecuencia con pulsos de conformación en el dominio del tiempo.

En resumen, a lo largo de los años se han propuesto una multitud de técnicas en los dominios del tiempo y de la frecuencia para suprimir los grandes lóbulos secundarios de OFDM, que llevan a radiación fuera de banda. Todas estas técnicas tienen sus propias ventajas e inconvenientes. La reducción de la OBR se logra a costa de uno o más de los parámetros de rendimiento: complejidad computacional, eficiencia espectral, picos espectrales y/o tasa de error de símbolo. Por ejemplo, la reducción de la OBR lograda por técnicas como la inserción de banda de guarda, las secuencias de múltiples opciones y el ventaneo se logra a costa de la eficiencia. Las técnicas dependientes de los datos, como la ponderación de subportadora, la expansión de constelación, el ajuste de fase y la transición de símbolo adaptativo, tienen un alto costo en términos de complejidad y/o tasa de error de símbolo. El costo de las técnicas AIC se encuentra en términos de pico espectral y eficiencia espectral. Los pre-codificadores espectrales logran la reducción de la OBR a expensas de la eficiencia espectral, la complejidad y/o la tasa de error de símbolo.

Por lo tanto, existe un compromiso entre los indicadores clave de rendimiento (KPI) mencionados anteriormente, y los compromisos no son los mismos para cada técnica de reducción de OBR. Además, dependiendo de las aplicaciones, los escenarios de uso, las máscaras de emisión espectrales particulares y los recursos disponibles, es posible que se desee sacrificar el rendimiento de OBR a cambio de una mejora en otro indicador clave o viceversa. Por lo tanto, el equilibrio entre los KPI es de vital importancia para satisfacer los diversos requisitos de diferentes escenarios de uso. Además, muchos métodos de supresión de lóbulo lateral carecen de flexibilidad porque no permiten a los usuarios elegir el rango de frecuencias de interés sobre el cual se debe enfatizar la reducción de OBR.

Motivado por las consideraciones anteriores, en esta tesis proponemos una serie de diseños novedosos para suprimir la OBR en sistemas multiportadora para evitar la interferencia en canales adyacentes. Estos diseños brindan la flexibilidad de elegir el rango de frecuencias mediante una función de ponderación espectral para enfatizar algunas frecuencias sobre otras. Los diseños propuestos son una generalización del criterio TSC presentado anteriormente y pueden entenderse como un criterio TSC ponderado. El objetivo es minimizar la OBR en una región de frecuencia seleccionable por el usuario. En otras palabras, los diseños de la tesis se basan en PSD en lugar de basarse en N-continuo o en muescas. Además, los diseños propuestos son lo suficientemente flexibles para permitir el compromiso mencionado anteriormente entre los KPI: OBR, complejidad, tasa de error de símbolo, picos espectrales y eficiencia espectral, para satisfacer los diversos requisitos de diferentes aplicaciones y escenarios. Además, todos los diseños propuestos son independientes de datos y se pueden calcular sin conexión.

Se propone una técnica de ventana temporal efectiva que es tanto efectiva como simple, y transparente para el receptor. El diseño óptimo de ventana propuesto tiene la flexibilidad de moldear la densidad espectral de potencia para enfocarse en OBR en los rangos de frecuencia de interés, a diferencia de los enfoques de ventana tradicionales. Además, el diseño optimiza el rendimiento de OBR en diferentes regiones de frecuencia en función de los requisitos del sistema, es decir, puede ser útil obtener una reducción de OBR más cercana a los extremos del espectro a expensas de OBR en frecuencias más alejadas.

El pre-codificado espectral es un enfoque popular en el dominio de frecuencia para abordar la OBR. En general, el pre-codificado espectral proporciona una alta reducción de OBR a expensas de una alta complejidad. Sin embargo, ciertas aplicaciones se preocupan más por la complejidad, especialmente los dispositivos alimentados por batería o de bajo consumo. Por lo tanto, puede ser beneficioso sacrificar OBR a cambio de una menor complejidad, siempre y cuando la OBR satisfaga la máscara de emisión espectral. Presentamos un nuevo enfoque de pre-codificación que controla cuidadosamente la cantidad de distorsión en las subportadoras de datos mediante un parámetro seleccionable por el usuario, que a su vez determina la complejidad del receptor. Además, el diseño propuesto del pre-codificador espectral minimiza la OBR en un rango de frecuencia determinado.

También se presenta un diseño conjunto de precodificación espectral y ventana que aprovecha las ventajas de ambos enfoques. Al optimizar los coeficientes del precodificador y la ventana para reducir la potencia radiada dentro de un rango de frecuencia especificado, el diseño logra un equilibrio superior entre la radiación fuera de banda (OBR), el rendimiento y la com-

plejidad en comparación con el uso de estas técnicas individualmente. Los resultados demuestran la efectividad de este enfoque.

La tesis presenta un enfoque de precodificación basado en memoria para mitigar el problema de los lóbulos laterales grandes. Al incorporar memoria en el precodificador, se puede mejorar el rendimiento de radiación fuera de banda (OBR) sin comprometer la eficiencia espectral, aunque a expensas de una mayor complejidad computacional. El nuevo precodificador basado en memoria está diseñado para minimizar la OBR total dentro de un rango de frecuencia definido por el usuario. Además, esta técnica permite el control sobre los picos espectrales, lo que permite niveles flexibles de OBR.

Contents

Abstract I

Resumen II

1. Introduction **1**

1.1. Fifth Generation (5G) mobile networks 1

1.1.1. Waveform contenders for 5G 4

1.2. OFDM 6

1.3. OBR reduction techniques 10

1.3.1. Frequency domain techniques 12

1.3.2. Time domain techniques 15

1.4. Contributions 18

1.5. Signal Model for OFDM 19

1.6. Publications 22

1.7. Thesis Structure 23

2. Window Design for OFDM **25**

2.1. Introduction 25

2.2. Signal Model 26
2.3. Optimal window design 28
2.4. Results and Discussion 29
2.5. Conclusion 36

3. Distortion-constrained memoryless spectral precoding 37
3.1. Introduction 37
3.2. Signal model 38
3.3. Total Distortion Constraint (TDC) 39
3.3.1. Complexity analysis 41
3.3.2. Numerical examples and Discussion 42
3.4. Per-subcarrier distortion constraint (PSDC) 51
3.4.1. Complexity analysis 54
3.4.2. Numerical examples 54
3.5. Conclusion 62

4. Joint Window and Precoder Design 63
4.1. Introduction 63
4.2. System Model 64
4.3. Joint Design 65
4.3.1. Optimal window for a given precoder 65
4.3.2. Optimal precoder for a given window 65
4.3.3. Cyclic optimization 67
4.4. Receiver, Efficiency, and Complexity 67
4.5. Results 68

4.5.1. Windowing and Orthogonal Precoding 69
4.5.2. Windowing and AIC precoding 71
4.6. Conclusion 75

5. Memory-based spectral precoding **77**
5.1. Introduction 77
5.2. Signal Model 79
5.3. Proposed Memory AIC Precoder 81
5.3.1. Results and Discussion 82
5.4. Proposed Orthogonal Memory Precoder 88
5.4.1. Decoder 89
5.4.2. Complexity Analysis 90
5.4.3. Numerical examples 90
5.5. Conclusion 98

6. Conclusions and Future Work **99**

A. Solution to optimal window design (2.8) **103**

B. Solution to problem (3.7) **using GSVD** **105**

C. Solution to problem (3.8) **109**

D. Low-rank approximation **111**

E. Solution to problem (3.13) **113**

Bibliography **115**

List of Figures

1.1. Estimation of global traffic by ITU [1] 2

1.2. Estimation of number of connected devices by ITU [1] 2

1.3. 5G network services and scenarios 3

1.4. OFDM block diagram 7

2.1. Time domain windowing at the transmitter. 27

2.2. PSD of OW-OFDM, RC W-OFDM and CP-OFDM for $H = 1/4$ CP and different spectral weighting functions. 29

2.3. PSD of OW-OFDM (dashed), RCW-OFDM (solid) and CP-OFDM (thin solid) for different window overhead values (expressed as a fraction of the CP length). 30

2.4. PSD of OW-OFDM (dashed), RCW-OFDM (solid) and CP-OFDM (thin solid) for different window overhead values (expressed as a fraction of the CP length). 30

2.5. PAPR of the proposed OW-OFDM (dahed) for different window overhead values (expressed as a fraction of the CP length). 31

2.6. PSD of OW-OFDM, RC W-OFDM and CP-OFDM for $H = 1/4$ CP in cognitive radio Scenario 1. 32

2.7. PSD of OW-OFDM, RC W-OFDM and CP-OFDM for $H = 1/4$ CP in cognitive radio Scenario 2. 32

2.8. PSD of OW-OFDM, RC W-OFDM and CP-OFDM for $H = 1/4$ CP in cognitive radio Scenario 3. 32

2.9. Signal-to-Interference Ratio for two asynchronous users with $\Delta f = 15$ kHz. $H = 1/4$ CP. 34

2.10. Signal-to-Interference Ratio for two adjacent numerologies: $\Delta f_1 = 15$ kHz, $\Delta f_2 = 30$ kHz. $H = 1/4$ CP. 34

2.11. Signal-to-Interference Ratio for two adjacent numerologies: $\Delta f_1 = 15$ kHz, $\Delta f_2 = 60$ kHz. $H = 1/4$ CP. 35

3.1. PSD for different values of ϵ. $N = 257$, $K_c = 50$, $\beta = 1$. . . . 43

3.2. SER in AWGN channel of the proposed iterative decoder for different values of ϵ. $K = 257$, $K_c = 50$, $\beta = 1$. 43

3.3. Convergence of the proposed TDC design in terms of OBR in the setting of Fig. 3.1 43

3.4. PAPR of the proposed TDC design in the setting of Fig. 3.1 with 16 16-QAM modulation. 44

3.5. PSD for different values of β. $K = 257$, $K_c = 50$, $\epsilon = 0.002$. . 45

3.6. OBR achieved with TDC design (relative to that of the unprecoded system) as a function of spectral overshoot. $K = 257$, $K_c = 50$. 45

3.7. Singular values of matrices $\boldsymbol{P}$ and $\boldsymbol{Q}$. $K = 257$, $K_c = 50$, $\epsilon = 0.02$, $\beta = 1$. 45

3.8. PSD of different designs with different ϵ and K_c. $K = 257$. . 46

3.9. SER in AWGN channel for TDC design. $K = 257$, $K_c = 8$, $\epsilon = 0.0165$. 47

3.10. SER in AWGN channel for TDC design. $K = 257$, $K_c = 6$, $\epsilon = 0.018$. 47

3.11. SER in AWGN channel for TDC design. $K = 257$, $K_c = 4$, $\epsilon = 0.022$. 47

3.12. PSD of various designs in cognitive radio Scenario 1, $K = 226$. 48

3.13. PSD of various designs in cognitive radio Scenario 2, $K = 242$. 48

3.14. PSD of various designs in cognitive radio Scenario 3, $K = 211$. 49

3.15. SER in multipath channel of the proposed iterative decoder for different values of ϵ. $K = 257$, $K_c = 50$. 50

3.16. PSD of the proposed TDC design with an LPF for different values of ϵ. $K = 257$, $K_c = 50$. 50

3.17. Frequency response of the 10th order Chebyshev type II filter with a cutoff frequency of $f_c = 10$ MHz and -80 dB stop band ripples. 51

3.18. Impulse response of the Chebyshev type II filter. 51

3.19. Normalized MSE for the TDC design. $\epsilon_{\text{TDC}} = 0.02$. 52

3.20. Obtained PSDs for a system with $K = 257$, $K_c = 20$. "Standard OFDM" refers to a system with $(\boldsymbol{P}, \boldsymbol{Q}) = (\boldsymbol{I}_{K_d}, \boldsymbol{0})$. . . . 55

3.21. SER in AWGN channel, $K = 257$, $K_c = 20$. TDC design (left), PSDC design (right). 55

3.22. Obtained PSDs for a system with different values of β. $K = 257$, $K_c = 20$. $\epsilon_i = 0.0005$. 55

3.23. Obtained PSDs for a system with different values of ϵ. $K = 257$, $K_c = 20$, $\beta = 1$. 56

3.24. SER in AWGN channel of the proposed iterative decoder with PSDC design. $K = 257$, $K_c = 20$, $\beta = 1$. 56

3.25. Convergence of the proposed PSDC method in terms of OBR in the settings of Fig. 3.23. 57

3.26. PAPR of the PSDC design for the settings in Fig. 3.23 with 16-QAM modulation. 57

3.27. Obtained PSDs in cognitive radio Scenario 1. 58

3.28. Obtained PSDs in cognitive radio Scenario 2. 58

3.29. Obtained PSDs in cognitive radio Scenario 3. 58

3.30. Obtained PSDs for a system with $K = 257$, $K_c = 4$. 60

3.31. Distortion profile $\{\epsilon_i\}$ of the proposed PSDC design. 60

3.32. SER in AWGN channel of the proposed iterative decoder with PSDC design. (a) $\epsilon_i = 0.007\ \forall i$, (b) ϵ_i as in Fig. 3.31. 61

3.33. SER in multipath channel of the proposed iterative decoder with PSDC design. $K = 257$, $K_c = 20$, $\beta = 1$. 61

3.34. PSD of the PSDC design at the output of LPF . $K = 257$, $K_c = 20$. 62

4.1. PSD of the proposed JPW-OP design for different (K_c, H) pairs. $\eta = 84.6\%$, $N = 256$, $N_{\text{CP}} = N/4$, $K = 65$. 69

4.2. PAPR of the proposed JPW-OP design for the Fig. 4.1 with 16 QAM modulation. 70

4.3. PSD of the proposed JPW-OP design in cognitive scenario. $\eta = 78.4\%$, $N = 256$, $N_{\text{CP}} = N/4$, $K = 65$. 70

4.4. PSD of JPW-AIC for different (K_c, H) pairs. $\eta = 84.6\%$. Spectral peak is limited to 2 dB. $N = 256$, $N_{\text{CP}} = N/4$, $K = 65$. 71

4.5. Convergence of the proposed designs in terms of OBR in the setting of Figs. 4.1 and 4.4. 72

4.6. PAPR of JPW-AIC for the settings in Fig. 4.4 with 16-QAM modulation. 72

4.7. PSD of JPW-AIC for different (K_c, H) pairs. $\eta = 83.1\%$. Spectral peak is limited to 2 dB. $N = 256$, $N_{\text{CP}} = N/4$, $K = 107$. 74

5.1. OBR achieved with AIC precoders (relative to that of the unprecoded system) as a function of spectral overshoot. $K_d =$ 53 data subcarriers. 82

5.2. Transmit power of AIC precoders (relative to that of the unprecoded system) as a function of spectral overshoot. $K_d =$ 53 data subcarriers. 83

5.3. PSDs for 1-dB spectral overshoot. $K_d = 53$ data subcarriers. Dashed vertical lines mark the OBR region $\mathbb{B}$. 84

5.4. PAPR of the different designs in Fig. 5.3 with 16-QAM modulation. 84

5.5. PSDs in cognitive radio Scenario 1. Spectral overshoot is limited to 1-dB. 85

5.6. PSDs in cognitive radio Scenario 2. Spectral overshoot is limited to 1-dB. 85

5.7. PSDs in cognitive radio Scenario 3. Spectral overshoot is limited to 1-dB. 86

5.8. OBR (relative to that of the unprecoded system) with memory AIC precoders of different orders, and for different number of data subcarriers K_d. Spectral overshoot is kept at 1 dB in all cases. 87

5.9. PSDs of different precoder designs. $N = 256$, $N_{cp} = N/4$, $K = 129$, $K_d = 121$. 91

5.10. OBR (relative to that of the unprecoded system) as a function of spectral peak. $N = 256$, $N_{cp} = N/4$, $K = 129$, $K_d = 121$. 91

5.11. PAPR of the proposed design with 16-QAM modulation. . . 91

5.12. PSDs of different precoder designs in cognitive radio Scenario 1. $N = 256$, $N_{cp} = N/4$, $K = 114$, $K_c = 12$. 93

5.13. PSDs of different precoder designs in cognitive radio Scenario 2. $N = 256$, $N_{cp} = N/4$, $K = 122$, $K_c = 12$. 93

5.14. PSDs of different precoder designs in cognitive radio Scenario 3. $N = 256$, $N_{cp} = N/4$, $K = 107$, $K_c = 12$. 93

5.15. PSDs of different designs. $N = 256$, $N_{cp} = N/4$, $K = 129$, $K_d = 121$. Spectral peak is 3.2 dB for N-continuous and proposed precoders. 94

5.16. SER of 1st-order memory precoder for 16-QAM in AWGN channel. $N = 256$, $N_{cp} = N/4$, $K = 129$, $K_d = 121$. 94

5.17. SER of 1st-order memory precoder for 16-QAM in multipath channel. $N = 256$, $N_{cp} = N/4$, $K = 129$, $K_d = 121$. 95

5.18. OBR (relative to that of the unprecoded system) of the proposed design, for different values of order ℓ_0 and redundancy K_c. Spectral peak is set to 1 dB in all cases. 96

5.19. Singular values of precoding matrices $\{\boldsymbol{G}_\ell,\ 1 \leq \ell \leq \ell_0\}$. $N = 256$, $N_{cp} = N/4$, $K = 129$, $K_c = 8$. Spectral peak is set to 1 dB in all cases. 97

List of Tables

1.1. Different numerologies proposed for 5G NR [2]. 10

3.1. Computational complexity of different designs (no. of complex multiplications per OFDM symbol) for the same spectral efficiency for different scenarios. 59

4.1. Online Complexity and OBR (relative to that of plain CP-OFDM with 10 null subcarriers) of JPW-OP and RC-OP. $\eta = 84.6\%$. 69

4.2. Online Complexity and OBR (relative to that of plain CP-OFDM with 10 null subcarriers) of JPW-AIC and RC-AIC. $\eta = 84.6\%$, Spectral peak ≤ 2 dB. 71

4.3. Online Complexity and OBR (relative to plain OFDM with null subcarriers) of different designs. $N = 256$, $K = 65$. . . . 73

5.1. Relative OBR (in dB) of memory precoders for different orders, redundancies, and CP lengths. $N = 256$, $K = 129$. Spectral peak is set to 1 dB in all cases. 97

List of Abbreviations

1G	First Generation
3GPP	Third Generation Partnership Project
4G	Fourth Generation
5G	Fifth generation
5G-NR	5G new radio
AR	Augmented Reality
AIC	Active Interference Cancellation
AST	Adaptive Symbol Transition
AWGN	Additive White Gaussian Noise
BRAN	Broadcast Radio Access Network
BT-LE	Bluetooth Low Energy
CR	Cognitive Radio
CFO	Carrier Frequency Offset
CPE	Common Phase Error
CP	Cyclic Prefix
CP-OFDM	Cyclic Prefix Orthogonal Frequency Division Multiplexing
CE	Constellation Expansion
DFT	Discrete Fourier transform
DFT-s-OFDM	DFT-spread OFDM
DAB	Digital Audio Broadcasting
DVB	Digital Video Broadcasting
ETSI	European Telecommunications Standards Institute
eMBB	enhanced Mobile Broadband
FM	Frequency Modulation
FBMC	Filter Bank Multicarrier
FFT	Fast Fourier Transform
F-OFDM	Filtered-OFDM
FC-OFDM	Flexibly Configured OFDM
FS-FBMC	Frequency Spreading FBMC
FIR	Finite Impulse Response
GFDM	Generalized Frequency Division Multiplexing
GSVD	Generalized Singular Value Decomposition
HIPERLAN	High Performance Local Area Networks

HD	High Definition
HF	High Frequency
IEEE	Institute of Electrical and Electronics Engineers
IFFT	Inverse Fast Fourier Transform
ISI	Intersymbol Interference
ICI	Intercarrier Interference
INI	Inter-Numerology Interference
ITU	International Telecommunication Union
IIR	Infinite Impulse Response
KPI	Key Performance Indicator
LTE	Long-Term Evolution
LS	Least Squares
LPF	Low Pass Filter
MC	multicarrier
mMTC	massive Machine Type Communications
MIMO	Multiple-input and Multiple-output
MCQ	Multiple Choice Sequences
NMSE	Normalized Mean Squared Error
OBR	Out-of-Band Radiation
OQAM-FBMC	Offset quadrature amplitude modulation
PSD	Power Spectral Density
PU	Primary User
P-OFDM	Pulse-shaped OFDM
PRB	Physical Resource Block
PAPR	Peak-to-Average Power Ratio
PSDC	Per-Subcarrier Distortion Constrained
RF	Radio Frequency
RC	Raised Cosine
SIR	Signal-to-Interference Ratio
SER	Symbol Error Rate
SU	Secondary User
SCS	Subcarrier Spacing
SC-FDE	Single Carrier Frequency Domain Equalization
SMT	Staggered Multi-Tone
SW	Subcarrier Weighting
TSC	Total Suppression Criterion
TDC	Total Distortion Constrained
UFMC	Universal Filtered Multicarrier
UW-OFDM	Unique Word OFDM
URLLC	Ultra-Reliable Low-Latency Communications
VR	Virtual Reality
WLAN	Wireless Local Area Network
WOLA	weighted overlap-add
W-OFDM	windowed OFDM

Chapter 1

Introduction

Mobile communication has seen phenomenal growth over the past few decades, from the First Generation (1G) of mobile communication systems focused on voice to the Fourth Generation (4G) systems shifted to data and mobile broadband services. The exceptional growth in the volume of mobile data will reach up to 160 exabytes per month by 2025, according to Ericsson's report [3]. Another study by International Telecommunication Union (ITU) forecasts the global traffic to cross over five zettabytes per month by 2030, as shown in Fig. 1.1. Moreover, the exponential growth of the number of connected devices could reach up to 114 billion by 2030, as shown in Fig. 1.2.

Evolution towards the next generation is much required to support this massive and exponential increase in data usage and the connectivity of a large number of devices. Consequently, Fifth Generation (5G) mobile networks have been proposed to meet the traffic growth and provide enhanced quality of service to massive end-users by building cost-efficient networks.

1.1. Fifth Generation (5G) mobile networks

The Fifth generation (5G) mobile network was envisioned to be a revolutionary leap forward and provide significant improvements across all key performance indicators, i.e., data rate, massive connectivity, latency, network reliability, and energy efficiency. This highly heterogeneous 5G mobile network system would support diverse services over a single platform. The International Telecommunication Union (ITU) has classified the services offered by the 5G network mainly into three categories: enhanced Mobile

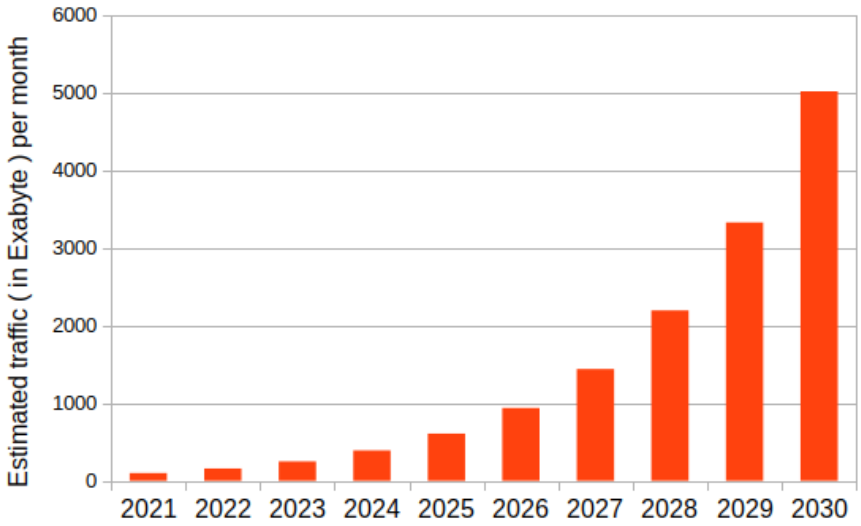

Figure 1.1: Estimation of global traffic by ITU [1]

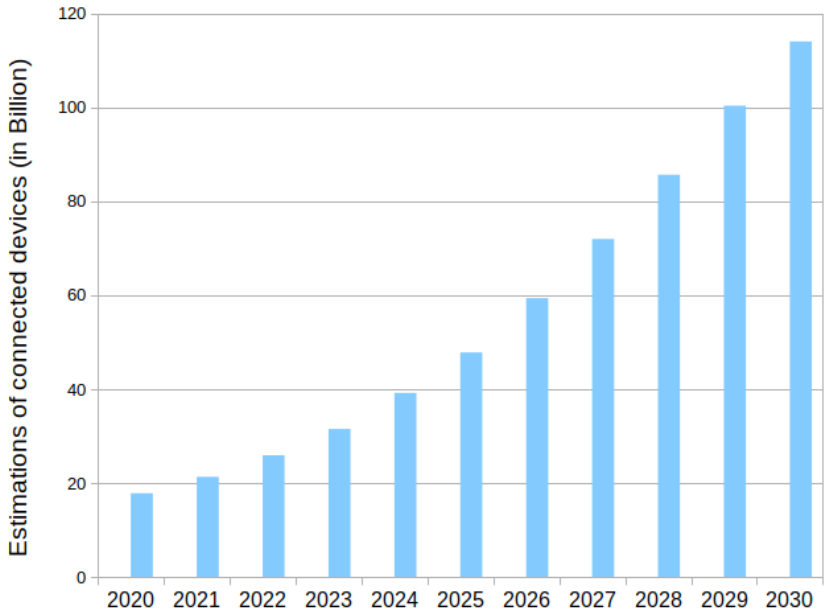

Figure 1.2: Estimation of number of connected devices by ITU [1]

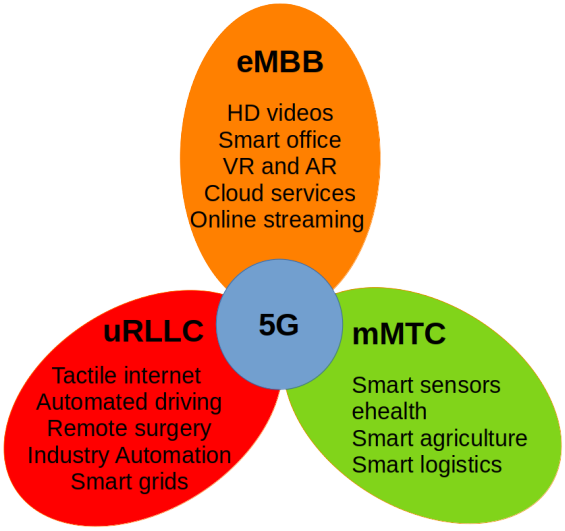

Figure 1.3: 5G network services and scenarios

Broadband (eMBB), massive Machine Type Communications (mMTC), and Ultra-Reliable Low-Latency Communications (URLLC), as shown in Fig. 1.3 [4].

Enhanced mobile broadband (eMBB) aims to address data-driven and human-centric services, offering improved performance in terms of high data rates along with a seamless user experience. The goal of eMBB is to meet the high bandwidth demands of services such as virtual reality (VR), augmented reality (AR), cloud-based applications and services, high-definition (HD) videos, and wireless internet access. Ultra-reliable and low latency communications (URLLC) put stringent latency, reliability, and availability requirements for mission-critical and real-time control applications. Some examples are tactile internet applications, automated driving, remote medical surgery, transportation safety, industrial robotics, public protection, smart grids, disaster relief, and vehicle-to-vehicle communications. Massive machine-type communications (mMTC) will cater to a very large number of low-cost devices with very long battery life. Smart cities, healthcare, manufacturing, smart agriculture, consumer goods, business communications, and transportation are a few examples of mMTC applications [5–8].

The future network will provide services to a highly diverse set of scenarios, and to efficiently support such diverse use cases, the 5G air interface needs to be flexible enough to meet the requirements of existing and future services. Transceiver complexity is vital for low-cost battery-powered devices and for supporting low-latency applications. High spectral efficiency and Multiple-input and Multiple-output (MIMO) compatibility are essential

to meet the extreme requirements of data rate, a large number of connections, and high traffic densities. Moreover, spectral containment to reduce out-of-band emissions is critical for the coexistence of different services.

Thus, the 5G air interface has to be highly flexible, robust, spectrally efficient, reliable, scalable, and energy-efficient to meet the stringent requirements of diverse applications. Moreover, the radio interface must have a unified framework supporting the various scenarios on a single block of spectrum [9]. Different waveforms have been studied over the years in the literature to address the abovementioned challenges.

1.1.1. Waveform contenders for 5G

Filter bank multicarrier (FBMC) was one of the strong candidate waveforms for 5G [10, 11]. The FBMC applies the pulse shaping filter on each subcarrier individually to achieve better sidelobe decay. Due to its high spectral efficiency, excellent spectral containment, and much weaker sidelobes causing small intercarrier interference, it gained high attraction, especially in the case of transmitting long sequences. However, during short bursts, the time-frequency efficiency is significantly degraded. The loss may be reduced at the expense of increased intercarrier interference, and out-of-band radiation [12]. FBMC also suffers from high computational complexity, and its MIMO implementation may be very limited [13]. Offset quadrature amplitude modulation (OQAM-FBMC) or staggered multi-tone (SMT) was proposed to make the subcarriers orthogonal in the real domain and to increase the spectral efficiency [13]. However, transmission via complex channels can cause intrinsic interference, and it is difficult to use the conventional pilot design, channel estimation techniques, and MIMO technologies. To avoid this problem, QAM-FBMC was proposed [14, 15].

Universal Filtered Multicarrier (UFMC) was also proposed for the 5G air interface [16, 17]. It filters per subband (for example, per physical resource block (PRB)) to suppress unwanted emissions. Another advantage of filtering per subband is that the filter length may be significantly shorter. Hence, the UFMC waveform achieves high spectral efficiency in short bursts, making it an appealing technique for low-latency communications. UFMC is fully compatible with MIMO. On the other hand, UFMC is more sensitive to time misalignment because there is no cyclic prefix (CP), suffers from intersymbol interference (ISI) for moderately large delay spreads, and has complexity issues due to large Fast Fourier Transform (FFT) size.

Generalized frequency division multiplexing (GFDM) is another waveform that has been studied for 5G networks [18, 19]. GFDM consists of

a block structure, where each block contains several subcarriers and subsymbols. Each subcarrier is filtered with a prototype filter, and a cyclic prefix is added per block. GFDM achieves lower out-of-band radiation and better spectral efficiency. GFDM has non-orthogonal subcarriers because of the filtering, causing inter-symbol interference (ISI) and intercarrier interference (ICI). However, interference can be reduced at the expense of increased complexity, and some loss in performance [20].

Another waveform that was considered for the 5G radio interface is Cyclic Prefix Orthogonal Frequency Division Multiplexing (CP-OFDM). Due to its inherent advantages, i.e., spectral efficiency, robustness against multipath effects, and a good match for MIMO, it was already being used in the 4-th generation systems (LTE) as the signaling waveform. However, it suffers from Peak-to-Average Power Ratio (PAPR), large sidelobes, and sensitivity to frequency offsets and phase noise.

These were some of the major contenders for the 5G air interface. However, many other waveforms were studied and suggested for the 5G network. Constant envelope waveforms are simple and low complexity waveforms used in ZigBee, Bluetooth, and Bluetooth Low Energy (BT-LE); however, they have poor spectral efficiency [21, 22]. Single Carrier Frequency Domain Equalization (SC-FDE) improves the performance in multipath fading at the cost of spectral efficiency [23]. Different versions of DFT-spread OFDM (DFT-s-OFDM), a variation of SC-FDE, were proposed as potential waveforms for 5G networks [24, 25]. DFT-s-OFDM is also used in the 4G-LTE uplink.

Zero-tail DFT-spread OFDM inserts zero-head and zero-tail samples before DFT to suppress out-of-band radiation and potentially reduce the overhead [26, 27]. Filtered-OFDM (F-OFDM) is another approach for achieving a better OBR suppression than legacy CP-OFDM by utilizing a filtering approach [28, 29]. The bandpass filter is bandwidth dependent which may lead to varying ISI. Moreover, the long filter length may lead to a large processing delay, which is a potential concern for low-latency applications. Different pulse shape designs for OFDM were proposed, sometimes also called pulse-shaped OFDM (P-OFDM) [30–32]. Unique Word (UW-OFDM) replaces the CP with a known sequence, which may improve the spectral efficiency and have very low PAPR [33]. An improved Unique Word DFT-Spread OFDM Scheme for 5G Systems was proposed in [34]. Other heuristic waveforms like Flexibly Configured OFDM (FC-OFDM) [35], Frequency Spreading FBMC (FS-FBMC) [36] were proposed for the 5G radio.

As can be seen from the previous discussion, many waveforms were proposed in the quest for finding the best waveform for the 5G radio in-

terface. Different comparisons were performed in the literature, and various waveforms were suggested for different scenarios. Universal Filtered Multi-Carrier (UFMC) was proposed by [37, 38] for short-packet communications and low-latency transmissions. On the other hand, [39] recommended UFMC for short burst communications and GFDM for achieving very short latency due to its flexibility and block structure. Moreover, according to [40], GFDM is the most suited waveform for 5G asynchronous communications. Another study recommended f-OFDM for the 5G air interface to support the diverse services and deployment scenarios [41], and it is also recommended for high-speed scenarios [42]. FBMC was also suggested as a waveform for its minor interference between adjacent bands [43].

All the above proposed waveforms for the 5G air interface have their own advantages and drawbacks, and each waveform is a preferable modulation format for a specific scenario. However, CP-OFDM was found to be the most appropriate candidate for the 5G radio interface. CP-OFDM showed better performance in all the key indicators: good compatibility with MIMO, low implementation complexity, and high spectral efficiency. It is well-localized in the time domain and more robust against phase noise and doppler effects than other multicarrier waveforms [44]. Due to these advantages, in August 2016 the Third Generation Partnership Project (3GPP) agreed on the use of CP-OFDM for the 5G new radio (5G-NR) interface [45]. In the next section, we provide a brief historical overview of OFDM.

1.2. OFDM

Orthogonal frequency division multiplexing is a special case of multicarrier (MC) modulation that dates back to the 1960s. The concept of multicarrier transmission was first proposed in 1966 to achieve high data rate communication [46, 47]. In 1967, the first application of MC in High Frequency (HF) radio was published [48]. Peled presented a simplified OFDM implementation [49]. The first application of OFDM for mobile wireless communications was proposed in 1985 [50], whereas [51] studied its performance and complexity. The introduction of Discrete Fourier transform (DFT) significantly reduced the implementation complexity [52]. Later in 1991, experimental results were presented and discussed for the application of OFDM over mobile radio FM channels [53].

With these developments, OFDM was adopted for the European digital audio broadcasting (DAB) standard and the Digital Video Broadcasting (DVB) standard for digital terrestrial television [54, 55]. Moreover, OFDM has been used by standards like IEEE 802.16, IEEE 802.20, and

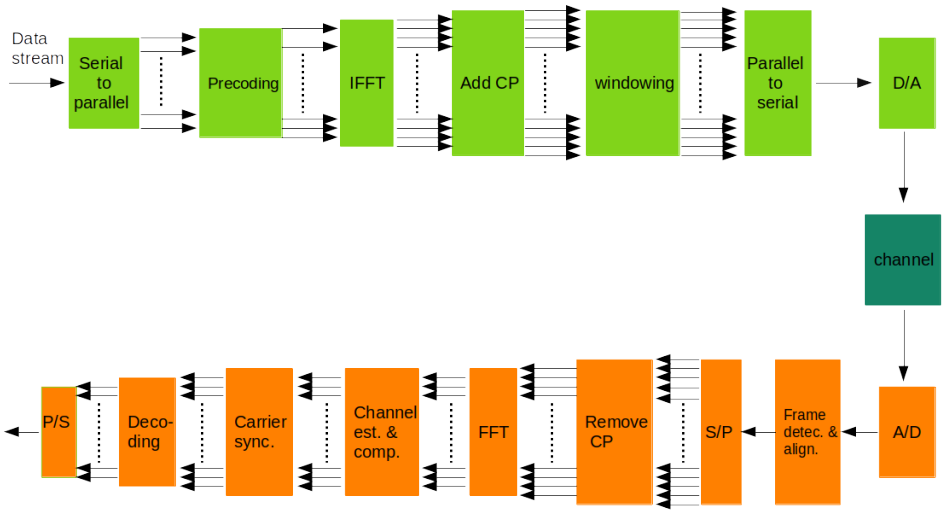

Figure 1.4: OFDM block diagram

European Telecommunications Standards Institute (ETSI) Broadcast Radio Access Network (BRAN) committees [56]. OFDM was also used in high-performance local area networks (HIPERLAN) transmission technique as well as the IEEE 802.11 Wireless Local Area Network (WLAN) standard. OFDM is also adopted as the signaling technique for 4G LTE and 5G NR. OFDM was introduced in Power Line Communications (PLC) to address the frequency selective nature of the power line channel, which can cause significant signal degradation and low data rates [57–59]. This led to its adoption in standards such as IEEE 1901.2 [60], ITU-T G.9903 [61], and ITU-T G.9960 [62]. Since its introduction, numerous developments and improvements have been made in the literature to further enhance the performance of OFDM-based PLC systems [63–68].

A general block diagram for digital data transmission based on CP-OFDM is shown in Fig. 1.4. OFDM divides the entire channel bandwidth into many narrow bands (also called sub-channels or subcarriers), which are transmitted in parallel to maintain high data rate transmission, and at the same time making it robust against frequency selective fading. High spectral efficiency is achieved by overlapping and spacing the subcarriers closer to each other. The subcarriers are orthogonal to each other in order to avoid interference between the tightly spaced carriers. The use of cyclic prefix (CP) effectively alleviates intersymbol interference (ISI) caused by the

delay spread of the wireless channel, and in order to avoid ISI, the length of CP should be larger than the difference between the maximum and the minimum delays of the channel impulse response. Due to the long symbol duration of OFDM, the subcarrier bandwidth is smaller than the channel coherence bandwidth which yields frequency flat fading for each subcarrier, allowing the use of a one-tap equalizer approach at the receiver side. The use of fast Fourier transform significantly improves implementation efficiency.

Nonetheless, OFDM suffers from some drawbacks, which are briefly discussed below.

- CP-induced inefficiency: The addition of the CP to the OFDM symbol is a redundant transmission, since it is a copy of the tail samples placed at its beginning. Thus, the CP increases the overall symbol duration of OFDM, which reduces the efficiency of OFDM. The CP-induced inefficiency depends on the CP overhead and the symbol duration. For a given CP, the efficiency of OFDM is reduced by a factor of $\frac{\text{symbol duration}}{\text{CP length+symbol duration}}$.

- Peak-to-average-power-ratio: The PAPR is the ratio between the maximum instantaneous power and the average transmitted power of the signal. OFDM is the summation of the many individual subcarriers, and at any instant, the output power may lead to a high peak. High PAPR would result in intermodulation among subcarriers and out-of-band radiation (also known as spectral regrowth). In order to avoid spectral regrowth, the RF power amplifier is operated in a linear region to avoid amplifier's saturation (i.e., with a large input backoff); resulting in power inefficiency which reduces the battery life of devices.

- Sensitivity to synchronization errors: OFDM is susceptible to time and frequency offsets, so strict synchronization is required. The orthogonality in OFDM is lost when there is carrier frequency offset (CFO) because of a mismatch of the local oscillator between the transmitter and receiver, resulting in Inter-Carrier Interference (ICI). CFO can be accurately estimated and compensated using various methods by inserting pilots, preambles, or training sequences at the transmitter to assist the synchronization at the receiver side. The timing offset occurs when the receiver loses the starting point of the OFDM symbol, resulting in inter-symbol interference (ISI) which degrades the performance.

- Large spectrum sidelobes: OFDM uses sinc-like pulses for each subcarrier waveform in the frequency domain. These sinc-type pulses have large sidelobes which decay slowly. The large sidelobe leakage causes

high out-of-band radiation (OBR), resulting in significant levels of adjacent channel interference.

OFDM has to overcome these inherent problems. On one hand, it is required to minimize spectral leakage and PAPR. On the other hand, data rates and efficiency need to be improved to support the diverse set of scenarios in 5G. The capacity of OFDM can be significantly improved by using multiple transmit and receive antennas to form a multiple-input–multiple-output (MIMO) channel [69–76]. The problem of PAPR is a well-studied topic in literature, and many PAPR reduction techniques have been proposed [77–80]. The synchronization errors of OFDM can be mitigated via various methods proposed in literature [81–89].

5G services will potentially utilize frequency bands below 1 GHz up to 100 GHz. Different services will require different bandwidths. Low bandwidth services like massive machine connectivity will operate at the lower end of the spectrum. On the other hand, bandwidth-hungry applications (like HD videos and cloud services) will need very high bandwidths and use the high end of the spectrum band. In OFDM, phase noise increases with the frequency of the local oscillator [90], but note that this is a physical effect not related to the modulation used (could be OFDM or other). This phase noise leads to common phase error (CPE) and inter-carrier interference (ICI). CPE can be mitigated via pilot subcarriers, and ICI depends on the subcarrier spacing. Note that the subcarrier spacing (SCS) is the inverse of the useful OFDM symbol duration, thus if the SCS is increased, the useful symbol duration is decreased; since the CP length must stay the same (it is dictated by the maximum channel delay spread), the CP-related inefficiency becomes worse. Thus, a single OFDM numerology cannot meet the requirements across all these frequency ranges and support these diverse applications. To tackle this issue, 3GPP has agreed on utilizing a set of OFDM numerologies to handle a wide range of frequencies and deployment options [44, 91–95]. Using the LTE subcarrier spacing of $\Delta f = 15$ kHz as the base numerology, the other numerologies are scaled from the base numerology according to the following factor: 15×2^n kHz, where n is an integer. Thus, using a common factor, OFDM slots and symbols of different numerologies are aligned in the time domain and frequency domain. Table. 1.1 shows five different numerologies for 5G NR.

Another drawback of OFDM is the large spectrum sidelobes that cause high out-of-band radiation which results in adjacent channel interference. Since the radio spectrum is a limited resource, spectral confinement is essential to efficiently utilize the available spectrum. The radio spectrum is allocated to different users (also called *primary users* (PUs)). However, the licensed spectrum is underutilized, resulting in spectrum wastage [96]. Cog-

OFDM numerology	15 kHz	30 kHz	60 kHz	120 kHz	240 kHz
Frequency band	0.45–6 GHz	0.45–6 GHz	0.45–6 GHz 24–52.6 GHz	24–52.6 GHz	24–52.6 GHz
OFDM symbol duration	66.67 μs	33.33 μs	16.67 μs	8.33 μs	4.16 μs
Cyclic prefix duration	4.69 μs	2.34 μs	1.17 μs	0.59 μs	0.29 μs
Total OFDM symbol duration	71.35 μs	35.68 μs	17.84 μs	8.91 μs	4.45 μs
Maximum bandwidth	50 MHz	100 MHz	200 MHz	400 MHz	800 MHz

Table 1.1: Different numerologies proposed for 5G NR [2].

nitive radio (CR) is a key enabling technology to improve the RF spectrum by utilizing the spectrum efficiently in an opportunistic manner without interfering with the primary users [97–100]. In CR, secondary users (SUs) (which are unlicensed users) are allowed to utilize the unused spectrum holes (also referred to as white space) of PUs at any time, provided that they do not cause harmful interference to the primary users, and the spectrum leakage of SUs must be below a certain threshold [101–103]. Thus, the sidelobes of OFDM need to be drastically reduced to operate in the white spaces without causing interference to the primary user.

The sidelobe suppression is also necessary for the coexistence of multiple users, different services, and scenarios in 5G. Since 5G will cater to various services and scenarios on a single block of spectrum, it is crucial to reduce the spectral leakage to the adjacent channels in order to efficiently utilize the spectrum. Moreover, using different numerologies in adjacent bands may cause interference to each other, since the subcarriers in adjacent bands are not orthogonal to each other. This inter-numerology interference (INI), may significantly degrade performance [93–95].

Thus, it is of paramount importance to reduce the large sidelobes of OFDM for the coexistence of different services and scenarios in 5G and cognitive radio networks. The radiated power must be efficiently minimized to reduce adjacent channel interference. In addition, the OBR reduction techniques should achieve adequate OBR reduction with considerably low computational complexity and high spectral efficiency. Motivated by the above considerations, this thesis presents various OBR reduction techniques for suppressing the OFDM sidelobes to reduce unwanted emissions.

1.3. OBR reduction techniques

Many OBR reduction techniques have been proposed in literature over the years, and each has its advantages and drawbacks. In general, the performance of an OBR reduction technique is measured by its ability to

suppress out-of-band emission. However, besides OBR reduction, some other key performance parameters are critical for OBR reduction techniques as discussed below.

- **Computational complexity** plays a vital role in practical implementation, especially in limited-power battery-operated devices. The computational complexity of an OBR reduction technique can be split into two parts: online complexity and offline complexity. The online complexity is given by the computations needed at the transmitter and receiver, in terms of complex operations per OFDM symbol. On the other hand, offline complexity is the number of operations required to find the coefficients of an OBR reduction technique. Generally, this is performed once as long as the system parameters remain unchanged.

- **Spectral efficiency** is another critical performance indicator for OBR reduction methods. The available time and frequency resources must be utilized efficiently in order to increase the throughput which is measured in bits/s/Hz. However, some OBR reduction techniques reserve a number of subcarriers for OBR suppression or transmitting side information to the receiver. These subcarriers do not carry data, thus reducing the system throughput and degrading the spectral efficiency. Moreover, some OBR reduction techniques increase the OFDM symbol duration which also reduces the efficiency and throughput of the system.

- **In-band distortion** is introduced when an OBR reduction technique modifies the data subcarriers to suppress the sidelobes. This operation is not transparent to the receiver, and appropriate decoding may be required at the receiver side to avoid symbol error rate (SER) degradation. Consequently, the complexity increases due to the decoding operation.

- **Spectrum overshoot** is undesirable in practice, and the large spurs can be a limiting factor for OBR reduction techniques since in practice spectral emission masks impose strict limits to the maximum value of the PSD of the transmitted signal within its passband.

To alleviate the OBR problem of OFDM, numerous techniques have been proposed in the literature, which can be broadly categorized as *frequency-domain* and *time-domain* methods.

1.3.1. Frequency domain techniques

Frequency-domain techniques for OBR reduction operate at the input of inverse fast Fourier transform (IFFT) and modify the samples before IFFT operation. Guard band insertion is one of the simplest methods to reduce OBR by simply deactivating subcarriers at the edges of the spectral band. This simple method reduces sidelobes asymptotically with f^{-2}; however, this comes at the cost of spectral efficiency, and the OBR reduction is insufficient without allocating a large number of null subcarriers [13, 104, 105].

The method known as Multiple choice sequences (MCQ) maps the original transmission sequence onto a set of sequences for OBR reduction [106, 107]. For a successful detection and demapping of the signal, an index is transmitted to identify the selected sequence. The side information causes system overhead and reduced data throughput. Subcarrier Weighting (SW) techniques multiply the subcarriers by an optimal set of weights to minimize the OBR [108, 109]. However, these data-dependent techniques require to solve an optimization problem for each OFDM symbol; therefore, they are computationally expensive and suffer from symbol error rate (SER) degradation. Similarly, constellation expansion (CE) and phase adjustment techniques are data-dependent and suffer from high complexity [110, 111].

Active interference cancellation (AIC) is another frequency-domain method that modulates some reserved subcarriers (also commonly known as *cancellation subcarriers*) with appropriate combinations of the symbols transmitted on data subcarriers [112–117]. Generally, these R reserved cancellation subcarriers are placed on the spectrum edges to reduce the out-of-band emission, although their positions can be optimized for better performance [114]. AIC techniques are transparent to the receiver; thus, the receiver simply discards cancellation carriers, and data subcarriers are demodulated. On the other hand, AIC techniques have limited performance in terms of OBR reduction and may suffer from spectral peaks.

Spectral precoding [118–138] is another popular frequency-domain technique to suppress the sidelobes in OFDM. Spectral precoding can be regarded as a generalization of AIC methods in which all the K available subcarriers (and not just the reserved ones) are modulated with some function of data symbols. The number of data-carrying symbols per OFDM block is $K - R$, where $R \geq 0$ is the *redundancy* of the precoder. In general, larger redundancy values result in better sidelobe suppression, although at the price of reduced spectral efficiency. Generally, spectral precoding is more effective than AIC in suppressing the out-of-band emission; however, the precoding operation is not transparent to the receiver since precoding introduces some in-band distortion, so appropriate decoding may be required at the receiver

end in order to avoid symbol error rate (SER) degradation.

Based on the structure of precoders, they can be classified as either linear or non-linear. A non-linear precoder modulates the subcarriers with some non-linear function of the data to reduce the OBR; for example, the designs in [106, 108, 113, 120] constitute as non-linear approaches for sidelobe suppression. On the other hand, with linear precoding the samples modulated on the available subcarriers are linear functions of the data symbols. In general, linear precoder designs result in more tractable problems, and in addition, under certain assumptions it can be shown that they incur no loss of optimality [139]. Intuitively, this can be linked to the fact that OBR is a second-order statistic, i.e., the transmitted power over a given subband. For these reasons, in this thesis we will focus on linear precoding schemes. Broadly speaking, linear precoders can be classified based on the structure of the precoding matrix as *orthogonal* or *non-orthogonal*.

In orthogonal precoding [123, 124, 126, 127], the precoding matrix has size $K \times (K-R)$, and its $K-R$ columns are orthonormal; in other words, it is a *semi-unitary matrix.* To avoid excessive degradation of spectral efficiency, the redundancy $R > 0$ should be as small as possible, but on the other hand larger values of R provide additional degrees of freedom that can be used to improve OBR reduction. The fact that the precoder is semi-unitary allows straightforward decoding at the receiver without enhancing the noise, by merely multiplying the received vector by the conjugate transpose of the precoding matrix. However, orthogonal precoders generally suffer from complexity. Although an efficient online implementation for orthogonal precoding via Householder block reflectors has been proposed in [140]. On the other hand, all the frequency-domain techniques which do not have an orthogonal structure in the precoding matrix can be termed as non-orthogonal precoders. In general, non-orthogonal precoding techniques may suffer from some in-band distortion which may degrade the system SER.

The aforementioned spectral precoding structures may have different design criteria to suppress the OFDM sidelobes; thus the techniques can also be classified according to the design criterion. Notch-based precoders place spectral nulls at some selected out-of-band notch frequencies to reduce the sidelobes. The selection of notch frequencies is done manually, and it may not be straightforward to pick them as there is no guarantees about spectral suppression of other frequencies. However, notch-based precoders achieve better spectral efficiency with redundancy $R = 0$, but they suffer from in-band distortion, and the amount of distortion increases with the number of notch frequencies [118, 119]. The mask compliant precoder [120] was proposed to reduce the in-band distortion; however, it suffers from high complexity as it requires solving an optimization problem for each OFDM

block, and even for a low-complexity alternative, the online complexity remains a problem [121]. To reduce the complexity, a data-independent design was proposed in [122]. Instead of solving an optimization problem for each block, a fixed matrix is used to obtain the transmit symbols from data symbols, thus reducing the online complexity. However, precoded symbols are computed by $K \times K$ matrix multiplication per data block, which can be computationally expensive when a large number of subcarriers are used. Orthogonal notch-based precoders were also proposed [126, 141] to improve the SER performance, however complexity still remains a problem and the spectral efficiency is reduced. Thus, in general notch-based precoders achieve the OBR reduction at the cost of SER degradation and/or complexity.

Another spectral precoder design criterion is N-continuity, which is based on the observation that the slow sidelobe decay of the multicarrier PSD is mainly due to discontinuities of the time-domain signal at the boundaries between consecutive blocks. Thus, intuitively, imposing continuity of the signal and its first N derivatives at these time instants should result in faster-decaying sidelobes. In [128], reserved subcarriers were used to impose the continuity conditions, whereas in [129], the precoder is a linear precoder with memory of 1 OFDM symbol and no redundancy (which translates into SER degradation). These techniques achieve considerable OBR reduction at the cost of high complexity, SER degradation, and/or spectral spurs. To reduce complexity, cancellation tones were used in [130], which degrades the spectral efficiency. A selected mapping technique was introduced to reduce the spectral peaks and to improve SER performance at the expense of increased complexity [131]. Different improvements were proposed to minimize the in-band distortion to improve the SER performance [132–134]. The design in [127, 142] imposed continuity and multiplexed the data symbols orthogonally to achieve significant suppression of sidelobes and avoid SER degradation; however, it suffers from reduced throughput.

Rather than placing nulls at the prespecified frequencies or imposes continuity, *total suppression criterion* (TSC) design aims to minimize the total out-of-band transmitted power in OFDM [123–125]. TSC-based precoders minimize the out-of-band radiation leakage in the out-of-band frequency region. Moreover, it offers additional flexibility because it allows to fine-tune the precoder to different situations (e.g. in CR systems one may need to vacate different portions of the passband).

Several other precoder designs have also been proposed according to different criteria to suppress the OFDM sidelobes. Correlatively codes were used to introduce correlation to each data block before OFDM modulation which results in fast decay of the sidlobes [135]. However, the SER performance degrades remarkably because the correlative codes breaks the

orthogonality among multiplexed symbols. Orthogonal codes were proposed in [136] to improve the SER performance, nevertheless it suffers from high complexity at transmitter and receiver, even for a loss complexity design [137], it still remains a concern. A mapping based precoder was propsoed in [138], which maps antipodal symbol pair onto two adjacent subcarriers to suppress the OFDM sidelobes, however it suffers from limited OBR performance.

1.3.2. Time domain techniques

Time-domain schemes directly modify the samples at the output of the IFFT operation. Traditionally filtering is used to suppress the out-of-band emission, but it usually requires filters with long impulse responses, which significantly reduces the effective guard interval of OFDM symbols [143]. Instead of using a fixed filter, adaptive symbol transition (AST) adaptively optimizes the signal transition based on transmitted data [144]. AST extends the OFDM symbols and the extension is used to smooth the transition between consecutive symbols to suppress OFDM sidelobes similar to that N-continuity designs. AST suffers from computationally-heavy optimization as it needs to solve an optimization problem for each OFDM symbol. Moreover, the increase in symbol duration reduces efficiency. To improve the efficiency and data throughput, a phase adjustment approach was proposed in [145], where the phase of each OFDM symbol is adjusted to minimize the OBR emission. Since phase adjustment approach does not need explicit side information to be sent to the receiver, thus data throughput is not decreased. However, it has limited OBR performance, and similar to AST, the phase adjustment approach also suffers from high online complexity.

Another effective time-domain approach to minimize the unwanted emission is *windowing*, also referred to as weighted overlap-add (WOLA) or windowed OFDM (W-OFDM) [44, 146]. The objective of such techniques is to replace the typical standard rectangular pulse in CP-OFDM by a window with soft edges, thus gradually reducing the amplitude of the two edges of an OFDM symbol and making a smooth transition between two OFDM symbols, resulting in much sharper sidelobe decay in the frequency domain. Additionally, the complexity of windowing is relatively less than that of other OFDM-derived waveforms and does not suffer from peak-to-average power ratio (PAPR) issues [147]. A number of different window functions, e.g., raised cosine (RC), Blackman, Hanning, and Hamming can be used for windowing operation [13, 105, 148]. Assuming that the cyclic prefix length remains the same to tackle the channel's delay spread and avoid ISI, the OFDM symbol length needs to be extended because of the newly intro-

duced pulse edges. Thus, the aforementioned windowing techniques obtain the OBR reduction at the cost of efficiency because of increased symbol length. To improve the efficiency, [149] proposed to perform the windowing operation before CP, unlike the traditional windowing methods; however, this process introduces ICI, and an appropriate equalizer is required at the receiver to combat ICI; consequently, the complexity increases.

To enhance sidelobe suppression, it is possible to combine various techniques in both time and frequency domains. One proposed approach involves combining frequency domain methods, such as multiple-choice sequences (MCS), cancellation carrier (CC), or subcarrier weighting (SW), with time domain windowing, as suggested by Brandes et al. [150].

The combination of SW and windowing provides a modest improvement in OBR. The combination of MCS with windowing has slightly better performance but may lead to a decrease in spectral efficiency. The combination of CC and windowing has been found to achieve the best results; however, it can also reduce spectral efficiency due to the use of CC and windowing techniques. Another proposed technique to suppress OFDM sidelobes involves combining the frequency domain AIC method with time-domain shaping pulses, as suggested by Diez [68]. This technique has been shown to comply with the stringent PSD mask imposed by EN 50561-1, which is a European standard for EMC, and ITU-T Rec. G.9964, which is a standard for powerline communication (PLC). However, it may suffer from increased computational complexity.

To summarize, a plethora of time-domain and frequency-domain techniques have been proposed over the years to suppress the large sidelobes of OFDM, which lead to out-of-band radiation. All these techniques have their own advantages and shortcomings. The OBR reduction is achieved at the cost of one or more of the performance parameters: computational complexity, spectral efficiency, spectral peaks, and/or symbol error rate. For example, the OBR reduction achieved by techniques such as guard band insertion, multiple choice sequences, and windowing is at the cost of efficiency. Data-dependent techniques like subcarrier weighting, constellation expansion, phase adjustment, and adaptive symbol transition pay the price in terms of high complexity and/or symbol error rate. The cost for AIC techniques is in terms of spectral peak and spectral efficiency. Spectral precoders achieve OBR reduction at the expense of spectral efficiency, complexity, and/or symbol error rate.

Thus, there is a tradeoff between the aforenamed key performance indicators (KPIs), and the tradeoffs are not the same for each OBR reduction technique. Moreover, depending on applications, use-case scenarios, par-

ticular spectral emission masks, and available resources, one may want to sacrifice OBR performance in exchange for an improvement in another key indicator or vice versa. Hence, trading off among KPIs is of paramount importance to meet the diverse requirement of various use-case scenarios. In addition, many sidelobe suppression methods lacks flexibility because they do not allow users to choose the frequency range of interest over which OBR reduction is to be emphasized.

Motivated by the above considerations, in this thesis, we propose a number of novel designs to suppress the OBR in multicarrier systems to avoid adjacent channel interference. These designs provide the flexibility to choose the range of frequencies through a spectral weighting function in order to emphasize some frequency ranges over others. The proposed designs are a generalization of the TSC criterion presented before, and can be understood as a weighted TSC criterion. The goal is to minimize the OBR over a user-selectable frequency region. In other words, the designs of the thesis are PSD-based rather than N-continuous based or notch-based. Furthermore, the proposed designs are flexible enough to allow the tradeoff mentioned above between the KPIs: OBR, complexity, symbol error rate, spectral peaks and spectral efficiency, to meet the diverse requirements of different applications and scenarios. In addition, all of the proposed designs are data-independent and can be computed offline. More specifically, the salient features of the proposed designs in the thesis can be summarized as follows:

- Windowing is an effective time domain approach to suppress OBR. It benefits from having low complexity and being receiver agnostic. However, due to the fixed window, traditional windowing approaches lack the flexibility to shape the power spectral density to focus on OBR at the frequency ranges of interest. Thus, we propose an optimal window design that trades off OBR performance between different frequency regions according to the system requirements, i.e., it may be useful to gain more OBR reduction near the spectrum edges at the expense of OBR in the far away frequencies.

- Spectral precoding is a popular frequency domain approach to tackle the OBR. In general, spectral precoding provide high OBR reduction at the expense of high complexity. However, certain applications are more concerned about the complexity, especially battery-operated or low-power devices. Thus it may be beneficial to sacrifice OBR in exchange for lower complexity, as long as the OBR satisfies the spectral emission mask. We present a novel precoding approach that judiciously controls the amount of distortion on data subcarriers by a user-selectable parameter, which in turn determines receiver complexity. Moreover, the proposed spectral precoder design minimizes the

OBR over a given frequency range.

- Spectral precoding and windowing are two effective approaches to reduce out-of-band radiation (OBR) in multicarrier systems. Their performance comes at the price of reduced throughput and additional computational complexity, so there is strong motivation for simultaneously using both techniques. We present a novel design that jointly optimizes the precoder and window coefficients to minimize radiated power within a user-selectable frequency region. The proposed design achieves a better OBR/throughput/complexity tradeoff than either of these individual techniques separately.

- Reducing the large sidelobes of multicarrier signals, especially in techniques like active interference cancellation (AIC) or orthogonal precoding, is at the expense of spectral efficiency. Introducing memory may be promising to improve the OBR performance without sacrificing additional spectral efficiency at the cost of an increase in computational complexity. Similar to the previously proposed designs, the novel memory-based precoder minimizes the total OBR within a user-selectable frequency region. Moreover, the proposed technique can achieve various levels of OBR by controlling the spectral peaks.

1.4. Contributions

This thesis has the following scientific contributions, and each one is presented in the following chapters. The list of contributions is shown below.

- **Design an optimal window for cyclic-prefix based orthogonal frequency division multiplexing**

  In this chapter, we presented a flexible window design to minimize the OBR in a given user-selectable frequency region. The proposed method can tradeoff OBR between different ranges of frequencies, and depending on the application; more OBR can be achieved in the frequency of interest. It is a data-independent design since the window is computed offline. Simulation results show that the optimal window design can achieve various levels of OBR reduction in different frequency ranges. Moreover, the proposed technique can reduce inter-numerology interference (INI) in 5G systems.

- **A novel spectral precoding technique to suppress the sidelobes for OFDM systems**

This chapter presents novel spectral precoding techniques to reduce out-of-band radiation (OBR) in multicarrier systems to avoid adjacent channel interference. The proposed designs are flexible to tradeoff OBR reduction, complexity, and error rate, by judiciously choosing the level of distortion on data subcarriers. Since precoding introduces distortion in the signal, appropriate decoding is proposed at the receiver end to avoid error rate degradation. Results show that the proposed designs can satisfy the requirements of a wide variety of systems with different levels of complexity. In addition, it reduces the online complexity significantly with adequate OBR performance.

- **Design a joint precoder and window scheme to suppress the OFDM sidelobes**

  This chapter presents a novel design that jointly optimizes the precoder and window coefficients to minimize out-of-band power within a user-selectable frequency region. The combination of spectral precoding and windowing can improve the OBR performance compared to standard precoding but with much less online complexity. Moreover, the design coefficients can be computed offline. Results show that the proposed design achieves a better tradeoff between OBR/efficiency/complexity than either of these individual techniques separately.

- **Using memory for improving the OBR performance of spectral precoders**

  In this chapter, novel memory-based spectral precoder designs are proposed to minimize the OBR in the frequency region of interest through a spectral weightage function. The proposed techniques improve OBR performance without sacrificing additional spectral efficiency at the cost of extra computational complexity. Simulation results show that the proposed memory-based designs improve the OBR performance and effectively control the spectral overshoot.

1.5. Signal Model for OFDM

Consider a CP-OFDM signal generated from a N-IFFT and a cyclic prefix of size N_{cp} samples. There are K active subcarriers with indices $\mathcal{K} = \{k_1, k_2, \cdots, k_K\}$. Let $x_k[m]$ be the data modulated on the k-th subcarrier in the m-th symbol, then the baseband samples of the multicarrier signal are given by

$$s[n] = \sum_{m=-\infty}^{\infty} \sum_{k \in \mathcal{K}} x_k[m] h_{\mathrm{P}}[n - mL] e^{j\frac{2\pi}{N}k(n-mL)}, \tag{1.1}$$

where L is the hop size in samples, and h_{P} is the shaping pulse. In standard CP-OFDM with rectangular pulse shape one has $h_{\mathrm{P}}[n] = 1$ for $n \in \{0, 1, \ldots, L-1\}$ and zero otherwise, so that the CP length is $N_{cp} = L - N$. Let $\Delta f = \frac{1}{NT_s}$ be the subcarrier spacing with the sampling frequency $f_s = \frac{1}{T_s}$, then the baseband continuous-time multicarrier signal is obtained at the output of a digital-to-analog converter (DAC) is

$$s(t) = \sum_{n=-\infty}^{\infty} s[n] h_{\mathrm{I}}(t - nT_s), \tag{1.2}$$

where $h_{\mathrm{I}}(t)$ is the impulse response of the interpolation filter in the Digital-to-Analog Converter (DAC). Let the Fourier transforms of shaping pulse and DAC interpolation filter respectively be:

$$H_{\mathrm{P}}(e^{j\omega}) = \sum_{n} h_{\mathrm{P}}[n] e^{-j\omega n} \qquad \text{and} \qquad H_{\mathrm{I}}(f) = \int_{-\infty}^{\infty} h_{\mathrm{I}}(t) e^{-j2\pi ft}\, dt. \tag{1.3}$$

Let us define the following terms:

$$\phi_0(f) \triangleq H_{\mathrm{P}}^*(e^{j2\pi f T_s}) \tag{1.4}$$

$$\phi_k(f) \triangleq \phi_0(f - k\Delta f) \tag{1.5}$$

$$\boldsymbol{\phi}(f) \triangleq [\ \phi_{k_1}(f) \quad \phi_{k_2}(f) \quad \cdots \quad \phi_{k_K}(f)\ ]^T. \tag{1.6}$$

Let the vector $\boldsymbol{x}[m] = [\ x_{k_1}[m] \quad x_{k_2}[m] \quad \cdots \quad x_{k_K}[m]\ ]^T \in \mathbb{C}^K$ collect the transmit symbols in the m-th block. It is assumed that $\boldsymbol{x}[m]$ is zero-mean and wide-sense stationary, so that the CP-OFDM signal $s(t)$ in (1.2) is cyclostationary with period LT_s. Then the power spectral density (PSD) of baseband multicarrier signal $s(t)$ is given by [151]

$$S_s(f) = \frac{|H_{\mathrm{I}}(f)|^2}{LT_s} \boldsymbol{\phi}^H(f) \boldsymbol{S}_x(Lf) \boldsymbol{\phi}(f), \tag{1.7}$$

where $\boldsymbol{S}_x(f) = \sum_{\ell} \mathbb{E}\{\boldsymbol{x}[m]\boldsymbol{x}[m-\ell]^H\} e^{-j2\pi f T_s \ell}$.

The PSD expression (1.7) reveals the influence of the three elements featuring in the synthesis of the multicarrier signal:

- **Shaping pulse**. The shaping pulses affect the vector $\boldsymbol{\phi}(f)$. More specifically, the vector $\boldsymbol{\phi}(f)$ has shifted replicas of their transfer functions to the positions of the active subcarriers $\{k\Delta f \mid k \in \mathcal{K}\}$. In standard CP-OFDM a rectangular pulse is used where $\phi_0(f) \triangleq L e^{j\pi f T_s (L-1)} \cdot \frac{sinc(fT_s L)}{sinc(fT_s)}$. In general, the shaping pulse can be designed to shape the transmitted signal PSD.

- **Precoding**. The transmitted signal PSD (1.7) also depend on the matrix $\boldsymbol{S}_x(Lf)$, which can be designed to shape the transmitted signal PSD via precoding. The transmitted sequence $\boldsymbol{x}[m]$ can be obtained from the data samples through a precoding operation to shape the PSD according to the requirements.

- **Interpolation filter**. The effect of the DAC interpolation filter is to remove the undesired replicas present in the term $\boldsymbol{\phi}^H(f)\boldsymbol{S}_x(Lf)\boldsymbol{\phi}(f)$, which is periodic in f with period equal to the sampling rate f_s.

The transmit samples $\boldsymbol{x}[m] \in \mathbb{C}^K$ are obtained from data sample $\boldsymbol{d}[m] \in \mathbb{C}^{K_d}$, where $K_d \leq K$. The data sequence $\boldsymbol{d}[m]$ is assumed to be zero-mean with covariance

$$\mathbb{E}\{\boldsymbol{d}[m]\boldsymbol{d}^H[m']\} = \delta[m-m']\boldsymbol{C}, \tag{1.8}$$

where $\boldsymbol{C}$ is positive definite. For a memoryless linear precoder, the transmitted $\boldsymbol{x}[m]$ are generated from the data samples $\boldsymbol{d}[m]$ as

$$\boldsymbol{x}[m] = \boldsymbol{G}\boldsymbol{d}[m] \tag{1.9}$$

where $\boldsymbol{G} \in \mathbb{C}^{K\times K_d}$ is a precoding matrix. Since $\boldsymbol{d}[m]$ is assumed to be zero-mean with covariance $\boldsymbol{C} = \boldsymbol{I}$, $\boldsymbol{x}[m]$ is also zero-mean with $\mathbb{E}\{\boldsymbol{x}[m]\boldsymbol{x}^H[m']\} = \delta[m-m']\boldsymbol{G}\boldsymbol{G}^H$. Throughout the thesis we will assume memoryless precoders except in Chapter 5, where development of the PSD expression will be extended to accommodate memory precoders.

To proceed forward, we will drop the dependence of the vectors $\boldsymbol{x}[m]$, $\boldsymbol{d}[m]$, etc., on the symbol index m, and write simply $\boldsymbol{x}$, $\boldsymbol{d}$, etc., unless stated otherwise. For a memoryless linear precoder (1.9), the PSD in (1.7) becomes

$$\begin{aligned} S_s(f) &= \frac{|H_{\mathrm{I}}(f)|^2}{LT_s} \cdot \boldsymbol{\phi}^H(f)\boldsymbol{G}\boldsymbol{G}^H\boldsymbol{\phi}(f) \\ &= \mathrm{tr}\{\boldsymbol{G}^H\boldsymbol{\Phi}(f)\boldsymbol{G}\}, \end{aligned} \tag{1.10}$$

where

$$\boldsymbol{\Phi}(f) \triangleq \frac{|H_{\mathrm{I}}(f)|^2}{LT_s}\boldsymbol{\phi}(f)\boldsymbol{\phi}^H(f) \in \mathbb{C}^{K\times K} \tag{1.11}$$

is Hermitian with rank one. Let $W(f) \in [0,1] \forall f$ be a spectral weighting function that puts emphasis on frequency ranges of interest over which OBR reduction is important. In the simplest case, if $\mathbb{B} \subset \mathbb{R}$ is the set of frequencies over which OBR is to be minimized, one can take $W(f) = 1$ for $f \in \mathbb{B}$ and zero otherwise. Then, the weighted power is given by

$$\mathcal{P}_W = \int_{-\infty}^{\infty} W(f)S_s(f)df \;=\; \mathrm{tr}\{\boldsymbol{G}^H\boldsymbol{A}_W\boldsymbol{G}\}, \tag{1.12}$$

where we have introduced the $K \times K$ positive (semi-)definite matrix

$$\boldsymbol{A}_W \triangleq \int_{-\infty}^{\infty} W(f)\boldsymbol{\Phi}(f)df. \tag{1.13}$$

The total transmit power can be found as

$$\mathcal{P}_T = \mathrm{tr}\{\boldsymbol{G}^H \boldsymbol{A}_T \boldsymbol{G}\}, \tag{1.14}$$

where

$$\boldsymbol{A}_T \triangleq \int_{-\infty}^{\infty} \boldsymbol{\Phi}(f)df. \tag{1.15}$$

The goal is to minimize $\mathcal{P}_W$ in (1.12) with respect to precoder and/or pulse shape, subject to appropriate constraints and for a given spectral weighting function; and at the receiver end, an appropriate decoder to avoid symbol error rate degradation.

1.6. Publications

The above contributions of the thesis resulted in the following publications:

- **Design an optimal window for cyclic-prefix based orthogonal frequency division multiplexing**
  - K. Hussain and R. López-Valcarce, Optimal Window Design for W-OFDM in 45th IEEE International Conference on Acoustics, Speech and Signal Processing (ICASSP), 2020, pages 5275-5289, May 2020, Barcelona, Spain.
- **A novel spectral precoding technique to suppress the sidelobes for OFDM systems**
  - K. Hussain, A. Lojo and R. López-Valcarce, Flexible Spectral Precoding for Sidelobe Suppression in OFDM Systems, in 44th IEEE International Conference on Acoustics, Speech and Signal Processing (ICASSP), 2019, pages 4789-4793, May 2019, Brighton, UK.
  - K. Hussain and R. López-Valcarce, OFDM Spectral Precoding With Per-Subcarrier Distortion Constraints, in 27th European Signal Processing Conference (EUSIPCO), 2019, pages 1-5, September 2019, A Coruña, Spain.

- **Design a joint precoder and window scheme to suppress the OFDM sidelobes**

  - K. Hussain and R. López-Valcarce, Joint Precoder and Window Design for OFDM Sidelobe Suppression, in IEEE Communications Letters, 2022.

- **Using memory for improving the OBR performance of spectral precoders**

  - K. Hussain and R. López-Valcarce, Memory Tricks: Improving Active Interference Cancellation for Out-of-Band Power Reduction in OFDM, in 22nd IEEE International Workshop on Signal Processing Advances in Wireless Communications (SPAWC), 2021, pages 86-90, September 2021 Lucca, Italy.
  - K. Hussain and R. López-Valcarce, Orthogonal precoding with memory for sidelobe suppression in OFDM, in 30th European Signal Processing Conference (EUSIPCO), 2022, pages , September 2022, Belgrade, Serbia.

1.7. Thesis Structure

The thesis is structured into five chapters, each of which presents the previously mentioned contributions. Chapter 2 introduces a novel window design for OFDM that aims to suppress sidelobes. In Chapter 3, flexible spectral precoding designs are presented with the aim of reducing the unwanted emission of OFDM. Chapter 4 proposes a joint window and precoder design for sidelobe suppression. Chapter 5 introduces the concept of memory for improving the OBR performance of spectral precoders. Finally, Chapter 6 concludes the thesis and outlines future work.

Chapter 2

Window Design for OFDM

This chapter is adapted with permission of the coauthors and the editorial from IEEE: K. Hussain and R. López-Valcarce, Optimal Window Design for W-OFDM in 45th IEEE International Conference on Acoustics, Speech and Signal Processing (ICASSP), 2020, pages 5275-5289, May 2020, Barcelona, Spain.

2.1. Introduction

This chapter presents a novel time-domain technique to mitigate the problem of OBR in OFDM systems. Time-domain methods modify the samples after the IFFT operation. Filtering is the most common time-domain technique to reduce the sidelobes; however, the long filters decrease the effective guard interval of OFDM symbols [143]. Data-dependent methods like adaptive symbol transition suffer from high online complexity [144]. Another approach modifies the phase of samples to reduce the OBR emission but it has limited performance [145].

Weighted overlap-add (WOLA) or windowed OFDM (W-OFDM) [44, 146] is another approach to suppress the large sidelobes. Transmit windowing extends OFDM symbol length and uses a pulse with soft edges at both sides of the symbol replacing the standard rectangular pulse in CP-OFDM. The smooth transition between the consecutive symbols results in sharper decay of the sidelobes, and the consecutive OFDM symbols are now overlapped with each other to comply with the standards, which results in a similar overhead as in the standard CP-OFDM. In general, windowing techniques have low complexity and do not suffer from PAPR issues [147].

Moreover, this operation performed on CP-OFDM at the transmitter side is receiver agnostic [152, 153]. On the other hand, these techniques pay the price in terms of efficiency due to the newly introduced pulse edges, assuming the effective cyclic prefix length, as dictated by the maximum channel delay spread, remains the same. Thus, there is a tradeoff between spectral confinement and efficiency. To improve the spectral efficiency, a time-asymmetric per-subcarrier windowing scheme was proposed in [154] which uses a portion of the existing CP for the window transition. However, inter symbol interference (ISI) is introduced due to the reduced CP size. The interference can be minimized by designing a time-asymmetric pulse shape for each subcarrier. Nevertheless, the complexity increases many folds for large number of subcarriers.

Window operation can use different functions, e.g., Blackman, Hamming, Hanning, and raised cosine (RC), which are discussed in [13, 105, 148] along with the classical main lobe width/sidelobe level tradeoff. The most commonly used window is RC because of its straightforward implementation and adequate performance [11]. However, depending on the application, utilized bandwidth, active subcarrier set, etc., it may become useful to flexibly shape the power spectral density in order to focus on OBR at particular frequency regions. For example, depending on the specific spectral emission mask, one may want to sacrifice OBR performance for sufficiently far away frequencies in exchange for a better performance near the transmitted spectrum edges. This cannot be done by using a single fixed window.

Motivated by the above consideration, in this chapter, we present a novel window design that is flexible enough to allow the aforementioned tradeoff. The goal is to minimize the total OBR over a user-selectable frequency region; additionally, spectral weights may be included in the design in order to emphasize some frequency ranges over others. The proposed window can be computed offline; therefore, the optimization process does not incur additional online complexity.

2.2. Signal Model

Consider the model from Sec. 1.5 where an OFDM signal generated from an N-IFFT. The baseband samples of the multicarrier signal are then given by

$$s[n] = \sum_{m=-\infty}^{\infty} \sum_{k \in \mathcal{K}} x_k[m] h_{\mathrm{P}}[n - mL] e^{j\frac{2\pi}{N}k(n-mL)}, \tag{2.1}$$

where L is the hop size in samples, and h_{P} is the shaping pulse. With the introduction of windowing, the length of the pulse $h_{\mathrm{P}}[n]$ is extended

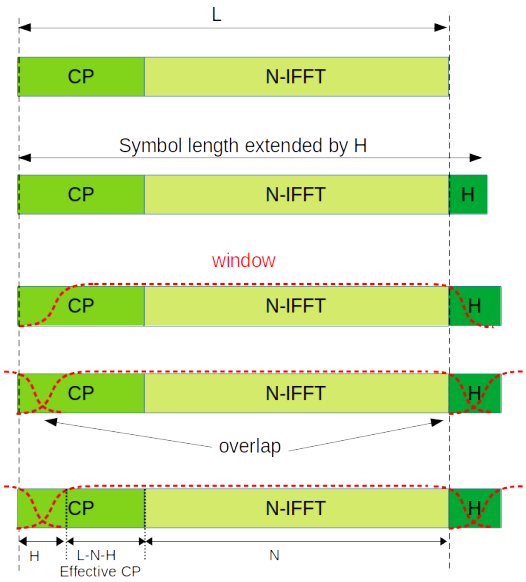

Figure 2.1: Time domain windowing at the transmitter.

H samples with respect to standard CP-OFDM, which uses a rectangular pulse of unit samples for $0 \leq n \leq L-1$, as shown in Fig. 2.1. Thus, $h_{\mathrm{P}}[n]$ is nonzero only for $n \in \{0, 1, \ldots, L+H-1\}$, and there is an overlap of H samples between consecutive blocks in (2.1). In particular, the central samples are still fixed to 1, i.e., $h_{\mathrm{P}}[n] = 1$ for $H \leq n \leq L-1$, the edge samples $h_{\mathrm{P}}[0]$,...,$h_{\mathrm{P}}[H-1]$ and $h_{\mathrm{P}}[L]$,...,$h_{\mathrm{P}}[L+H-1]$ are allowed to take different values. The gradual transition from 0 to 1 of these edge samples results in a sharper PSD [146]. On the other hand, due to the H-sample overlap, the effective CP has been reduced to $N_{CP} = L - N - H$ samples as shown in Fig. 2.1; therefore, for a given effective CP length N_{CP} (determined by the expected channel delay spread), windowing results in a reduction of efficiency by a factor $\frac{N}{L} = \frac{N}{N+N_{CP}+H}$. For $H = 0$ (no windowing), this reduces to the well-known efficiency loss $\frac{N}{N+N_{CP}}$ due to CP insertion. The selection of H implies a tradeoff between throughput efficiency and sidelobe suppression, since larger values of H will result in better spectral confinement of the OFDM signal.

Since there is no precoding operation, all the available K active subcarriers are dedicated to sending data, that is, $K = K_d$, and $\boldsymbol{G} = \boldsymbol{I}_K$ in (1.9). It is also assumed that $\boldsymbol{C} = \boldsymbol{I}$ in (1.8). The power spectral density (PSD) of $s(t)$ from (1.10) can be rewritten as

$$S_s(f) = \frac{|H_{\mathrm{I}}(f)|^2}{LT_s} \boldsymbol{\phi}^H(f)\boldsymbol{\phi}(f). \tag{2.2}$$

At the receiver end, after synchronization, the CP and the H overlapping

samples between consecutive blocks are removed. The samples of active subcarriers are recovered after an N-point FFT and equalization.

2.3. Optimal window design

For a given H, we seek to optimize the free coefficients in the pulse $h_{\mathrm{P}}[n]$ in terms of OBR. To proceed, note that $\boldsymbol{\phi}(f)$ in (1.6) can be rewritten as $\boldsymbol{\phi}(f) = \boldsymbol{M}(f)\boldsymbol{h}$, where $\boldsymbol{h} \in \mathbb{C}^{L+H}$ comprises the conjugate pulse samples:

$$\boldsymbol{h} \triangleq [\ h^*[0] \quad h^*[1] \quad \cdots \quad h^*[L+H-1]\ ]^T, \tag{2.3}$$

and $\boldsymbol{M}(f) \in \mathbb{C}^{K\times(L+H)}$ is given entrywise by

$$[\boldsymbol{M}(f)]_{pq} = e^{j2\pi(q-1)(f-k_p\Delta f)}, \left\{ \begin{array}{rcl} p & = & 1,\ldots,K, \\ q & = & 1,\ldots,L+H. \end{array} \right. \tag{2.4}$$

Thus, the PSD $S_s(f)$ in (2.2) can be rewritten in terms of $\boldsymbol{h}$ as

$$S_s(f) = \frac{|H_I(f)|^2}{LT_s}\boldsymbol{h}^H\boldsymbol{M}^H(f)\boldsymbol{M}(f)\boldsymbol{h}, \tag{2.5}$$

so that the spectrally weighted power in (1.12) becomes

$$\mathcal{P}_W = \int_{-\infty}^{\infty} W(f)S_s(f)\mathrm{d}f = \boldsymbol{h}^H\boldsymbol{Z}\boldsymbol{h}, \tag{2.6}$$

where the matrix $\boldsymbol{Z} \in \mathbb{C}^{(L+H)\times(L+H)}$ is given by

$$\boldsymbol{Z} \triangleq \frac{1}{LT_s}\int_{-\infty}^{\infty} W(f)|H_{\mathrm{I}}(f)|^2\boldsymbol{M}^H(f)\boldsymbol{M}(f)\mathrm{d}f, \tag{2.7}$$

which is Hermitian positive (semi)definite. Then the window design problem for the minimization of $\mathcal{P}_W$ becomes

$$\min_{\boldsymbol{h}} \boldsymbol{h}^H\boldsymbol{Z}\boldsymbol{h} \quad \text{s. to} \quad \boldsymbol{D}^H\boldsymbol{h} = \boldsymbol{1}, \tag{2.8}$$

where $\boldsymbol{D} \in \mathbb{C}^{(L+H)\times(L-H)}$ comprises columns $H+1$ through L of the identity matrix $\boldsymbol{I}_{L+H}$, and $\boldsymbol{1} \in \mathbb{C}^{L-H}$ is the all-ones vector. Note that the constraint $\boldsymbol{D}^H\boldsymbol{h} = \boldsymbol{1}$ is necessary to keep the central $L-H$ window taps equal to 1. This guarantees that the central OFDM symbol samples remain unmodified, thus ensuring a system without Symbol Error Rate (SER) degradation. The solution of this convex minimization problem can be readily found in closed form (see details in Appendix A).

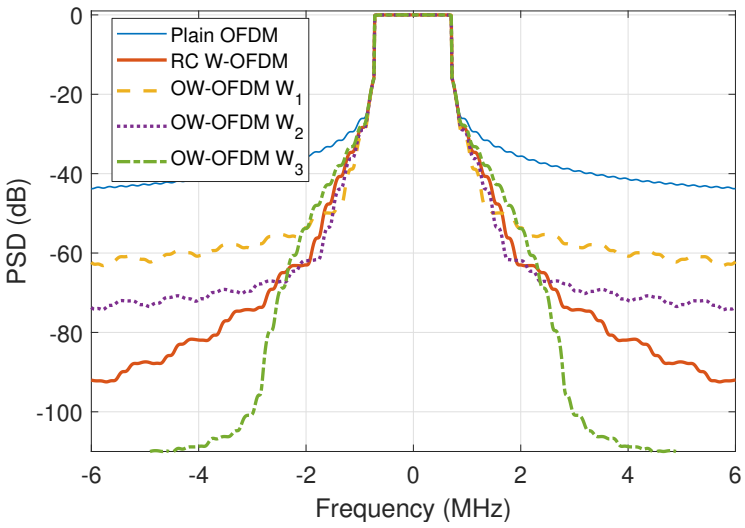

Figure 2.2: PSD of OW-OFDM, RC W-OFDM and CP-OFDM for $H = 1/4$ CP and different spectral weighting functions.

2.4. Results and Discussion

The proposed window design provides flexibility to achieve various levels of OBR reduction in different frequency regions, determined by the chosen spectral weighting function $W(f)$, according to system requirements. Let us consider a CP-OFDM system with subcarrier spacing $\Delta f = 15$ kHz and 7 % CP overhead, as in LTE/5G NR. An ideal lowpass filter $H_{\mathrm{I}}(f)$ is assumed with $H_{\mathrm{I}}(f) = 1$ for $|f| \leq \frac{1}{2T_s}$ and zero otherwise. The IFFT size is $N = 1024$ and the symbol length is $L = 1096$. Fig. 2.2 shows the PSD of the proposed optimum window design (OW-OFDM), along with non-windowed CP-OFDM and raised cosine W-OFDM (RCW-OFDM) for a user with 96 active subcarriers (i.e., 8 resource blocks (RBs) of 12 subcarriers each); the size of the window edge H is set to 1/4 of the CP (18 samples) for both OW-OFDM and RCW-OFDM.

Three different weighting functions were considered:

$$W_1(f) = 1, \quad 1.02 \text{ MHz} \leq |f| \leq 6.5 \text{ MHz}, \tag{2.9}$$

$$W_2(f) = 1, \quad 1.47 \text{ MHz} \leq |f| \leq 6.5 \text{ MHz}, \tag{2.10}$$

$$W_3(f) = 1, \quad 2.82 \text{ MHz} \leq |f| \leq 6.5 \text{ MHz}, \tag{2.11}$$

and $W_i(f) = 0$ elsewhere. The optimum window based on W_1 provides more OBR reduction in the vicinity of the transmitted spectrum edges than the RC window, at the expense of less reduction for $|f| \geq 1.65$ MHz (at which

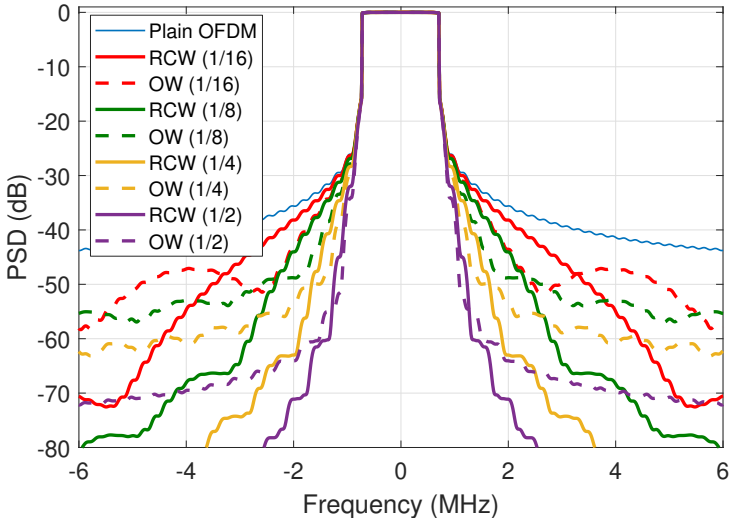

Figure 2.3: PSD of OW-OFDM (dashed), RCW-OFDM (solid) and CP-OFDM (thin solid) for different window overhead values (expressed as a fraction of the CP length).

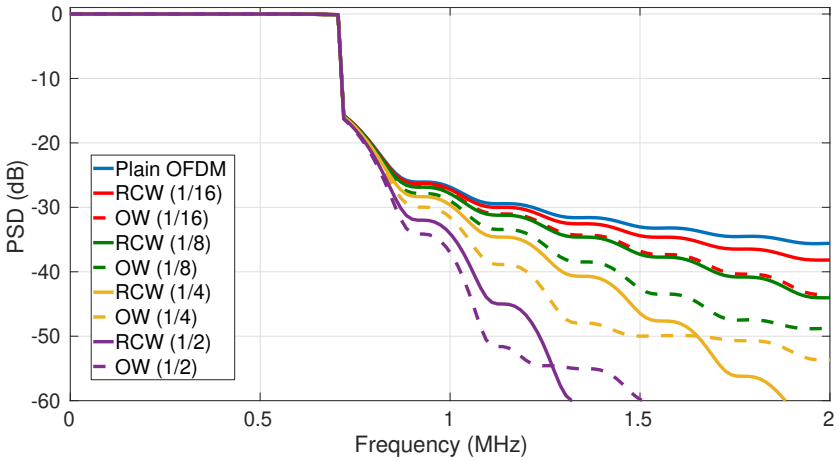

Figure 2.4: PSD of OW-OFDM (dashed), RCW-OFDM (solid) and CP-OFDM (thin solid) for different window overhead values (expressed as a fraction of the CP length).

the PSD is already 50 dB below the passband value). With W_2, the optimal window results in a PSD below that for the RC window for $|f| \leq 2$ MHz, at which 60 dB with respect to the passband have been achieved. However, the PSD for W_1 is below that for W_2 for $|f| \leq 1.48$ MHz. Finally, with W_3 no weight is given to nearby frequencies, and therefore very low PSD values can be attained for distant frequencies in exchange for spectral regrowth closer

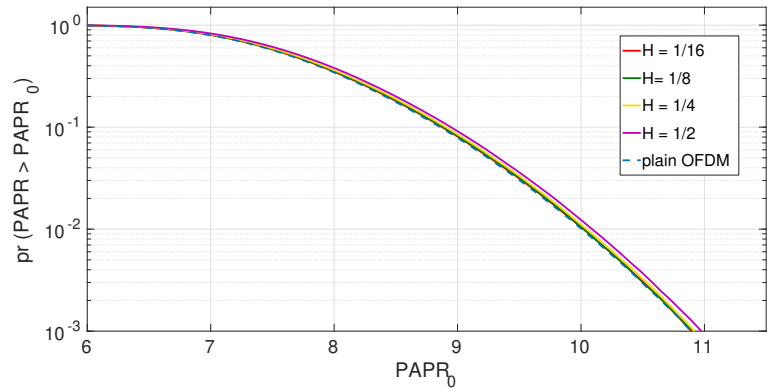

Figure 2.5: PAPR of the proposed OW-OFDM (dahed) for different window overhead values (expressed as a fraction of the CP length).

to the spectrum edges. This illustrates how the proposed optimal window design is flexible enough to accommodate different requirements.

The window edge size H is another critical factor, which directly impacts the performance of the window. Larger values of H provide better OBR reduction at the cost of reduced effective CP, as discussed in Sec. 2.2. Thus, on one hand, H should be small enough to leave a sufficiently long CP to combat multipath, and on the other, it should be large enough to achieve the required OBR reduction. To illustrate this, Fig. 2.3 shows the PSD obtained in the same setting as that of Fig. 2.2 ($\Delta f = 15$ kHz, 7% CP, $N = 1024$, $K = 96$) with an RC window and with the proposed design using weighting function $W_2(f)$ from (2.10), for different values of H. For small window overhead ($H = 1/16$ CP), the PSD of RC W-OFDM decays very slowly and gradually, and the proposed design provides significant improvement for $|f| \leq 3.3$ MHz. This trend continues for increasing values of H, with the frequency at which the PSDs of RCW-OFDM and OW-OFDM cross getting closer to the spectrum edge as seen in Fig. 2.4. We note that OW-OFDM can be further optimized using a different weighting function to achieve OBR requirements in a particular frequency range. Additionally, the proposed OW-OFDM design does not increase the PAPR as evident from the Fig. 2.5, which shows PAPR for different values of window size H (which are expressed as a fraction of CP length) for 16 QAM modulation and weighting function $W_2(f)$.

In the next examples, we consider three cognitive radio scenarios, where the secondary user (SU) is allowed to utilize the spectrum holes of the primary user (PU). In Scenario 1, two spectrum holes are available, each with 225 active subcarriers, situated symmetrically on both sides of the PU frequency band. Scenario 2 also offers two spectrum holes, however, the 482

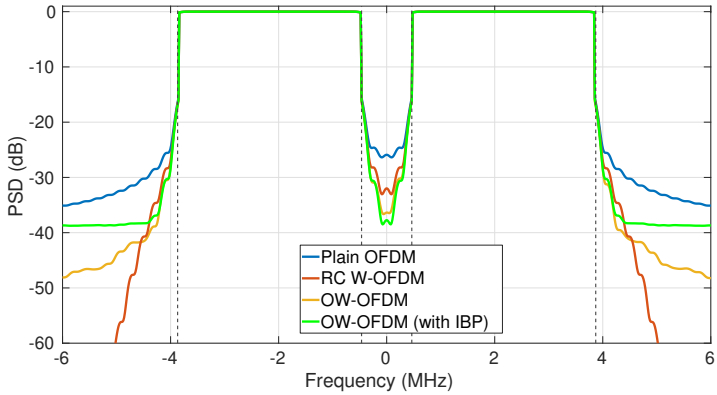

Figure 2.6: PSD of OW-OFDM, RC W-OFDM and CP-OFDM for $H = 1/4$ CP in cognitive radio Scenario 1.

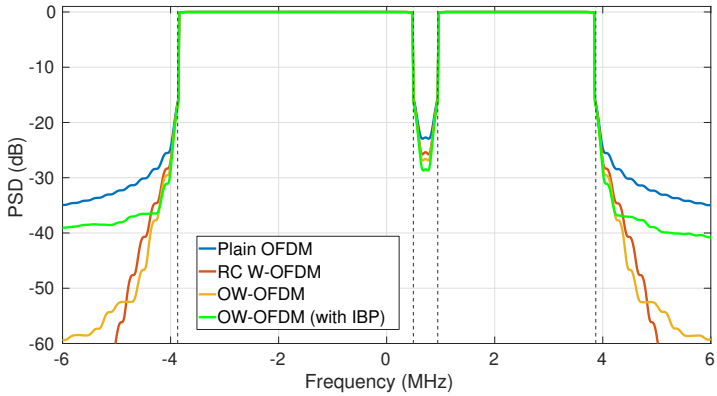

Figure 2.7: PSD of OW-OFDM, RC W-OFDM and CP-OFDM for $H = 1/4$ CP in cognitive radio Scenario 2.

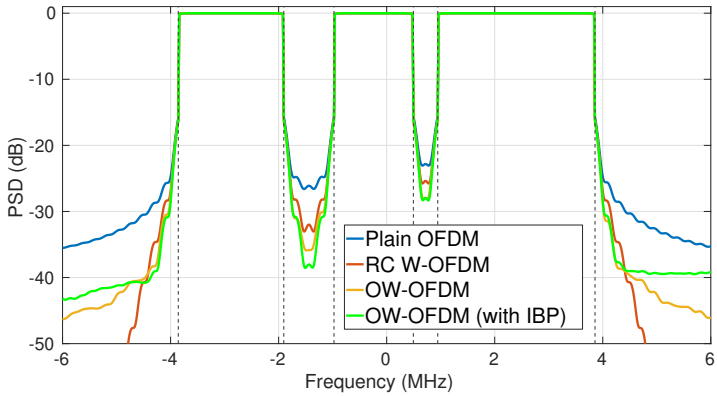

Figure 2.8: PSD of OW-OFDM, RC W-OFDM and CP-OFDM for $H = 1/4$ CP in cognitive radio Scenario 3.

active subcarriers are located in an asymmetrical manner around the PU frequency band. Finally, Scenario 3 has multiple spectrum holes available for the secondary user, with 419 active subcarriers available for transmission. SU has to protect multiple PU subbands which are located within the passband. Assuming the same setting as before i.e., $\Delta f = 15$ kHz, 7% CP, $N = 1024$, and $H = 1/4$ CP. The spectral weighting function is $W(f) = 1 \in \mathbb{B}$ and otherwise zero, where $\mathbb{B}$ includes the set of frequencies in PU band and adjacent channel over which OBR is to be minimized. Fig. 2.6 shows the PSD of the proposed optimum window design (OW-OFDM), along with plain CP-OFDM and RCW-OFDM in the cognitive radio Scenario 1. The proposed OW-OFDM provides more OBR reduction in the protected PU band as compared to the RC window. Moreover, the OW-OFDM design also provides more OBR reduction near the edges of the transmit spectrum as compared to the RC window; however, this reduction is at the cost of less reduction at far away frequencies. The performance can be further improved in the frequency band of the primary user by giving more priority to PSD reduction in the in-band than the adjacent channels. As seen in the Fig. 2.6, the proposed OW-OFDM with in-band priority (IBP) improves the OBR performance in the PU band at the expense of OBR is the adjacent channels. The spectral weighting function for IBP is $W(f) = 1, \{4 \text{ MHz} \leq |f| \leq 6 \text{ MHz}\} \cup \{-0.3 \text{ MHz} \leq f \leq 0.3 \text{ MHz}\}$, and zero elsewhere. Similar results can be seen in Scenario 2 shown in Fig. 2.7, where the proposed OW-OFDM design achieves better OBR reduction in the protected PU band, as well as at the spectrum edges. The spectral weighting function for Scenario 2 is $W(f) = 1, \{4 \text{ MHz} \leq |f| \leq 6 \text{ MHz}\} \cup \{0.555 \text{ MHz} \leq f \leq 0.885 \text{ MHz}\}$, and zero elsewhere. Lastly, Fig. 2.8 show the PSDs of the three designs in the cognitive radio Scenario 3. Clearly, the OW-OFDM design provides better protection to the PU subbands as compared to RCW-OFDM, with $W(f) = 1, \{4 \text{ MHz} \leq |f| \leq 6 \text{ MHz}\} \cup \{-1.8 \text{ MHz} \leq f \leq -1.08 \text{ MHz}\} \cup \{0.555 \text{ MHz} \leq f \leq 0.885 \text{ MHz}\}$, and zero elsewhere.

To quantify performance in a specific interference scenario, consider a setting with two asynchronous users, each of which is assigned 8 RBs (96 subcarriers), and there is no guard band between these two transmissions. We assume $\Delta f = 15$ kHz, 7% CP, $N = 1024$ as before, and $H = 1/4$ CP, so each user can use the windows considered in the setting of Fig. 2.2. Fig. 2.9 shows the signal-to-interference ratio (SIR), defined as the ratio of the PSDs of the signal and the interference when both suffer the same frequency-flat attenuation, for different window choices. It is seen that the proposed design provides better SIR than RC W-OFDM and plain CP-OFDM near edge subcarriers. The use of weight function W_1 (2.9) is likely more meaningful in this setting than W_2 (2.10), since the latter outperforms the former only for very high values of SIR (> 50 dB), a regime in which channel noise, and

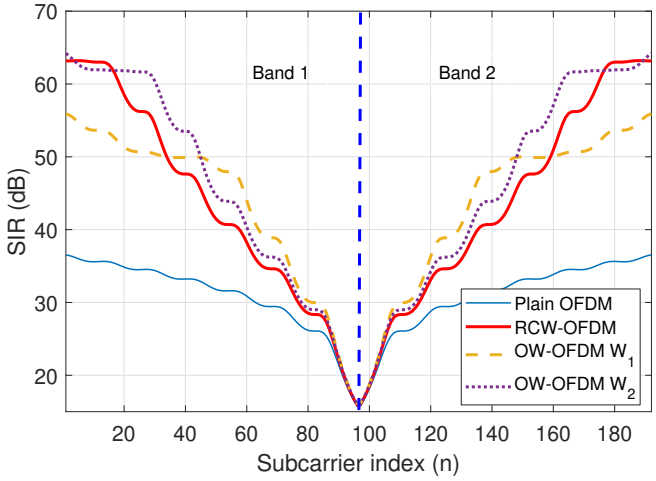

Figure 2.9: Signal-to-Interference Ratio for two asynchronous users with $\Delta f = 15$ kHz. $H = 1/4$ CP.

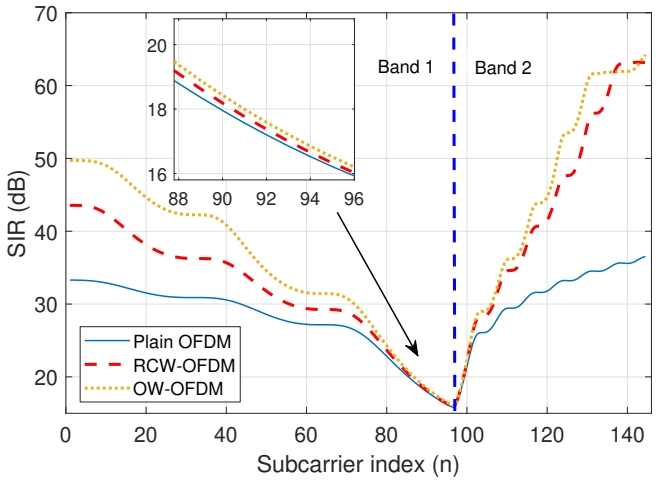

Figure 2.10: Signal-to-Interference Ratio for two adjacent numerologies: $\Delta f_1 = 15$ kHz, $\Delta f_2 = 30$ kHz. $H = 1/4$ CP.

not interference, is likely to be the limiting factor.

5G systems may use different numerologies (i.e., different subcarrier spacings), for different scenarios [95], e.g., using larger subcarrier spacing (hence shorter symbol duration) for low latency or enhanced robustness to phase noise and Doppler spread, and smaller subcarrier spacing (hence longer symbol and CP duration) for settings with long delay spreads, as in large cells. Different services can be frequency-multiplexed by assigning

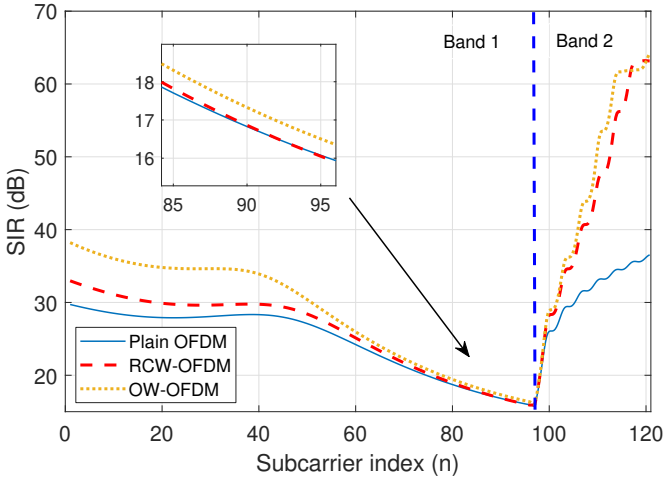

Figure 2.11: Signal-to-Interference Ratio for two adjacent numerologies: $\Delta f_1 = 15$ kHz, $\Delta f_2 = 60$ kHz. $H = 1/4$ CP.

them different numerologies in different subbands [93]. However, although within a given numerology subcarriers are mutually orthogonal, subcarriers with different numerologies may cause interference to each other, especially if they are close in frequency. This effect, known as inter-numerology interference (INI), may significantly degrade performance [93, 95].

We consider next a scenario in which two adjacent (i.e., no guard band) frequency subbands accommodate different numerologies: band 1 with subcarrier spacing $\Delta f_1 = 15$ kHz, and band 2 with $\Delta f_2 = 30$ kHz. Band 1 transmits 8 RBs whereas band 2 is using 4 RBs, so that the occupied bandwidth is the same for both bands (1.44 MHz). The CP overhead is set to 7% and the window edge size H is 1/4 CP for both numerologies. In the design of the optimum window for band 1, the weighting function was taken as $W(f) = 1$ for frequencies farther than 1.47 MHz from the center frequency, and zero otherwise; whereas for band 2, the corresponding value was taken as 1.32 MHz. Fig. 2.10 shows the corresponding SIR values. Band 1 suffers from more interference from band 2, as the latter has wider subcarriers with sidelobes decreasing more slowly. The proposed design provides significant improvement in SIR over both subbands as compared to RCW-OFDM, for the same window overhead.

Furthermore, if band 2 uses a wider subcarrier spacing, it will cause higher interference to the adjacent band 1. Fig. 2.11 shows the results in such scenario, where band 2 is now using a subcarrier spacing of $\Delta f_2 = 60$ kHz and transmits 2 RBs; whereas the parameters for band 1 were the same as in the previous case. The spectral weighting for band 2 was now taken as

$W(f) = 1$ for frequencies farther than 0.72 MHz from its center frequency and zero otherwise. It can be seen that the SIR for band 1 is significantly lower than in the previous case, highlighting the benefits of an optimized window design.

2.5. Conclusion

Windowing at the transmit side is an effective way to reduce out-of-band radiation, with the benefit of having low implementation complexity and being transparent to the receiver. In this chapter, a novel window design for multicarrier systems has been presented, focusing on the reduction of out-of-band radiation. The proposed design provides the flexibility to minimize the OBR in a given frequency region which is user-selectable, with the possibility of assigning different weights to different subregions. This tradeoff is particularly appealing for mitigating internumerology interference in 5G systems. Since the optimized window is computed offline, the online computational complexity is the same as that for other windowing techniques.

Chapter 3

Distortion-constrained memoryless spectral precoding

This chapter is adapted with permission of the coauthors and the editorial from IEEE: K. Hussain, A. Lojo and R. López-Valcarce, Flexible Spectral Precoding for Sidelobe Suppression in OFDM Systems, in 44th IEEE International Conference on Acoustics, Speech and Signal Processing (ICASSP), 2019, pages 4789-4793, May 2019, Brighton, UK. And with permission of the coauthors and the editorial from EURASIP: K. Hussain and R. López-Valcarce, OFDM Spectral Precoding With Per-Subcarrier Distortion Constraints, in 27th European Signal Processing Conference (EUSIPCO), 2019, pages 1-5, September 2019, A Coruña, Spain.

3.1. Introduction

This chapter focuses on frequency-domain techniques, and two novel spectral precoding designs are presented to reduce the unwanted emission of OFDM. As discussed before, frequency-domain techniques modify the samples before IFFT operation in order to reduce the sidelobes. The frequency-domain methods such as guard band insertion, MCQ, SW and AIC generally have limited performance in terms of sidelobe suppression, in addition to other issues as discussed in Sec. 1.3. On the other hand, spectral precoding achieves significant OBR reduction. Spectral precoding modulates all the subcarriers with some linear combination of data symbols. Many precoder designs have been proposed in the literature under different criteria,

e.g., notch-based precoders [118–122], orthogonal precoding [123, 124, 126], N-continuous [127–134], or other heuristics [135–138]. However, unlike the windowing methods discussed in Chapter 2, precoding is not transparent at the receiver. Since precoding introduces some distortion in the signal, an appropriate decoder is required at the receiver to avoid symbol error rate degradation. Consequently, there is a need to tradeoff OBR reduction, residual error rate, and computational complexity at both the transmitter (precoder) and receiver (decoder). For example, orthogonal precoders provide very high OBR reduction at the expense of high precoding and decoding complexity, and even with the reduced-complexity implementations, it still remains a concern [140]. Moreover, in certain applications, some amount of OBR is acceptable as long as it complies with the corresponding spectral emission mask, so orthogonal precoding need not be the best choice regarding system resources.

Motivated by the above considerations, we present novel spectral precoder designs which are flexible enough to allow the aforementioned complexity/performance tradeoffs. They directly minimize OBR over a given frequency range without specifying notch frequencies. The amount of distortion on data subcarriers, which determines the complexity of the decoder at the receiver, is controlled through a user-selectable parameter. More specifically, the first design constraints the overall normalized mean squared error (NMSE) introduced by the precoder in a data block. However, this *total distortion constrained* (TDC) design may result in some uneven NMSE distribution among subcarriers, and these highly distorted subcarriers are more susceptible to errors which increases the receiver complexity. Thus, to improve the TDC design, we propose a *per-subcarrier distortion constrained* (PSDC) design which sets NMSE constraints on each data subcarrier individually. This way, a user-selectable NMSE profile can be specified, providing more flexibility and control in the tradeoff between OBR reduction and the required number of decoder iterations. Moreover, both designs result in precoding matrices that are approximately low rank, a property that can be exploited to reduce complexity further.

3.2. Signal model

Using the model from Sec. 1.5, the proposed system allocates the K active subcarriers as follows:

- K_d subcarriers are dedicated to sending data. We define $\boldsymbol{S} \in \mathbb{C}^{K \times K_d}$ as the matrix comprising the K_d columns of $\boldsymbol{I}_K$ whose indices correspond to the location of the data subcarriers.

- K_c subcarriers are reserved for OBR reduction. We define $\boldsymbol{T} \in \mathbb{C}^{K \times K_c}$ as the matrix comprising the K_c columns of $\boldsymbol{I}_K$ whose indices correspond to the location of these cancellation subcarriers.

Thus, $K = K_d + K_c$, and the allocation matrices $\boldsymbol{S}$ and $\boldsymbol{T}$ correspond to the locations of data and cancellation subcarriers respectively. Moreover, $\boldsymbol{S}$ and $\boldsymbol{T}$ are semi-unitary and pairwise orthogonal, i.e., $\boldsymbol{S}^H\boldsymbol{S} = \boldsymbol{I}_{K_d}$, $\boldsymbol{T}^H\boldsymbol{T} = \boldsymbol{I}_{K_c}$ and $\boldsymbol{S}^H\boldsymbol{T} = \boldsymbol{0}$. The transmit samples $\boldsymbol{x} \in \mathbb{C}^K$ are generated from the data samples $\boldsymbol{d} \in \mathbb{C}^{K_d}$ as

$$\boldsymbol{x} = \boldsymbol{G}\boldsymbol{d} = (\boldsymbol{S}\boldsymbol{P} + \boldsymbol{T}\boldsymbol{Q})\boldsymbol{d}, \tag{3.1}$$

where $\boldsymbol{P} = \boldsymbol{S}^H\boldsymbol{G}$ (size $K_d \times K_d$) and $\boldsymbol{Q} = \boldsymbol{T}^H\boldsymbol{G}$ (size $K_c \times K_d$). Note that if one sets $\boldsymbol{P} = \boldsymbol{I}_{K_d}$ and $\boldsymbol{Q} = \boldsymbol{0}$, then the data vector $\boldsymbol{d}$ is directly mapped to the corresponding subcarriers, whereas the cancellation subcarriers are assigned zero power. The data subcarriers can be easily extracted from the transmit vector $\boldsymbol{x}$, represented mathematically as the product

$$\boldsymbol{S}^H\boldsymbol{x} = \boldsymbol{S}^H(\boldsymbol{S}\boldsymbol{P} + \boldsymbol{T}\boldsymbol{Q})\boldsymbol{d} = \boldsymbol{P}\boldsymbol{d} \tag{3.2}$$

In general, due to the presence of $\boldsymbol{P}$, the precoding operation introduces distortion in the data subcarriers with the corresponding performance degradation if no countermeasures are adopted at the receiver. From (1.10), the power spectral density of the signal can be rewritten as

$$S_s(f) = \mathrm{tr}\{\boldsymbol{G}^H\boldsymbol{\Phi}(f)\boldsymbol{G}\}, \tag{3.3}$$

where we assume $\mathbb{E}\{\boldsymbol{d}\boldsymbol{d}^H\} = \boldsymbol{I}_{K_d}$, i.e., $\boldsymbol{C} = \boldsymbol{I}$ in (1.8). Thus, the weighted and total transmission powers become

$$\mathcal{P}_W = \mathrm{tr}\{\boldsymbol{G}^H\boldsymbol{A}_W\boldsymbol{G}\} \quad \text{and} \quad \mathcal{P}_T = \mathrm{tr}\{\boldsymbol{G}^H\boldsymbol{A}_T\boldsymbol{G}\}, \tag{3.4}$$

where $\boldsymbol{A}_W$ and $\boldsymbol{A}_T$ are given by (1.13) and (1.15) respectively.

3.3. Total Distortion Constraint (TDC)

The symbols modulating the data subcarriers are given by $\boldsymbol{S}^H\boldsymbol{x} = \boldsymbol{P}\boldsymbol{d} \neq \boldsymbol{d}$, and to facilitate the task of the receiver, this distortion should be kept small. The error vector magnitude (EVM) is one of the popular metric to measure the distortion in communication standards like wireless LAN (WLAN) or LTE [155, 156]. The distortion is the deviation of transmit symbols from the true data symbols, which can defined as the normalized mean squared error (NMSE) by

$$\frac{\mathbf{E}\{\|\boldsymbol{P}\boldsymbol{d} - \boldsymbol{d}\|^2\}}{\mathbf{E}\{\|\boldsymbol{d}\|^2\}} = \frac{1}{K_d}\|\boldsymbol{P} - \boldsymbol{I}_{K_d}\|_F^2, \tag{3.5}$$

where $\|\cdot\|_F$ denotes the Frobenius norm. We propose to minimize OBR subject to a constraint on the NMSE, together with a constraint on the total transmit power. The resulting optimization problem can be written as

$$\min_{\boldsymbol{P},\boldsymbol{Q}} \ \mathrm{tr}\{\boldsymbol{G}^H\boldsymbol{A}_W\boldsymbol{G}\} \quad \text{s.to} \begin{cases} \|\boldsymbol{P}-\boldsymbol{I}_{K_d}\|_F^2 \le K_d\epsilon \\ \mathrm{tr}\{\boldsymbol{G}^H\boldsymbol{A}_T\boldsymbol{G}\} \le \beta P_{\mathrm{ref}} \\ \boldsymbol{S}\boldsymbol{P}+\boldsymbol{T}\boldsymbol{Q}=\boldsymbol{G} \end{cases} \tag{3.6}$$

where $\epsilon \ge 0$ is a design constant, representing the maximum allowable value of the NMSE, and $P_{\mathrm{ref}} = \mathrm{tr}\{\boldsymbol{S}^H\boldsymbol{A}_T\boldsymbol{S}\}$ is the transmit power for $(\boldsymbol{P},\boldsymbol{Q}) = (\boldsymbol{I}_{K_d},\boldsymbol{0})$, i.e., when using null subcarriers and no precoding. The scaling factor $\beta > 0$ is used to prevent undesirable spectral spurs. Generally larger values of β provide more OBR reduction since there is more available power for cancellation subcarriers. However, it may yield a PSD with large peak values in the frequencies corresponding to the cancellation subcarriers. This spectral overshoot is undesirable in practice, because spectral emission masks place upper bounds on the PSD relative to its maximum value. Thus, there is a tradeoff between OBR reduction and spectral peaks by choosing β.

Problem (3.6) is a Least Squares (LS) problem with two Quadratic Inequality constraints, or LS2QI. It is a convex problem, and in principle it can be solved using available convex solvers. However, as the number of system subcarriers increases, this approach becomes impractical due to the large number of variables involved. This issue is of particular importance in dynamic spectrum access systems which reconfigure their transmissions as spectrum availability conditions evolve.

For that reason, we propose an alternative approach based on the fact that LS problems with a single Quadratic Inequality constraint (LSQI) can be solved efficiently by making use of the Generalized Singular Value Decomposition (GSVD) [157, Ch. 12]. The key observations are: (i) if either of the two inequality constraints is neglected in (3.6), an LSQI problem results, and (ii) the first inequality constraint in (3.6) involves $\boldsymbol{P}$ but not $\boldsymbol{Q}$. These facts suggest the following iterative scheme. Starting with some guess $\boldsymbol{P}_1$, for $k \ge 1$ do:

$$\begin{aligned} \boldsymbol{Q}_k &= \arg\min_{\boldsymbol{Q}} \mathcal{P}_W(\boldsymbol{P}_k,\boldsymbol{Q}) \\ &\quad \text{s. to} \quad \mathcal{P}_T(\boldsymbol{P}_k,\boldsymbol{Q}) \le \beta P_{\mathrm{ref}}, \qquad (3.7) \\ \boldsymbol{P}_{k+1} &= \arg\min_{\boldsymbol{P}} \mathcal{P}_W(\boldsymbol{P},\boldsymbol{Q}_k) \\ &\quad \text{s. to} \quad \|\boldsymbol{P}-\boldsymbol{I}_{K_d}\|_F^2 \le K_d\epsilon, \qquad (3.8) \end{aligned}$$

where $\mathcal{P}_W$ and $\mathcal{P}_T$ are given by (3.4). The iteration can be initialized with $\boldsymbol{P}_1 = \boldsymbol{I}_{K_d}$. Note that the above iteration (3.7)-(3.8) produces a sequence

$(\boldsymbol{P}_k, \boldsymbol{Q}_k)$ of feasible points for problem (3.6); since the feasible set is closed, any convergent point must be feasible. We note that no convergence problems have been observed in any simulations we have tried. The solution to the problems (3.7) and (3.8) are shown in Appendix B and Appendix C respectively.

At the receiver, after carrier and timing synchronization, the cyclic prefix is discarded and an N-point FFT is applied. The K_c non-data subcarriers are just discarded. After channel equalization (assuming a perfect channel equalizer), the K_d data subcarriers are available and the resulting $K_d \times 1$ vector of samples $\boldsymbol{r}$ can be written as

$$\boldsymbol{r} = \boldsymbol{P}\boldsymbol{d} + \boldsymbol{w} = \boldsymbol{d} + \boldsymbol{\Delta}\boldsymbol{d} + \boldsymbol{w}, \tag{3.9}$$

where $\boldsymbol{w}$ is the noise vector, and $\boldsymbol{\Delta} \triangleq \boldsymbol{P} - \boldsymbol{I}_{K_d}$ is the distortion coefficient, satisfying $\|\boldsymbol{\Delta}\|_F^2 \leq K_d\epsilon$ by design. Thus, the fact that this distortion coefficient is small suggests the use of iterative decoding as follows, exploiting the finite-alphabet property of practical constellations. We initialize $\hat{\boldsymbol{d}}_0 = \boldsymbol{r}$ and, at iteration k, the estimate of the data vector $\boldsymbol{d}$ is obtained as

$$\hat{\boldsymbol{d}}_k = \mathrm{DEC}\{\boldsymbol{r} - \boldsymbol{\Delta}\hat{\boldsymbol{d}}_{k-1}\}, \quad k = 1, 2, \ldots \tag{3.10}$$

where $\mathrm{DEC}\{\cdot\}$ is an entrywise hard-decision operator, returning for each entry its closest point in the constellation.

3.3.1. Complexity analysis

Computational complexity plays an important role in energy consumption of limited-power battery-operated devices. The complexity of the proposed design for both the transmitter and receiver, in terms of complex multiplications per OFDM symbol, is discussed below.

Transmitter Complexity

Direct implementation of the precoder (3.1) requires $(K_d + K_c)K_d$ operations. However, it has been observed empirically that the matrices $\boldsymbol{\Delta}$ and $\boldsymbol{Q}$ are approximately of low rank. Hence, it is possible to truncate their respective SVDs to their $r_\Delta \ll K_d$ and $r_Q \ll K_d$ principal components (details are given in Appendix D), so that they can be accurately approximated as

$$\boldsymbol{\Delta} \approx \boldsymbol{L}_\Delta \boldsymbol{R}_\Delta^H, \qquad \boldsymbol{Q} \approx \boldsymbol{L}_Q \boldsymbol{R}_Q^H, \tag{3.11}$$

where $\boldsymbol{L}_\Delta$, $\boldsymbol{R}_\Delta$ have size $K_d \times r_\Delta$, whereas $\boldsymbol{L}_Q$ and $\boldsymbol{R}_Q$ have size $K_c \times r_Q$ and $K_d \times r_Q$ respectively. In this way, the transmitter computes $\boldsymbol{P}\boldsymbol{d} \approx$

$\boldsymbol{d} + \boldsymbol{L}_\Delta(\boldsymbol{R}_\Delta^H \boldsymbol{d})$ and $\boldsymbol{Q}\boldsymbol{d} \approx \boldsymbol{L}_Q(\boldsymbol{R}_Q^H \boldsymbol{d})$, requiring $2r_\Delta K_d + r_Q(K_d + K_c)$ operations per OFDM symbol. The complexity reduction with respect to direct implementation can be quite significant.

Receiver Complexity

The computational complexity at the receiver is dominated by the product $\boldsymbol{\Delta}\hat{\boldsymbol{d}}_{k-1}$ in the decoding operation (3.10). Thus, with direct implementation of such product the total number of operations is $K_d^2 N_{\text{it}}$, where N_{it} is the total number of decoding iterations. Using the low-rank approximation $\boldsymbol{\Delta} \approx \boldsymbol{L}_\Delta \boldsymbol{R}_\Delta^H$ instead, this number is reduced to $2r_\Delta K_d N_{\text{it}}$. In practice, N_{it} will depend on the distortion present in the precoded signal: larger values of ϵ will result in improved OBR reduction, but then a larger N_{it} will be likely required. Moreover, the finite-alphabet property of the constellation could be further exploited to save complexity at the receiver. For instance with QPSK the symbols are $\pm 1 \pm j$, and then the product $\boldsymbol{\Delta}\hat{\boldsymbol{d}}$ can actually be computed without products; only real additions and subtractions.

3.3.2. Numerical examples and Discussion

Numerical results are presented next to illustrate the performance of the proposed TDC design. Power spectral density (PSD), spectral peak and symbol error rate (SER) are the performance metrics used for comparison. Online complexity of the system, which can be a bottleneck for some systems, is also considered.

The proposed technique provides the flexibility to control the trade-off between OBR reduction and system complexity. Fig. 3.1 shows the PSD obtained with the proposed design for CP-OFDM system with IFFT of $N = 1024$, 1/8 CP, subcarrier spacing of $\Delta f = 19.5$ kHz and $K = 257$ subcarriers, of which $K_d = 207$ transport 16-QAM data. At the lower and upper spectrum edges, 25 subcarriers are reserved for OBR reduction. An ideal DAC interpolation filter $H_I(f)$ is assumed with a cutoff frequency of 10 MHz. The sampling rate is twice the cutoff i.e., 20 MHz, so that $W(f) = 1$ for $f \in [-10, -2.5] \cup [2.5, 10]$ MHz and $\beta = 1$. Clearly, increasing the value of ϵ improves OBR performance, but as shown in Fig. 3.2 (which considers an AWGN channel), this is at the cost of either SER degradation or increased receiver complexity. With $\epsilon = 0.002$, distortion is small and even without decoding the SER is close to that of an uncoded system; the small gap can be bridged with a single iteration of the proposed decoder. With $\epsilon = 0.02$, OBR is significantly improved (the PSD is reduced by 20

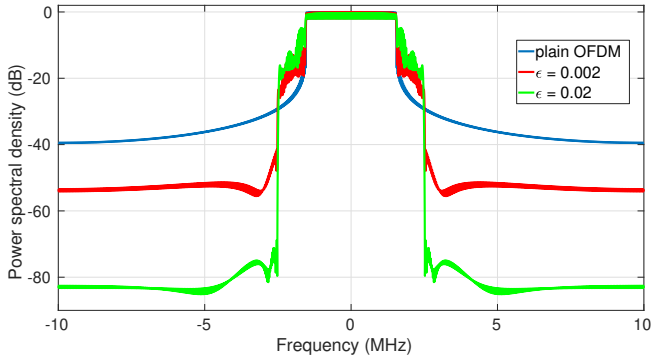

Figure 3.1: PSD for different values of ϵ. $N = 257$, $K_c = 50$, $\beta = 1$.

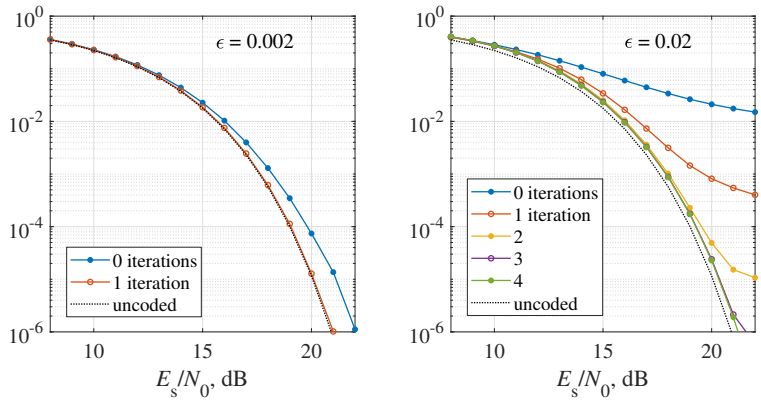

Figure 3.2: SER in AWGN channel of the proposed iterative decoder for different values of ϵ. $K = 257$, $K_c = 50$, $\beta = 1$.

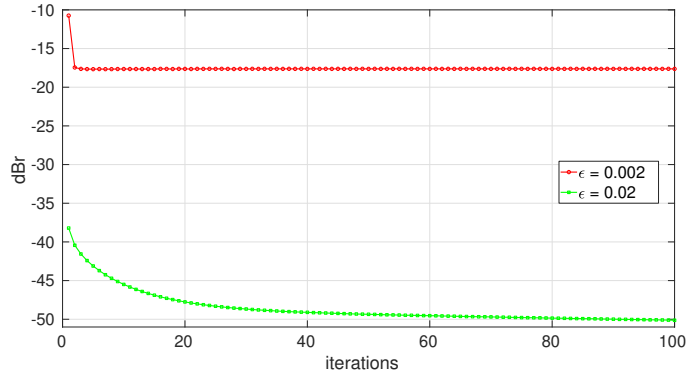

Figure 3.3: Convergence of the proposed TDC design in terms of OBR in the setting of Fig. 3.1

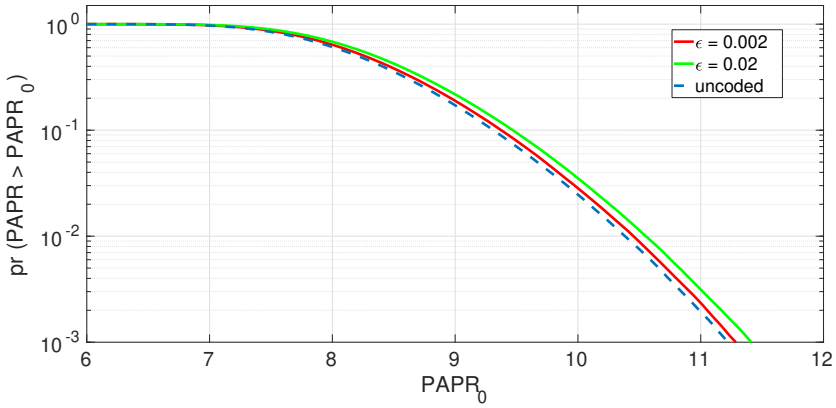

Figure 3.4: PAPR of the proposed TDC design in the setting of Fig. 3.1 with 16 16-QAM modulation.

dB at ±3 MHz from the carrier frequency), but the SER is significantly degraded. Nevertheless, with four decoding iterations the SER is within 0.3 dB of that of the uncoded system. Figure 3.3 demonstrates the convergence of the proposed TDC design in the above given settings. Additionally, the proposed method has minimal impact on the PAPR, with larger values of ϵ leading to only a slight increase in PAPR, as shown in the Figure 3.4 which depicts the PAPR under the same settings using 16-QAM modulation.

The value of β controls the maximum transmit power. With larger values of β, the OBR performance improves; however, this improvement is at the cost of larger undesirable spectral peaks within the passband, because there is more power available for the K_c cancellation subcarriers. Hence, there is a tradeoff between OBR/spectral overshoot. To illustrate this, consider the proposed TDC design in the above settings. Fig. 3.5 shows the PSD of TDC design with different values of β for $\epsilon = 0.002$. It is clear that larger values of β provide more OBR reduction at the expense of larger spectral peaks. The PSD with $\beta = 1$ has no spectral overshoot i.e., 0 dB. On the other hand, the PSD with $\beta = 1.5$ provides more OBR reduction, but it exhibits a spectral overshoot of 6 dB. To get more insight about this tradeoff, Fig. 3.6 shows the relative OBR as a function of the spectral peak for the proposed TDC design. The curve shows OBR and spectral peak for each value of $\beta \in [1, 2]$. When β is close to 1, on the left side of the figure, there is no spectral overshoot but OBR reduction is poor. However, as β increases and the spectral peak becomes larger, the OBR performance improves. Thus a tradeoff between OBR and spectral peak can be achieved by carefully selecting the value of β. Note that such a large value of beta are just for illustration purposes only, as in practice large spectral spurs are not tolerated.

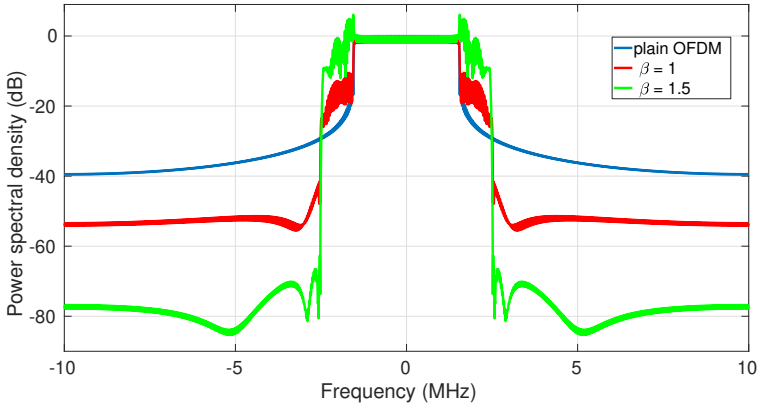

Figure 3.5: PSD for different values of β. $K = 257$, $K_c = 50$, $\epsilon = 0.002$.

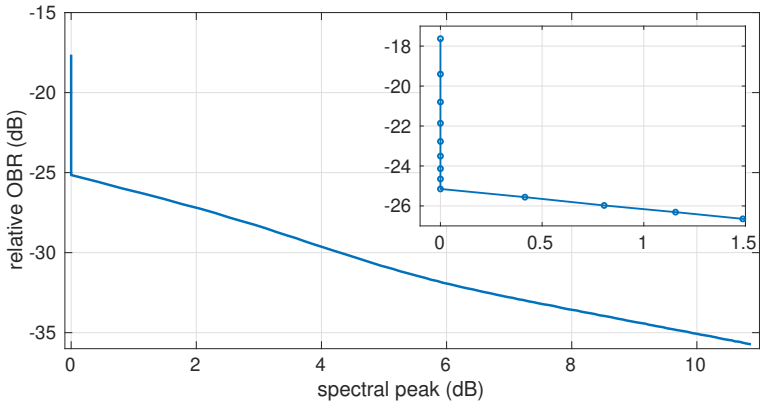

Figure 3.6: OBR achieved with TDC design (relative to that of the unprecoded system) as a function of spectral overshoot. $K = 257$, $K_c = 50$.

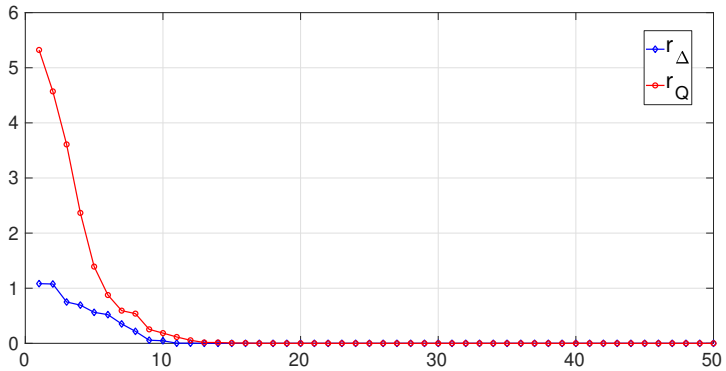

Figure 3.7: Singular values of matrices $\boldsymbol{P}$ and $\boldsymbol{Q}$. $K = 257$, $K_c = 50$, $\epsilon = 0.02$, $\beta = 1$.

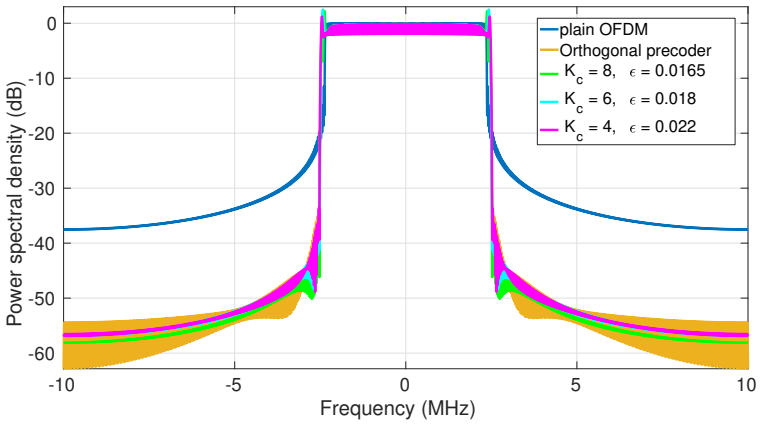

Figure 3.8: PSD of different designs with different ϵ and K_c. $K = 257$.

The computational load at both the transmitter and the receiver is a critical factor. In the above example for $\epsilon = 0.02$, the size of matrices $\boldsymbol{P}$ and $\boldsymbol{Q}$ are (207×207) and (50×207) respectively. Thus, the transmitter needs to compute 53 199 cmults/symb and the receiver requires 171 396 cmults/symb (with 4 iterations). The matrices produced by the TDC design happen to be close to low-rank, which allows us to dramatically reduce the computational load at both the transmitter and the receiver by replacing the matrices $\boldsymbol{P}$ and $\boldsymbol{Q}$ by their best low-rank approximations without compromising OBR performance. Fig. 3.7 shows the singular values of matrices $\boldsymbol{P}$ and $\boldsymbol{Q}$. It can be seen that $\boldsymbol{P}$ and $\boldsymbol{Q}$ are low rank matrices; thus, they can be replaced with ranks $r_\Delta = 10$ and $r_Q = 12$ respectively. Consequently, the transmitter only needs 7224 cmults/symb and the receiver requires 16 560 cmults/symb.

For performance comparison against other techniques, let us consider the above system with $K = 257$ active subcarriers. The proposed design was applied to this setting, with different values of ϵ and K_c, and the value of parameter β is adjusted to prevent spectral peaks above 2 dB. Fig. 3.8 illustrates the resulting PSDs together with that of plain OFDM and the orthogonal precoder design (with a redundancy of $K_c = 7$) from [123]. The orthogonal precoder design has a spectral efficiency of $\frac{257-7}{257} = 97.2\%$. The proposed design is flexible enough to achieve the same level of OBR reduction as of orthogonal precoder with varied levels of efficiency and complexity. For example, as seen in Fig. 3.8, the TDC design with $K_c = 8$ and $\epsilon = 0.0165$ has same performance with an efficiency of 94.1% with just 2 iterations at the decoder (which is shown in Fig. 3.9). The TDC design with $K_c = 6$ and $\epsilon = 0.018$ improves the efficiency to 97.6% at the expense of 3 decoding iterations and small SER loss as illustrated in Fig. 3.10. Nonetheless, the SER is within 0.3 dB of that of the uncoded system. The efficiency can be further improved using $K_c = 4$ and $\epsilon = 0.022$ which achieves similar OBR

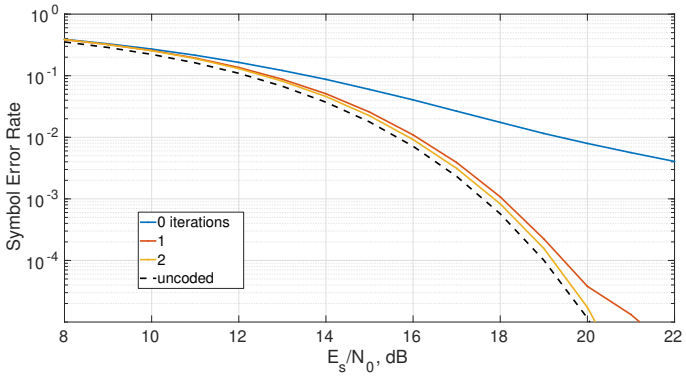

Figure 3.9: SER in AWGN channel for TDC design. $K = 257$, $K_c = 8$, $\epsilon = 0.0165$.

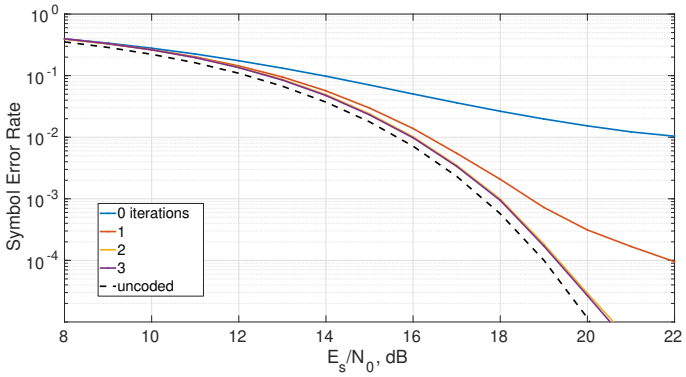

Figure 3.10: SER in AWGN channel for TDC design. $K = 257$, $K_c = 6$, $\epsilon = 0.018$.

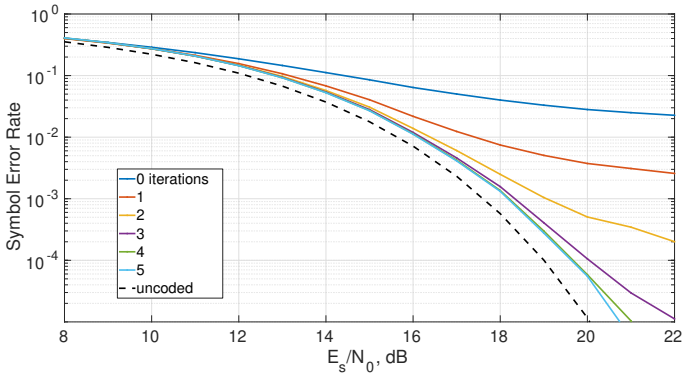

Figure 3.11: SER in AWGN channel for TDC design. $K = 257$, $K_c = 4$, $\epsilon = 0.022$.

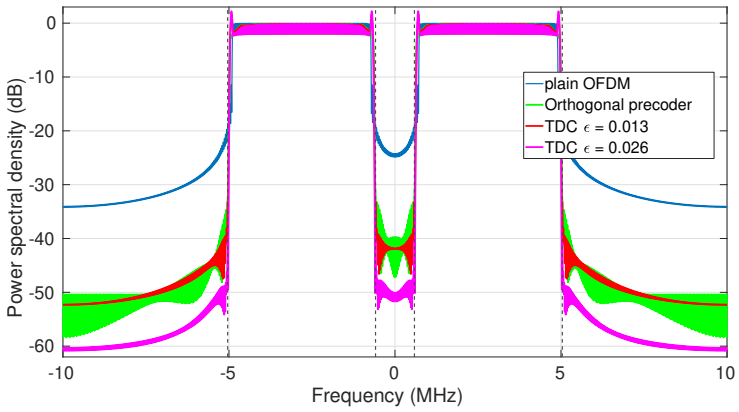

Figure 3.12: PSD of various designs in cognitive radio Scenario 1, $K = 226$.

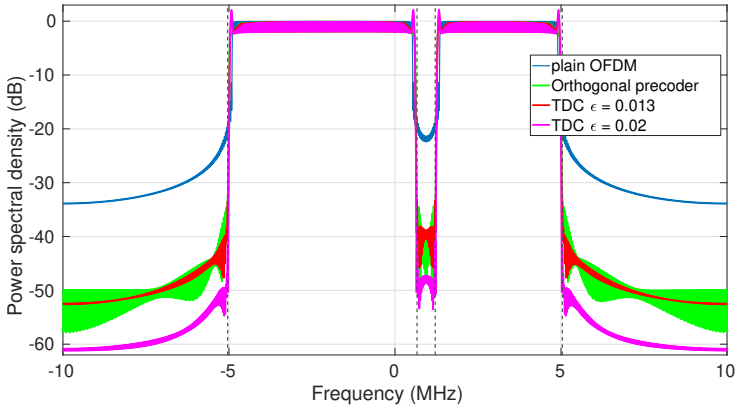

Figure 3.13: PSD of various designs in cognitive radio Scenario 2, $K = 242$.

performance as of orthogonal precoder. However, this improvement is at the cost of additional computational complexity with 5 iterations and small 0.5 dB SER loss as presented in Fig. 3.11.

In the next examples, three different cognitive radio scenarios are considered where the PU subbands need to be protected. The parameters for CP-OFDM system are: IFFT size $N = 512$, 1/8 CP and subcarrier spacing $\Delta f = 39$ kHz. In Scenario 1, the SU has 226 active subcarriers, located symmetrically on both sides of the PU band. Scenario 2 has two spectrum holes with 242 active subcarriers, but they are located asymmetrically around the PU band. Lastly, Scenario 3 has multiple spectrum holes available for the secondary user with 211 active subcarriers. However, multiple PU subbands are within the passband that need to be protected. In all scenarios, $K_c = 12$ cancellation subcarriers are used to aid in OBR reduction, which are equally divided and located on each of the spectrum edges of the SU band. The spectral peak is limited to 2 dB.

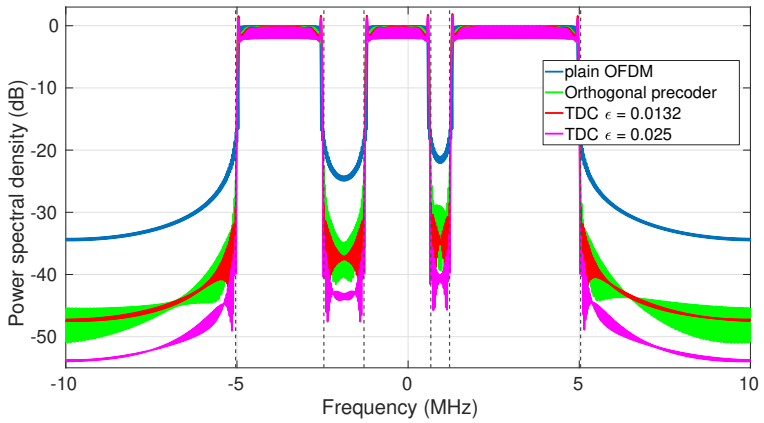

Figure 3.14: PSD of various designs in cognitive radio Scenario 3, $K = 211$.

Fig. 3.12 shows the PSDs of standard OFDM (with 12 null subcarriers), orthogonal precoder design (with $K_c = 12$), and the proposed TDC design in the cognitive radio scenario 1. The TDC design with $\epsilon = 0.013$ provides approximately the same OBR reduction as compared to the orthogonal precoder. With $\epsilon = 0.026$, the OBR reduction can be improved at the expense of extra computational complexity in the form of 2 more iterations at the decoder. The PSDs of three designs in the cognitive radio scenario 2 are shown in Fig. 3.13 with the efficiency of 95%. The proposed TDC design with $\epsilon = 0.013$ achieves the same level of OBR performance as the orthogonal precoder. The OBR performance can be improved using $\epsilon = 0.02$, without sacrificing additional efficiency, at the cost of extra computational complexity (2 more itr.). Lastly, the cognitive radio scenario 3 is shown in Fig. 3.14. The TDC design with $\epsilon = 0.0132$ and orthogonal precoder with $K_c = 12$ provide the same level of protection to the PU subbands. TDC design with $\epsilon = 0.025$ can provide better protection to the PU subbands by improving the OBR reduction with the same efficiency, but at the expense of extra computational complexity (3 more itr.) at the decoder.

Finally, the performance of the proposed TDC design will be evaluated under practical parameters. Fig. 3.15 shows the performance of TDC design in multi-path channel (using the same setting as Fig. 3.5) for two different ϵ values. A N_{cp} tap channel (equal to CP length) is considered. The taps have exponential power delay profiles generated as $P_{taps} = exp^{-\alpha V}$ where $V = [0\ 1\ \cdots N_{cp}-1]$, and with two decaying constants $\alpha = 0.05$ and $\alpha = 0.2$. The channel taps are random, zero-mean complex Gaussian, and uncorrelated. Moreover, independent channel realizations are assumed for different OFDM symbols. The design with $\epsilon = 0.002$ has same SER performance as that of uncoded system, whereas the TDC design with $\epsilon = 0.02$ needs 2 decoding iterations.

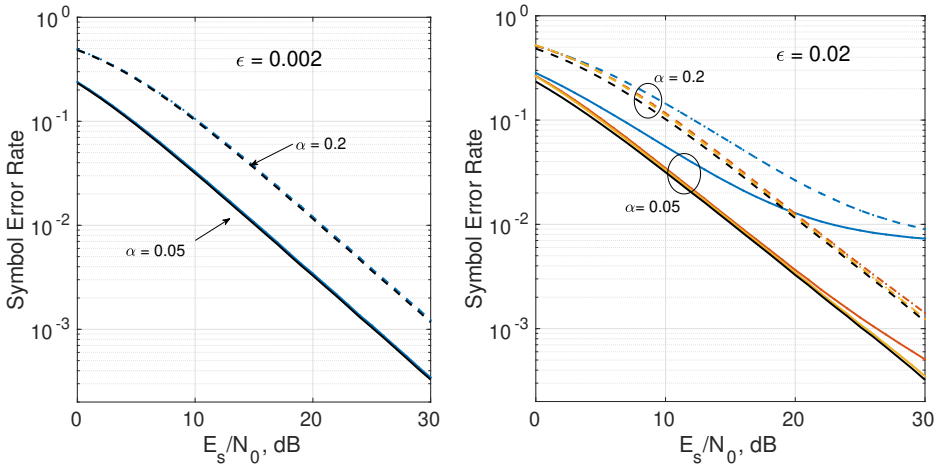

Figure 3.15: SER in multipath channel of the proposed iterative decoder for different values of ϵ. $K = 257$, $K_c = 50$.

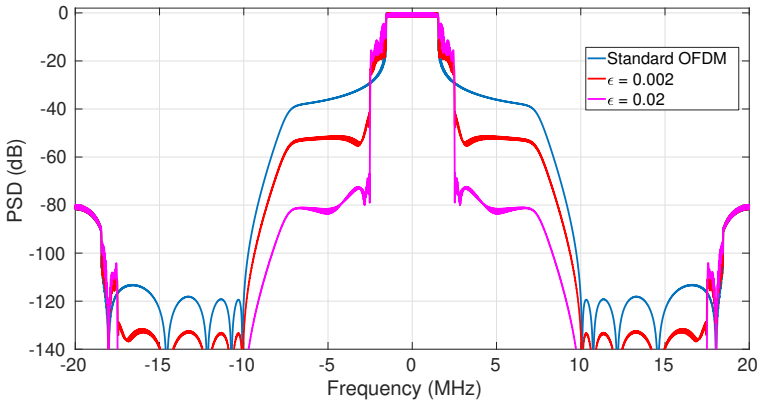

Figure 3.16: PSD of the proposed TDC design with an LPF for different values of ϵ. $K = 257$, $K_c = 50$.

Fig. 3.16 shows the PSD of the proposed TDC design with a more realistic anti-imaging Low-pass filter (LPF) $H_{\mathrm{I}}(f)$ instead of an ideal filter as in Fig. 3.5. A Chebyshev type II filter is considered for anti-imaging LPF because of its performance in OFDM systems over the other types of filters [143]. A 10th order filter is used with a cutoff frequency of $f_c = 10$ MHz and -80 dB stop band attenuation. The frequency response of the Chebyshev type II filter is shown in Fig. 3.17, which has no ripple in the passband. The impulse response of the filter is significantly shorter than the CP ($N_{CP} = N/8 = 128$ samples) as seen in Fig. 3.18. Fig. 3.16 illustrates the PSD of TDC design with the Low-pass filter for different ϵ values. With TDC design, the OFDM sidlelobes decay sharply. The OBR reduction can be improved further with larger values of ϵ.

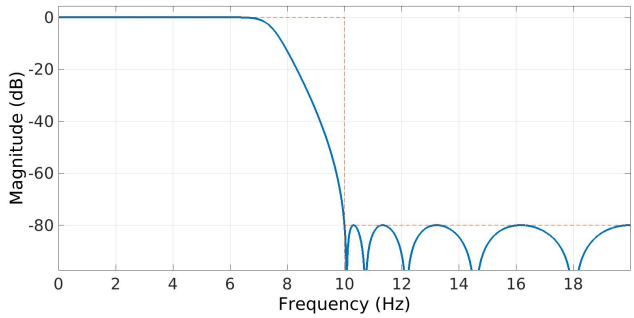

Figure 3.17: Frequency response of the 10th order Chebyshev type II filter with a cutoff frequency of $f_c = 10$ MHz and -80 dB stop band ripples.

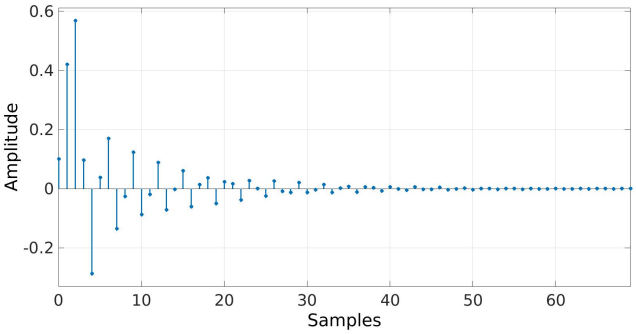

Figure 3.18: Impulse response of the Chebyshev type II filter.

3.4. Per-subcarrier distortion constraint (PSDC)

The TDC design proposed in Sec. 3.3 provides a tradeoff between OBR reduction and decoder complexity by constraining the overall normalized mean squared error. However, we have observed that this total distortion constraint design results in an uneven NMSE distribution among subcarriers, as shown in Fig. 3.19. The NMSE of Fig. 3.1 is shown, where the average NMSE was constrained to 0.02. The edge subcarriers get more distorted than central ones, as they contribute more towards OBR. The highly distorted edge subcarriers are more prone to errors and dominate receiver complexity: the decoder needs more iterations to achieve a given error rate.

Thus, we explore the possibility of setting different NMSE constraints on different data subcarriers in order to provide more flexibility and control in the tradeoff between OBR reduction and the required number of decoder iterations. Letting $\boldsymbol{e}_i$ be the i-th column of $\boldsymbol{I}_{K_d}$, then the NMSE experienced

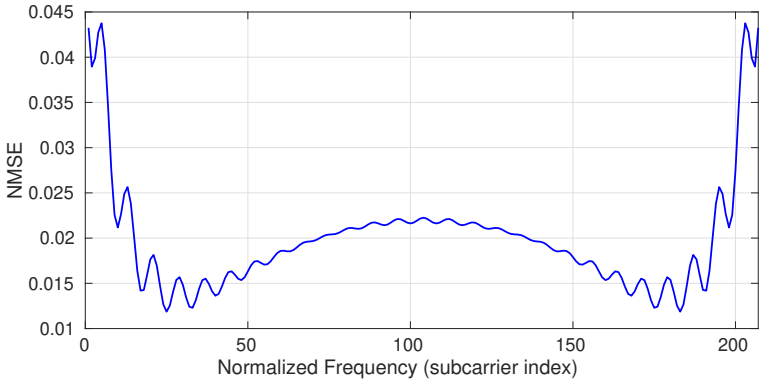

Figure 3.19: Normalized MSE for the TDC design. $\epsilon_{\text{TDC}} = 0.02$.

by the i-th subcarrier is given by

$$\frac{\mathbf{E}\{|\boldsymbol{e}_i^H(\boldsymbol{P}\boldsymbol{d}-\boldsymbol{d})|^2\}}{\mathbf{E}\{|\boldsymbol{e}_i^H\boldsymbol{d}|^2\}} = \|\boldsymbol{P}^H\boldsymbol{e}_i - \boldsymbol{e}_i\|^2, \tag{3.12}$$

i.e., the squared Euclidean distance from $\boldsymbol{e}_i$ to the i-th *row* of $\boldsymbol{P}$, and it is assumed that $\mathbf{E}\{\boldsymbol{d}\boldsymbol{d}^H\} = \boldsymbol{I}$. In the proposed PSDC design, the NMSE (3.12) on each subcarrier is constrained to a maximum value $0 \leq \epsilon_i \ll 1$. Similarly to TDC, the transmit power is constrained. The design becomes

$$\min_{\boldsymbol{P},\boldsymbol{Q}} \text{tr}\{\boldsymbol{G}^H\boldsymbol{A}_W\boldsymbol{G}\} \quad \text{s.to} \begin{cases} \|\boldsymbol{P}^H\boldsymbol{e}_i - \boldsymbol{e}_i\|^2 & \leq & \epsilon_i, \\ i = 1, \cdots, K_d, & & \\ \text{tr}\{\boldsymbol{G}^H\boldsymbol{A}_T\boldsymbol{G}\} & \leq & \beta P_{\text{ref}}, \\ \boldsymbol{S}\boldsymbol{P} + \boldsymbol{T}\boldsymbol{Q} & = & \boldsymbol{G}, \end{cases} \tag{3.13}$$

where β controls the undesirable spectral spurs. Problem (3.13) is a Least Squares (LS) problem with $K_d + 1$ Quadratic Inequality (QI) constraints, and hence convex. Although it can be solved in principle using any suitable convex optimization package, this becomes impractical as the number of subcarriers increases. Thus, we seek alternative approaches with less complexity. Note that LS problems with a *single* QI constraint (LSQI) can be efficiently solved via the Generalized Singular Value Decomposition (GSVD) [157, Ch. 12]. Our approach is to replace Problem (3.13) by a sequence of much simpler LSQI problems.

To this end, note first that for fixed $\boldsymbol{P}$, (3.13) reduces to an LSQI problem with respect to $\boldsymbol{Q}$, similarly to TDC design in Sec. 3.3 . On the other hand, let $\widetilde{\boldsymbol{p}}_i \triangleq \boldsymbol{P}^H\boldsymbol{e}_i$, and given $\ell \in \{1, \cdots, K_d\}$, consider Problem (3.13) for fixed $\boldsymbol{Q}$ and $\widetilde{\boldsymbol{p}}_i$ for all $i \neq \ell$, i.e., the minimization is carried out with respect to $\widetilde{\boldsymbol{p}}_\ell$ only: in this way, an LSQI problem is obtained, whose only constraint is $\|\widetilde{\boldsymbol{p}}_\ell - \boldsymbol{e}_\ell\|^2 \leq \epsilon_\ell$. In fact, the resulting LSQI problem is highly structured

Algorithm 1 Precoder design with per-subcarrier distortion constraints (PSDC)

Initialize $k = 1$ and $\boldsymbol{P}_1 = \boldsymbol{I}_{K_d}$
repeat
  $\boldsymbol{Q}_k \leftarrow \arg\min_{\boldsymbol{Q}} \mathcal{P}_W(\boldsymbol{P}_k, \boldsymbol{Q})$ subject to $\mathcal{P}_T(\boldsymbol{P}_k, \boldsymbol{Q}) \leq \beta P_{\text{ref}}$
  $\forall\, i \in \{1, \ldots, K_d\},\ \widetilde{\boldsymbol{p}}_{k,i} \leftarrow \boldsymbol{P}_k^H \boldsymbol{e}_i$
  for $\ell = 1, \ldots, K_d$ **do**
    $\boldsymbol{P}_{k+1}^{(\ell)} \leftarrow \sum_{j=1}^{\ell-1} \boldsymbol{e}_j \widetilde{\boldsymbol{p}}_{k+1,j}^H + \boldsymbol{e}_\ell \widetilde{\boldsymbol{p}}_\ell^H + \sum_{j=\ell+1}^{K_d} \boldsymbol{e}_j \widetilde{\boldsymbol{p}}_{k,j}^H$
    $\widetilde{\boldsymbol{p}}_{k+1,\ell} \leftarrow \arg\min_{\widetilde{\boldsymbol{p}}_\ell} \mathcal{P}_W(\boldsymbol{P}_{k+1}^{(\ell)}, \boldsymbol{Q}_k)$ subject to $\|\widetilde{\boldsymbol{p}}_\ell - \boldsymbol{e}_\ell\|^2 \leq \epsilon_\ell$
  end for
  $\boldsymbol{P}_{k+1} \leftarrow \boldsymbol{P}_{k+1}^{(K_d)}$
  $k \leftarrow k + 1$
until convergence

and can be solved in closed form without resorting to the GSVD (details are shown in Appendix E).

Based on these facts, we propose to minimize $\mathcal{P}_W$ sequentially and iteratively, first with respect to $\boldsymbol{Q}$ and then with respect to the rows of $\boldsymbol{P}$; at each step, the corresponding optimization variable is affected by a single QI constraint. The proposed iterative method is summarized in Algorithm 1.

In this way, the original problem is replaced by a sequence of easy-to-solve LSQI problems which clearly produces a sequence $(\boldsymbol{P}_k, \boldsymbol{Q}_k)$ of feasible points for problem (3.13). The convergent point must be feasible as the feasible set is closed. We note that no convergence problems have been observed in any simulations we have tried.

At the receiver, after timing and carrier synchronization, the CP is discarded and an N-point FFT is applied. At its output, the samples at the K_c cancellation subcarriers are discarded. After channel equalization (assuming a perfect channel equalization), the K_d data subcarriers are available and the resulting vector $\boldsymbol{r}$ can be written as

$$\boldsymbol{r} = \boldsymbol{P}\boldsymbol{d} + \boldsymbol{w} = \boldsymbol{d} + \boldsymbol{\Delta}\boldsymbol{d} + \boldsymbol{w}, \tag{3.14}$$

where $\boldsymbol{w}$ is the noise vector, and $\boldsymbol{\Delta} \triangleq \boldsymbol{P} - \boldsymbol{I}_{K_d}$ is the distortion matrix, which by design satisfies $\|\boldsymbol{\Delta}\|_F^2 \leq \sum_{i=1}^{K_d} \epsilon_i$. Similar to TDC in Sec. 3.3, the fact that $\boldsymbol{\Delta}$ is small suggests the use of iterative decoding: initializing $\hat{\boldsymbol{d}}_0 = \boldsymbol{r}$, the estimate of the data vector $\boldsymbol{d}$ is obtained at iteration k as

$$\hat{\boldsymbol{d}}_k = \text{DEC}\{\boldsymbol{r} - \boldsymbol{\Delta}\hat{\boldsymbol{d}}_{k-1}\}, \quad k = 1, 2, \ldots \tag{3.15}$$

where $\text{DEC}\{\cdot\}$ is an entrywise hard-decision operator, returning for each entry its closest point in the constellation.

3.4.1. Complexity analysis

It is important to quantify the implementation complexity of any OBR reduction method, both at the transmitter and the receiver. The online complexity of PSDC is the same as TDC. As it turns out, the matrices $\boldsymbol{\Delta}$ and $\boldsymbol{Q}$ obtained with the PSDC design are approximately low-rank, as was the case for TDC. Thus, the SVDs of low rank matrices $\boldsymbol{\Delta}$ and $\boldsymbol{Q}$ can be truncated to their $r_\Delta \ll K_d$ and $r_Q \ll K_d$ principal components, and the transmitter requires $2r_\Delta K_d + r_Q(K_d + K_c)$ cmults/symb.

On the receiver end, complexity is dominated by the product $\boldsymbol{\Delta}\hat{\boldsymbol{d}}_{k-1}$ in (3.15). Using low rank approximation, it is reduced to $2r_\Delta K_d N_{\text{it}}$ cmults/symb. N_{it} will depend on the distortion present in the precoded signal, resulting in a tradeoff between OBR reduction and decoding complexity as in the TDC design. However, the fact that the PSDC design allows to fine-tune the distortion level on a per-subcarrier basis results in a more favorable tradeoff, as shown next.

3.4.2. Numerical examples

We compare the proposed PSDC design with previous schemes, in terms of OBR reduction, symbol error rate (SER), and implementation complexity. In the following numerical examples we consider a CP-OFDM system carrying 16-QAM data with $K = 257$ active subcarriers occupying 5 MHz bandwidth. The IFFT size is $N = 1024$ with a subcarrier spacing of $\Delta f = 19.5$ kHz and 1/8 CP. An ideal DAC filter $H_I(f)$ is considered with a cutoff frequency of 10 MHz. Thus with a sampling rate of 20 MHz, the spectral weighting function is $W(f) = 1$ for $f \in [-10, -2.5] \cup [2.5, 10]$ MHz.

In the first example, the PSDC and TDC designs are compared for $K_d = 237$, so that 10 cancellation subcarriers are reserved at each spectrum edge. The average NMSE in the TDC design was set to $\epsilon_{\text{TDC}} = 0.015$, whereas for PSDC the NMSE at each data subcarrier was set to $\epsilon_i = 0.013$, and β is set to 1 for both cases. These values yield similar results in terms of OBR, without any spectral overshoot as seen in Fig. 3.20. Fig. 3.21 shows the SER of both designs in an AWGN channel. The proposed PSDC design requires fewer decoder iterations (about 2) to cover the gap to the uncoded system, whereas the TDC design needs 5 iterations to do so. For both TDC and PSDC, the resulting matrices $\boldsymbol{\Delta}$ (size 237×237) and $\boldsymbol{Q}$ (size 20×237) were replaced by their best low-rank approximations with $(r_\Delta, r_Q) = (11, 11)$, without compromising performance. With this, both precoders required 8041 cmults/symb. The decoder complexities for TDC ($N_{\text{it}} =$

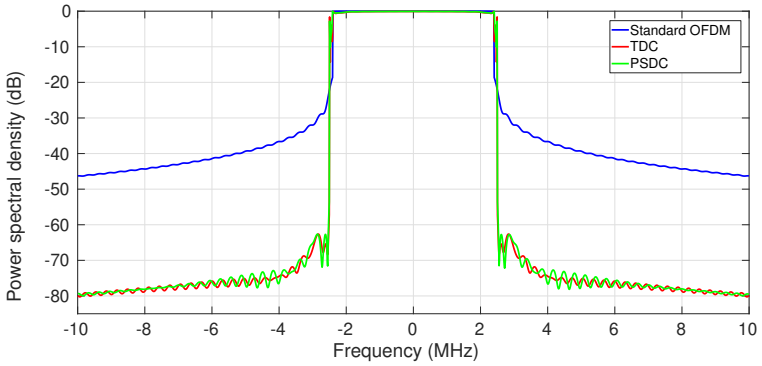

Figure 3.20: Obtained PSDs for a system with $K = 257$, $K_c = 20$. "Standard OFDM" refers to a system with $(\boldsymbol{P}, \boldsymbol{Q}) = (\boldsymbol{I}_{K_d}, \boldsymbol{0})$.

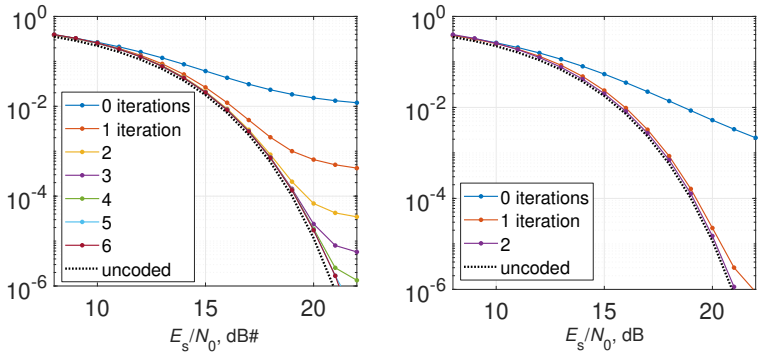

Figure 3.21: SER in AWGN channel, $K = 257$, $K_c = 20$. TDC design (left), PSDC design (right).

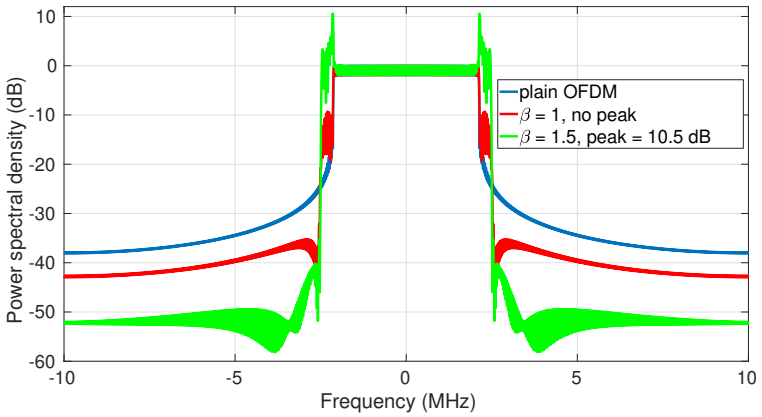

Figure 3.22: Obtained PSDs for a system with different values of β. $K = 257$, $K_c = 20$. $\epsilon_i = 0.0005$.

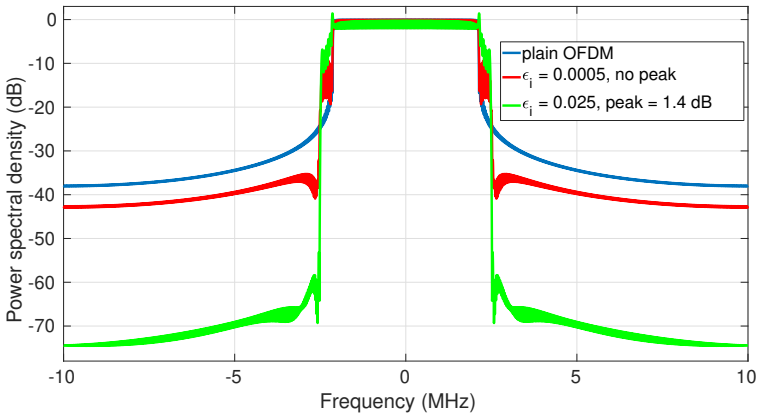

Figure 3.23: Obtained PSDs for a system with different values of ϵ. $K = 257$, $K_c = 20$, $\beta = 1$.

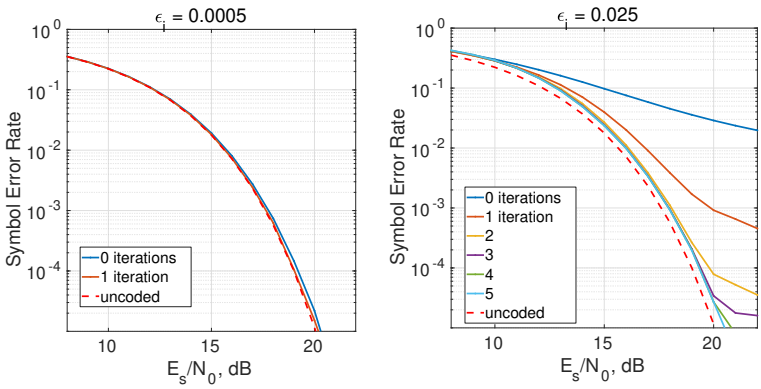

Figure 3.24: SER in AWGN channel of the proposed iterative decoder with PSDC design. $K = 257$, $K_c = 20$, $\beta = 1$.

5) and PSDC ($N_{\text{it}} = 2$) are 26 070 and 10 428 cmults/symb, respectively. Receiver complexity is thus reduced by 60%.

The PSDC design is flexible enough to meet different system requirements. In the second example, the number of cancellation subcarriers is $K_c = 20$ out of $K = 257$. Fig. 3.22 shows the PSDs obtained by the proposed PSDC method (with $\epsilon_i = 0.0005$ for all i) for different values of β. Similar to the TDC design, increasing the value of β leads to higher OBR performance; however, it also causes larger undesirable spectral peaks in the passband. Furthermore, the value of ϵ on each subcarrier determines the OBR reduction. It is clear from Fig. 3.23 that larger values of ϵ achieve better sidelobe suppression. However, this reduction comes at the cost of increased complexity at the decoder in terms of more decoding iterations in order to avoid SER degradation as illustrated in Fig. 3.24. Therefore, a

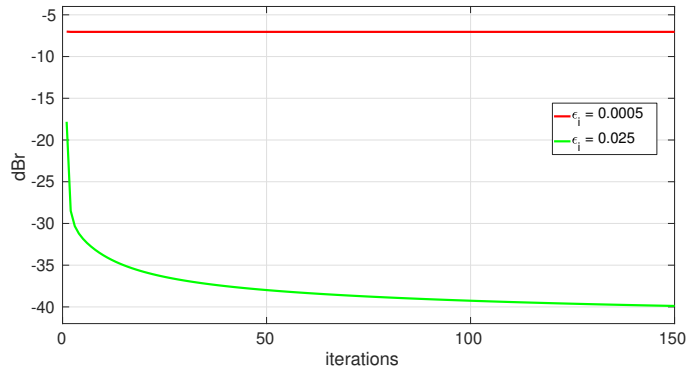

Figure 3.25: Convergence of the proposed PSDC method in terms of OBR in the settings of Fig. 3.23.

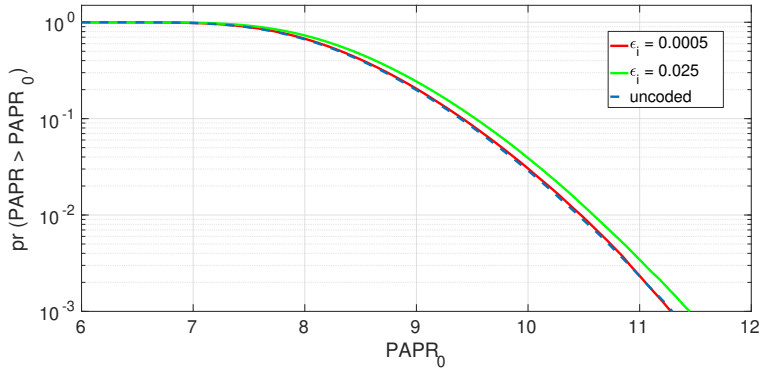

Figure 3.26: PAPR of the PSDC design for the settings in Fig. 3.23 with 16-QAM modulation.

tradeoff must be found between OBR/peak and OBR/complexity. The convergence of the PSDC design is demonstrated in Fig. 3.25. Furthermore,, the proposed design has minimal impact on the PAPR. As depicted in the Fig. 3.26, larger values of ϵ may lead to a slight increase in the PAPR.

Cognitive radio scenarios are considered in the next examples with the following parameters: IFFT size $N = 512$, 1/8 CP, subcarrier spacing $\Delta f =$ 39 kHz, and an ideal DAC filter with a cutoff frequency of 10 MHz. Scenario 1 has 226 active subcarriers, located symmetrically on both sides of the PU band. In Scenario 2, SU can transmit on 242 active subcarriers which are located asymmetrically around the PU band. Lastly, Scenario 3 has multiple spectrum holes available for transmission containing 211 active subcarriers. However, there are multiple PU subbands within the passband that need to be protected. The cancellation subcarriers are fixed to be $K_c = 12$, which are equally divided and located on each of the spectrum edges of the SU band. The spectral peak is limited to 2 dB.

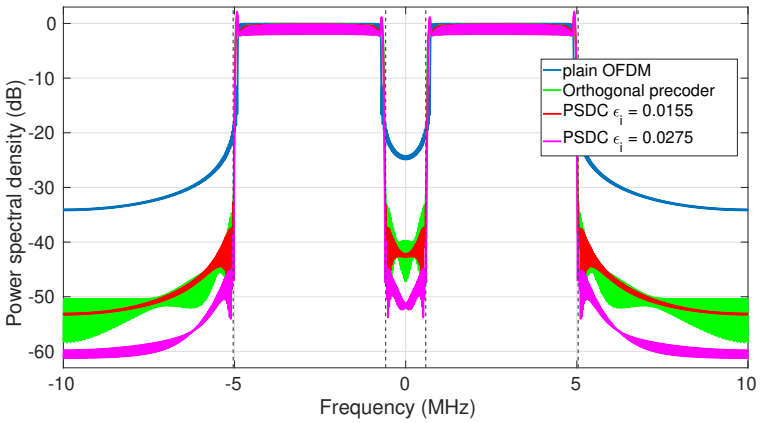

Figure 3.27: Obtained PSDs in cognitive radio Scenario 1.

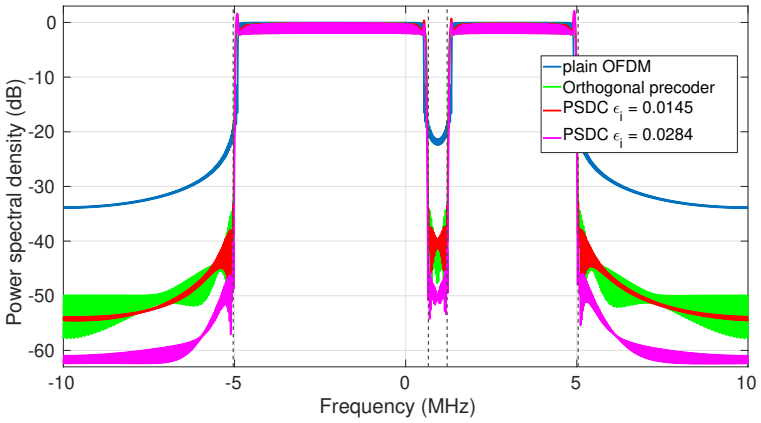

Figure 3.28: Obtained PSDs in cognitive radio Scenario 2.

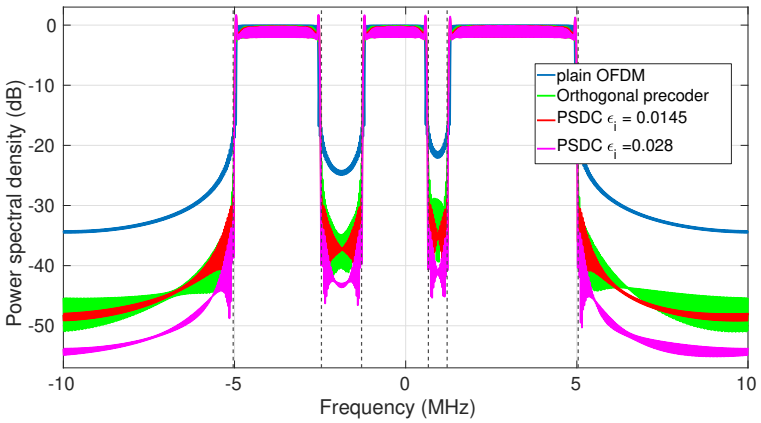

Figure 3.29: Obtained PSDs in cognitive radio Scenario 3.

	Orthogonal (direct)	Orthogonal (Clarkson [140])	PSDC
Scenario 1			
Transmitter	48 364	5280	9132
Receiver	48 364	5280	32 100 (5 it.)
Scenario 2			
Transmitter	62 920	6024	9804
Receiver	62 920	6024	34 500 (5 it.)
Scenario 3			
Transmitter	41 989	4920	8502
Receiver	41 989	4920	29 850 (5 it.)

Table 3.1: Computational complexity of different designs (no. of complex multiplications per OFDM symbol) for the same spectral efficiency for different scenarios.

The PSDs of the proposed PSDC design and orthogonal precoder from [123], along with standard OFDM are shown in Fig. 3.27 for Scenario 1. For the efficiency of 94.6%, PSDC design with $\epsilon_i = 0.0155$ and orthogonal precoder achieve the same level of OBR reduction. The PSDC design requires 2 iterations at the decoder. The OBR performance can be improved with PSDC design using $\epsilon_i = 0.0275$ with the same efficiency, at the cost of complexity (4 itr.) at the decoder. Fig. 3.28 illustrates the PSDs of the three designs in cognitive radio Scenario 2. The orthogonal precoder and PSDC design with $\epsilon_i = 0.0145$ achieve similar OBR performance for the efficiency of 95%. The PSDC design with $\epsilon_i = 0.0284$ can provide more OBR reduction without sacrificing additional efficiency. However, this is at the cost of increased complexity with 5 iterations (previous 2 itr.) at the decoder. The cognitive radio Scenario 3 is shown in Fig. 3.29. Orthogonal precoder and PSDC design with $\epsilon_i = 0.0145$ provide approximately the same level of protection to the PU subbands. With the same spectral efficiency, the PSDC design is able to provide more protection to the PU subbands using $\epsilon_i = 0.028$, at the expense of complexity at the decoder which now requires 5 iterations (instead of 2 itr. for $\epsilon_i = 0.0145$). Thus, the proposed PSDC design can provide better performance without compromising on efficiency at the expense of complexity, which is illustrated is Table 3.1.

In the next example, we consider a bandwidth-limited scenario with only $K_c = 4$ cancellation subcarriers available. In this case, the orthogonal precoder requires 2040 cmults/symb at both transmitter and receiver. The OBR reduction obtained by orthogonal precoding can be improved if one

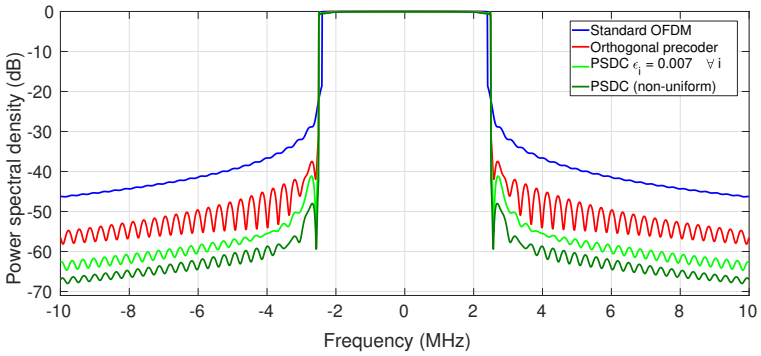

Figure 3.30: Obtained PSDs for a system with $K = 257$, $K_c = 4$.

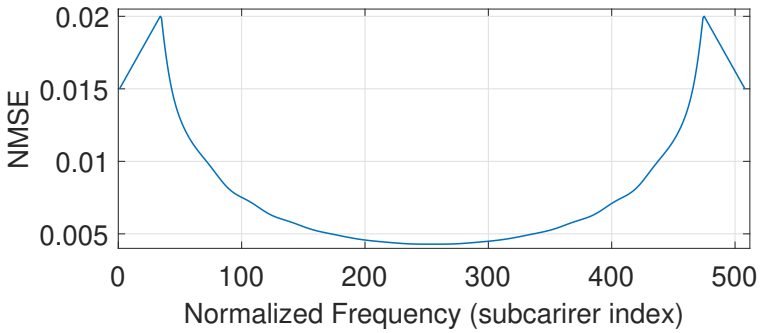

Figure 3.31: Distortion profile $\{\epsilon_i\}$ of the proposed PSDC design.

uses PSDC precoding instead, at the cost of additional complexity. Fig. 3.30 shows an example with $\epsilon_i = 0.007\ \forall i$ with $\beta = 1$. In this case, the decoder requires a single iteration, see Fig. 3.32(a). Using $(r_\Delta, r_Q) = (7, 4)$, the complexity incurred is 4570 and 3542 cmults/symb at the transmitter and receiver, respectively.

Moreover, with the PSDC design it becomes possible to further improve the performance by judiciously specifying a non-uniform NMSE profile $\{\epsilon_i\}$. In particular, consider the profile shown in Fig. 3.31, which allows more distortion at the edge subcarriers than the central subcarriers. Since the edge subcarriers contribute more towards the OBR, more distortion is allowed in those locations, but in contrast with the TDC design, this is done in a controlled manner as we can specified the maximum distortion level on a per-subcarrier basis. The NMSE profile gradually increases the allowed distortion from central subcarriers towards both edges. Thus, using this profile with $\beta = 1$ (which avoids spectral peaks), the OBR is further reduced by more than 6 dB as seen in Fig. 3.30, with the same values $(r_\Delta, r_Q) = (7, 4)$, and one additional decoder iteration, see Fig. 3.32(b).

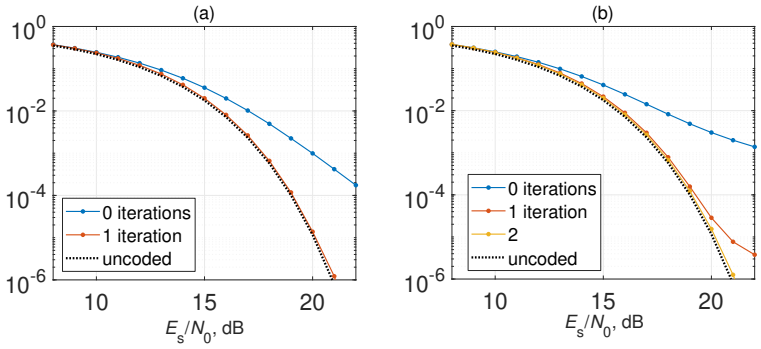

Figure 3.32: SER in AWGN channel of the proposed iterative decoder with PSDC design. (a) $\epsilon_i = 0.007\ \forall i$, (b) ϵ_i as in Fig. 3.31.

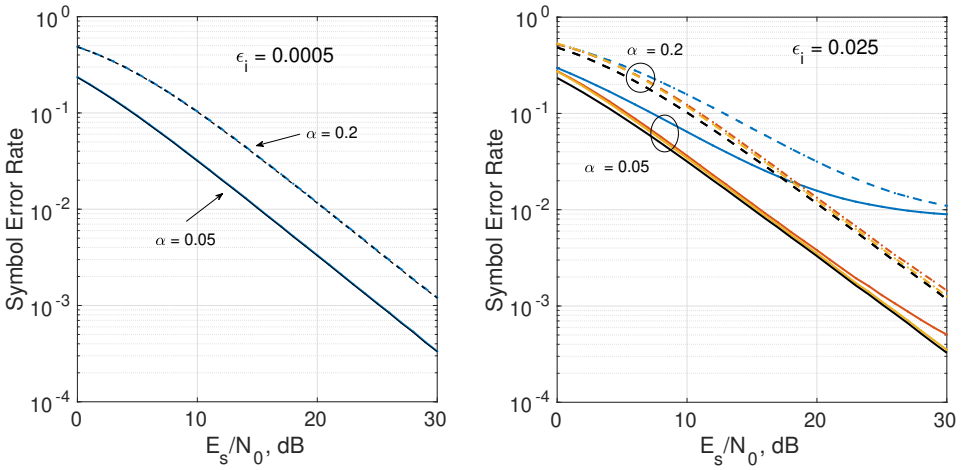

Figure 3.33: SER in multipath channel of the proposed iterative decoder with PSDC design. $K = 257$, $K_c = 20$, $\beta = 1$.

In the end, the performance of the PSDC design is evaluated under practical channel and filter (using the same settings as in Fig. 3.23). Fig. 3.33 shows the SER of the proposed PSDC design in multi-path channel. The channel has N_{cp} taps with exponential decaying power profiles generated via $P_{taps} = exp^{-\alpha[0:N_{cp}-1]^{\iota}}$ with decaying constants $\alpha = 0.05$ and $\alpha = 0.2$. The individual channel taps are random, uncorrelated, and drawn from a zero-mean Gaussian distribution. Additionally, we assume that the channel realizations for each OFDM symbol are independent from one another. Clearly, with larger values of ϵ, more decoding iterations are needed to bridge the gap with that of uncoded system. Fig. 3.34 shows the PSD of the PSDC method at the output of a practical LPF. A 10th order Chebyshev II filter is used (same as in TDC design) with a cutoff frequency $f_c = 10$ MHz and -80 dB stop band attenuation. The frequency and impulse response of the

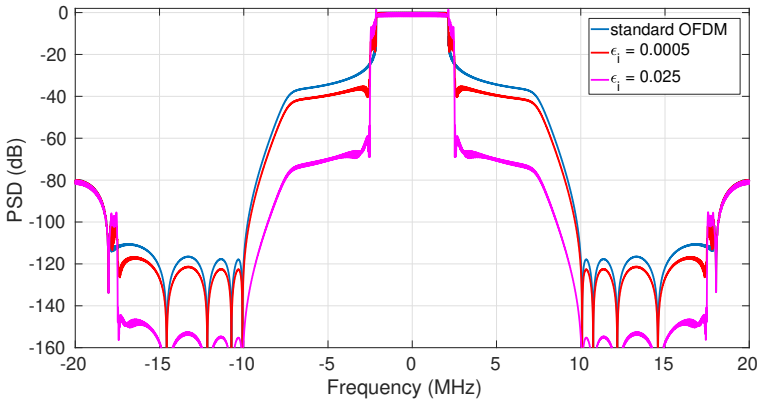

Figure 3.34: PSD of the PSDC design at the output of LPF . $K = 257$, $K_c = 20$.

filter are shown in Fig. 3.17 and Fig. 3.18 respectively. As seen in Fig. 3.34, the PSDC design improves the OBR performance by drastically reducing the OFDM sidelobes.

3.5. Conclusion

In this chapter, we have proposed two novel spectral precoder designs for multicarrier systems aiming to reduce of out-of-band radiation. The designs provide the flexibility to trade off out-of-band radiation reduction and computational complexity. The level of distortion on data subcarriers is given by a user-selectable parameters. The distortion is compensated at the receiver by iterative decoding, with the number of iterations required for a given error rate typically increasing as more distortion is allowed at the transmitter. Moreover, the distortion experienced by data subcarriers can be specified on a per-subcarrier basis, which can reduce the number of iterations required by the decoder, thus significantly reducing the computational complexity of the receiver. In addition, the resulting precoding matrices have very low rank in practice, which allows for significant computational savings in the on-line implementation of both precoder and decoder.

Chapter 4

Joint Window and Precoder Design

This chapter is adapted with permission of the coauthors and the editorial from IEEE: K. Hussain and R. López-Valcarce, Joint Precoder and Window Design for OFDM Sidelobe Suppression, in IEEE Communications Letters, 2022.

4.1. Introduction

This chapter presents a novel design that uses both spectral precoding and windowing simultaneously to minimize radiated power. OFDM has an inherent drawback of large spectrum sidelobes which cause high out-of-band radiation (OBR), and to alleviate this issue, many frequency and time domain methods have been proposed in the literature as discussed in Chapter 1.

All these time- and frequency-domain approaches have their own advantages and drawbacks, and their tradeoffs involving OBR reduction, computational complexity, and throughput efficiency need not be the same. Such tradeoffs should improve by simultaneously acting in both domains; for example, a spectral precoder could be designed for a given window, as in [158]. Our goal is to further improve on such approach by *jointly* optimizing both precoder and window coefficients. Further differences between our design and [158] include: (i) we allow to target arbitrary frequency ranges by leveraging the design from Chapter 2 rather than using notch frequencies; (ii) we allow redundant spectral precoders, establishing the overall through-

put efficiency once this redundancy is taken into account together with the symbol length extension due to windowing. The benefits of the proposed joint design, which is data-independent and can be computed offline, are illustrated for two particular precoding techniques which do not affect the bit error rate, namely orthogonal precoding (OP) and active interference cancellation (AIC).

4.2. System Model

Following the model from Sec. 1.5, the power spectral density (PSD) of $s(t)$ with an IFFT of size N and K active subcarriers is given by

$$S_s(f) = \frac{|H_{\mathrm{I}}(f)|^2}{LT_s} \cdot \boldsymbol{\phi}^H(f)\boldsymbol{G}\boldsymbol{G}^H\boldsymbol{\phi}(f) \tag{4.1}$$

where $\boldsymbol{G} \in \mathbb{C}^{K\times K_d}$ is a linear memoryless precoder. The transmit sequence $\boldsymbol{x} \in \mathbb{C}^K$ is generated from the data sequence $\boldsymbol{d} \in \mathbb{C}^{K_d}$ with $K_d \leq K$ as $\boldsymbol{x} = \boldsymbol{G}\boldsymbol{d}$. Thus, $K_c = K - K_d$ is the precoder redundancy. Assuming $\mathbf{E}\{\boldsymbol{d}\boldsymbol{d}^H\} = \boldsymbol{I}$, one has $\mathbb{E}\{\boldsymbol{x}\boldsymbol{x}^H\} = \boldsymbol{G}\boldsymbol{G}^H$, which has been used in (4.1).

Due to the windowing, the pulse $h_{\mathrm{P}}[n]$ extends from $n = 0$ to $n = L + H - 1$ (similar to the case in Chapter 2), so that the first and the last H samples of any consecutive symbols overlap. The central samples of $h_{\mathrm{P}}[n]$ are fixed to 1 to avoid distortion at the receiver: $h_{\mathrm{P}}[n] = 1$ for $H \leq n \leq L - 1$; whereas the edge samples $h_{\mathrm{P}}[n]$ for $n = 0, 1, \ldots, H - 1$ and $n = L, L + 1, \ldots, L + H - 1$ are to be designed. The gradual transition from 0 to 1 results in a sharper PSD. On the other hand, the effective CP length is reduced to $N_{\mathrm{CP}} = L - N - H$ samples due to the H-sample overlap between consecutive symbols; therefore, for a given effective CP length (determined by the maximum expected length of the channel impulse response), windowing results in a throughput efficiency reduction by a factor $\frac{N+N_{\mathrm{CP}}}{N+N_{\mathrm{CP}}+H}$.

Note that $\boldsymbol{\phi}(f)$ in (4.1), which is given by (1.4) -(1.6) , can be rewritten as $\boldsymbol{\phi}(f) = \boldsymbol{M}(f)\boldsymbol{h}$, where $\boldsymbol{M}(f) \in \mathbb{C}^{K\times(L+H)}$ was defined in (2.4) as

$$[\boldsymbol{M}(f)]_{pq} = e^{j2\pi(q-1)(f-k_p\Delta_f)}, \quad \begin{cases} 1 \leq p \leq K, \\ 1 \leq q \leq L + H, \end{cases} \tag{4.2}$$

and $\boldsymbol{h} \in \mathbb{C}^{L+H}$ comprises the (conjugated) pulse samples:

$$\boldsymbol{h} \triangleq [\ h^*[0] \quad h^*[1] \quad \cdots \quad h^*[L + H - 1]\ ]^T. \tag{4.3}$$

Thus, $S_s(f)$ in (4.1) can be rewritten in terms of $\boldsymbol{G}$ and $\boldsymbol{h}$ as

$$S_s(f) = \frac{|H_{\mathrm{I}}(f)|^2}{LT_s}\boldsymbol{h}^H\boldsymbol{M}^H(f)\boldsymbol{G}\boldsymbol{G}^H\boldsymbol{M}(f)\boldsymbol{h}. \tag{4.4}$$

4.3. Joint Design

Let $W(f) \geq 0$ be a weighting function, giving emphasis to those frequencies over which PSD reduction is important. Then, the weighted power, which quantifies OBR, is given by

$$\mathcal{P}_{\mathrm{W}} = \int_{-\infty}^{\infty} W(f) S_s(f) \mathrm{d}f. \tag{4.5}$$

The goal is to minimize $\mathcal{P}_{\mathrm{W}}$ with respect to the pulse $\boldsymbol{h}$ and precoder $\boldsymbol{G}$. This general problem can be stated as

$$\min_{\boldsymbol{h},\boldsymbol{G}} \ \mathcal{P}_{\mathrm{W}}(\boldsymbol{h},\boldsymbol{G}) \ \text{ s. to } \begin{cases} h[n] = 1, \ \ H \leq n \leq L-1, \\ \text{structural constraint on } \boldsymbol{G}. \end{cases} \tag{4.6}$$

The second constraint in (4.6) depends on the particular precoder structure (*e.g.,* OP or AIC) as discussed below.

Problem (4.6) is nonconvex in general. However, if either $\boldsymbol{h}$ or $\boldsymbol{G}$ is fixed, the corresponding subproblems become manageable. Thus, we propose to cyclically minimize $\mathcal{P}_{\mathrm{W}}$ with respect to these parameters (pulse and precoder).

4.3.1. Optimal window for a given precoder

For fixed $\boldsymbol{G}$, the weighted power in (4.5) becomes $\mathcal{P}_{\mathrm{W}} = \boldsymbol{h}^H \boldsymbol{Z}(\boldsymbol{G}) \boldsymbol{h}$, where $\boldsymbol{Z}(\boldsymbol{G}) \in \mathbb{C}^{(L+H)\times(L+H)}$ is given by

$$\boldsymbol{Z}(\boldsymbol{G}) \triangleq \int_{-\infty}^{\infty} W(f) \frac{|H_{\mathrm{I}}(f)|^2}{LT_s} \boldsymbol{M}^H(f) \boldsymbol{G}\boldsymbol{G}^H \boldsymbol{M}(f) \mathrm{d}f, \tag{4.7}$$

which is Hermitian positive (semi-)definite. Then the following convex subproblem is obtained:

$$\min_{\boldsymbol{h}} \ \boldsymbol{h}^H \boldsymbol{Z}(\boldsymbol{G}) \boldsymbol{h} \quad \text{ s. to } \quad \boldsymbol{D}^H \boldsymbol{h} = \boldsymbol{1}, \tag{4.8}$$

where $\boldsymbol{D} \in \mathbb{C}^{(L+H)\times(L-H)}$ comprises columns $H+1$ through L of $\boldsymbol{I}_{L+H}$, and $\boldsymbol{1} \in \mathbb{C}^{L-H}$ is the all-ones vector. The solution to optimal window design (4.8) can be readily found in closed form (see the details in Appendix A).

4.3.2. Optimal precoder for a given window

The PSD from (4.4) can be rewritten as

$$S_s(f) = \mathrm{tr}\{\boldsymbol{G}^H \boldsymbol{\Phi}(f;\boldsymbol{h}) \boldsymbol{G}\}, \tag{4.9}$$

where

$$\boldsymbol{\Phi}(f;\boldsymbol{h}) \triangleq \frac{|H_I(f)|^2}{LT_s}\boldsymbol{M}(f)\boldsymbol{h}\boldsymbol{h}^H\boldsymbol{M}^H(f). \tag{4.10}$$

Letting $\boldsymbol{A}_{\mathrm{W}}(\boldsymbol{h}) \triangleq \int_{-\infty}^{\infty} W(f)\boldsymbol{\Phi}(f;\boldsymbol{h})\mathrm{d}f$, the weighted power $\mathcal{P}_{\mathrm{W}}$ in (4.5) becomes

$$\mathcal{P}_{\mathrm{W}} = \mathrm{tr}\{\boldsymbol{G}^H\boldsymbol{A}_{\mathrm{W}}(\boldsymbol{h})\boldsymbol{G}\}. \tag{4.11}$$

- **Orthogonal precoder**
  With OP, the structural constraint on the precoder reads as $\boldsymbol{G}^H\boldsymbol{G} = \boldsymbol{I}_{K_d}$, yielding

  $$\min_{\boldsymbol{G}} \mathrm{tr}\{\boldsymbol{G}^H\boldsymbol{A}_{\mathrm{W}}(\boldsymbol{h})\boldsymbol{G}\} \quad \text{s. to} \quad \boldsymbol{G}^H\boldsymbol{G} = \boldsymbol{I}_{K_d}, \tag{4.12}$$

  whose solution $\boldsymbol{G}$ comprises the eigenvectors of $\boldsymbol{A}_{\mathrm{W}}(\boldsymbol{h})$ corresponding to the K_d smallest eigenvalues [123, 159].

- **AIC precoder**
  The data vector $\boldsymbol{d}[m]$ is directly mapped to K_d of the K active subcarriers, whereas the remaining $K_c = K - K_d$ subcarriers are used for cancellation. Let $\boldsymbol{S} \in \mathbb{C}^{K\times K_d}$ comprise the K_d columns of $\boldsymbol{I}_K$ corresponding to the indices of active subcarriers to which the data is directly mapped, and let $\boldsymbol{T} \in \mathbb{C}^{K\times(K-K_d)}$ comprise the remaining $K-K_d$ columns of $\boldsymbol{I}_K$. Then the structural constraint on the AIC precoder is $\boldsymbol{G} = \boldsymbol{S}+\boldsymbol{T}\boldsymbol{Q}$, where $\boldsymbol{S}$, $\boldsymbol{T}$ are fixed whereas $\boldsymbol{Q} \in \mathbb{C}^{(K-K_d)\times K_d}$ is a free parameter. Minimizing $\mathcal{P}_W = \mathrm{tr}\{(\boldsymbol{S}+\boldsymbol{T}\boldsymbol{Q})^H\boldsymbol{A}_{\mathrm{W}}(\boldsymbol{h})(\boldsymbol{S}+\boldsymbol{T}\boldsymbol{Q})\}$ with respect to $\boldsymbol{Q}$ is a convex quadratic problem with solution $\boldsymbol{Q} = -(\boldsymbol{T}^H\boldsymbol{A}_{\mathrm{W}}(\boldsymbol{h})\boldsymbol{T})^{-1}\boldsymbol{T}\boldsymbol{A}_{\mathrm{W}}(\boldsymbol{h})\boldsymbol{S}$. However, this may result in too much power being allocated to cancellation subcarriers, resulting in undesirably large PSD peaks. To control the size of these peaks, a regularization term can be introduced, leading to the following subproblem:

  $$\min_{\boldsymbol{Q}} \mathrm{tr}\{(\boldsymbol{S}+\boldsymbol{T}\boldsymbol{Q})^H\boldsymbol{A}_{\mathrm{W}}(\boldsymbol{h})(\boldsymbol{S}+\boldsymbol{T}\boldsymbol{Q})\} + \gamma\|\boldsymbol{Q}\|_F^2, \tag{4.13}$$

  where larger values of the regularization parameter $\gamma \geq 0$ will result in lower spectral peaks, but at the price of higher OBR. The solution to (4.13) is given by $\boldsymbol{Q} = -(\boldsymbol{T}^H\boldsymbol{A}_{\mathrm{W}}(\boldsymbol{h})\boldsymbol{T} + \gamma\boldsymbol{I}_{K_c})^{-1}\boldsymbol{T}\boldsymbol{A}_{\mathrm{W}}(\boldsymbol{h})\boldsymbol{S}$.

  Note that, in contrast to Chapter 3, where we used transmit power constraint to limit the spectral peaks, we have employed a regularization term in the cost function to design the AIC precoder, which has yielded almost identical results. This alternative approach is computationally simpler since the minimization problem can be solved in closed form without requiring GSVD decompositions or a bisection search for the Lagrange multiplier. For instance, with the approach in Chapter

3, given a value of β, we start by solving the LSQI problem and the corresponding Lagrange multiplier. Then, the value of the spectral peak is checked. If the peak is not within an acceptable range, the value of β is readjusted and the entire process is repeated until the intended spectral peak level is achieved. In contrast, the regularization approach involves a one-dimensional search over the parameter γ to obtain the desired peak value.

4.3.3. Cyclic optimization

To obtain an approximate solution to (4.6), we first initialize $\boldsymbol{h}_0$ as an RC window. Then, for $k \geq 1$, we solve:

$$\begin{aligned}
\text{OP:} \quad \boldsymbol{G}_k &= \arg\min_{\boldsymbol{G}} \mathcal{P}_{\mathrm{W}}(\boldsymbol{h}_{k-1}, \boldsymbol{G}) \\
&\quad \text{s. to} \quad \boldsymbol{G}^H \boldsymbol{G} = \boldsymbol{I}_{K_d} \qquad (4.14) \\
\text{AIC:} \quad \boldsymbol{G}_k &= \arg\min_{\boldsymbol{G}} \mathcal{P}_{\mathrm{W}}(\boldsymbol{h}_{k-1}, \boldsymbol{G}) + \gamma \|\boldsymbol{Q}\|_F^2 \\
&\quad \text{s. to} \quad \boldsymbol{G} = \boldsymbol{S} + \boldsymbol{T}\boldsymbol{Q} \qquad (4.15) \\
\text{OP \& AIC:} \quad \boldsymbol{h}_k &= \arg\min_{\boldsymbol{h}} \mathcal{P}_{\mathrm{W}}(\boldsymbol{h}, \boldsymbol{G}_k) \\
&\quad \text{s. to} \quad \boldsymbol{D}^H \boldsymbol{h} = \boldsymbol{1}. \qquad (4.16)
\end{aligned}$$

Note that the sequence of objective values $\mathcal{P}_{\mathrm{W}}(\boldsymbol{h}_k, \boldsymbol{G}_k)$ for OP, or $\mathcal{P}_{\mathrm{W}}(\boldsymbol{h}_k, \boldsymbol{G}_k) + \gamma \|\mathbf{Q}_k\|_F^2$ for AIC, is non-increasing and bounded below, so it must be convergent. Although there is no guarantee that the global optimum of (4.6) is found, simulation results validate the good performance of the proposed scheme.

4.4. Receiver, Efficiency, and Complexity

At the receiver end, after synchronization, the CP and the H overlapping samples between consecutive blocks are removed. After an N-point FFT and equalization, the vector $\boldsymbol{r} \in \mathbb{C}^K$ with the samples of active subcarriers is obtained. With OP, data can be estimated as $\mathrm{DEC}\{\boldsymbol{G}^H \boldsymbol{r}\}$, where $\mathrm{DEC}\{\cdot\}$ is an entrywise operator returning, for each entry, the closest symbol in the constellation; since $\boldsymbol{G}$ has orthonormal columns, noise enhancement is avoided. On the other hand, AIC is transparent to the receiver: data can be estimated as $\mathrm{DEC}\{\boldsymbol{S}^H \boldsymbol{r}\}$, *i.e.,* cancellation subcarriers are simply discarded.

Each OFDM block, carrying K_d data symbols, is sent every LT_s seconds,

so that the bit rate (in bits/s) can be expressed as

$$R_b = \frac{K_d . \log_2 M}{LT_s} = \frac{(K - K_c)\log_2 M}{(N + N_{\mathrm{CP}} + H)T_s} \tag{4.17}$$

where M is the modulation order. For the same effective CP length N_{CP}, the baseline is given by a system with no precoding ($K_c = 0$) and without windowing ($H = 0$), whose corresponding bit rate is $R_{b,\mathrm{ref}} = \frac{K \log_2 M}{(N+N_{\mathrm{CP}})T_s}$ bits/s. Hence, the metric for throughput efficiency is

$$\eta = \frac{R_b}{R_{b,\mathrm{ref}}} = \frac{1 - K_c/K}{1 + H/(N_{\mathrm{CP}} + N)}, \tag{4.18}$$

which depends on the relative precoder redundancy $\frac{K_c}{K}$ and the relative window redundancy $\frac{H}{N_{\mathrm{CP}}+N}$. Thus, a given efficiency η can be achieved with different (K_c, H) values, by using longer windows with fewer redundant subcarriers, or vice versa.

The proposed design is data-independent, so it can be computed offline. Regarding online complexity, windowing takes $2H$ complex multiplications per OFDM symbol (cm/symb) at the transmitter, whereas no additional complexity is incurred at the receiver; with respect to the precoder, one has:

- **OP.** The online complexity at each of transmitter and receiver is $K(K - K_c)$ cm/symb, if multiplication by $\boldsymbol{G}$ or $\boldsymbol{G}^H$ is implemented directly, but it becomes $K_c(2K - K_c)$ cm/symb with Clarkson's reduced complexity approach [140], which will be assumed in the sequel. With this, the total complexity including windowing and precoding is $2K_c(2K - K_c) + 2H$ cm/symb.
- **AIC.** At the transmitter, AIC requires $K_c(K - K_c)$ cm/symb. At the receiver end, the K_c cancellation subcarriers are just discarded, with no additional complexity. The total complexity is thus $K_c(K - K_c) + 2H$ cm/symb.

4.5. Results

We study the performance of the proposed *joint precoder and window* (JPW) design in a CP-OFDM system with IFFT size $N = 256$ and CP length $N_{\mathrm{CP}} = N/4$. The DAC filter is lowpass with $H_{\mathrm{I}}(f) = 1$ for $|f| \leq \frac{1}{2T_s}$ and zero otherwise. There are $K = 65$ active subcarriers, located symmetrically about the carrier frequency. The weighting function is $W(f) = 1, \forall \left\{ \frac{1}{8T_s} + \frac{\Delta_f}{2} \leq |f| \leq \frac{1}{2T_s} \right\}$, and zero otherwise.

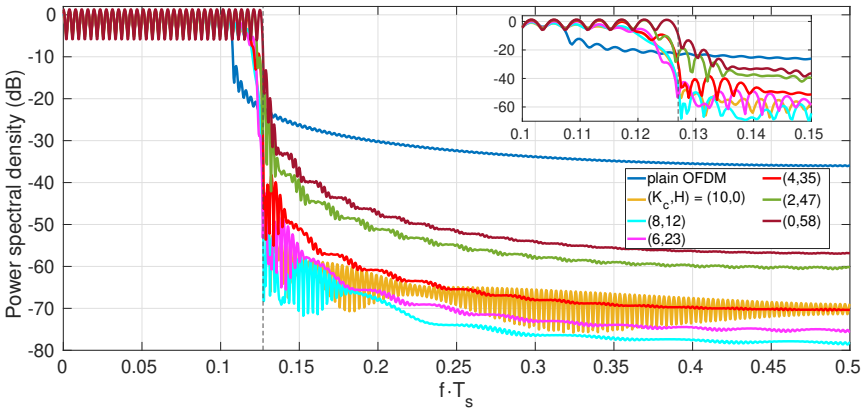

Figure 4.1: PSD of the proposed JPW-OP design for different (K_c, H) pairs. $\eta = 84.6\%$, $N = 256$, $N_{\text{CP}} = N/4$, $K = 65$.

Table 4.1: Online Complexity and OBR (relative to that of plain CP-OFDM with 10 null subcarriers) of JPW-OP and RC-OP. $\eta = 84.6\%$.

(K_c, H)	$(10, 0)$	$(8, 12)$	$(6, 23)$	$(4, 35)$	$(2, 47)$	$(0, 58)$
cm/symb	2400	1976	1534	1078	606	116
	100%	82.3%	63.9%	44.9%	25.2%	4.8%
OBR, dBr						
JPW-OP	-31.8	-36.1	-31.3	-24.1	-10.6	-3.9
RC-OP	-31.8	-30.6	-28.9	-22.8	-9.0	-2.8

4.5.1. Windowing and Orthogonal Precoding

For a given efficiency η, JPW provides the flexibility to trade off complexity and OBR reduction by choosing K_c and H. Fig. 4.1 shows the PSD obtained by JPW with orthogonal precoding (JPW-OP), along with that of standard CP-OFDM with 5 null subcarriers at each band edge, for the above system parameters and fixing $\eta = 84.6\%$. Note that $(K_c, H) = (10, 0)$ corresponds to orthogonal precoding with rectangular pulses, whereas $(K_c, H) = (0, 58)$ reduces to the optimal window design from Chapter 2 with no precoding. It is seen that windowing, by itself, is unable to provide a fast rolloff at the passband edge; an orthogonal precoder, without windowing, performs much better in this regard, but the associated online complexity is significantly higher. The tradeoff provided by JPW-OP is clearly seen in Fig. 4.1, and also in Table 4.1. For $(K_c, H) = (8, 12)$, JPW-OP provides a 4.3-dB OBR improvement with respect to the standard orthogonal precoder, with 82.3% of its complexity. With $(K_c, H) = (6, 23)$, complexity can be reduced to 63.9%, with just a small OBR degradation of 0.5 dB.

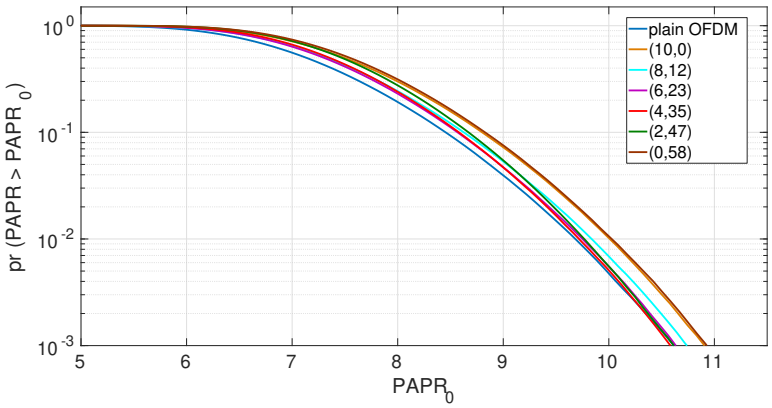

Figure 4.2: PAPR of the proposed JPW-OP design for the Fig. 4.1 with 16 QAM modulation.

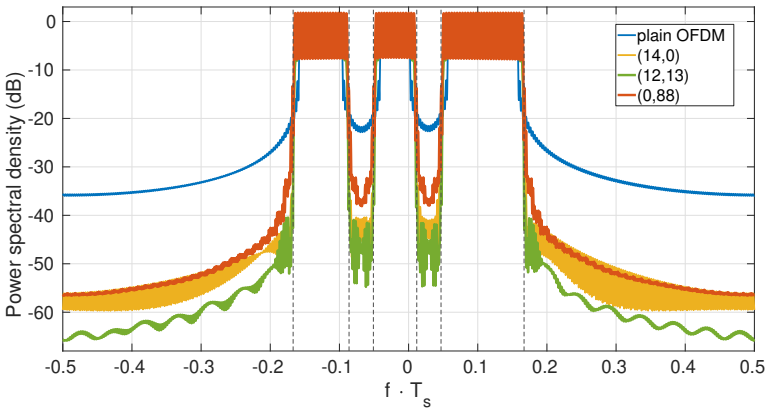

Figure 4.3: PSD of the proposed JPW-OP design in cognitive scenario. $\eta = 78.4\%$, $N = 256$, $N_{\text{CP}} = N/4$, $K = 65$.

JPW-OP also provides performance improvement in the cognitive radio scenario, where secondary user (SU) needs to protect the primary user (PU) which lies within the passband. Fig. 4.3 show the PSDs in this scenario with $K = 65$ active subcarriers in the above settings for efficiency $\eta = 78.4\%$. JPW-OP with $(K_c, H) = (12, 13)$ provides better PU band protection and sidelobe suppresion as compared to both orthogonal precoder without windowing and optimal window with no precoding. Additionally, the JPW-OP design has minimal or no impact on the PAPR as compared to the standard OFDM which is illustrated in Fig. 4.2.

Table 4.1 also shows the results for a simplified design in which the window is fixed to an RC pulse, and then the orthogonal precoder is optimized for this fixed window, as proposed in [158]. This approach, termed "RC-OP", corresponds to performing (4.14) for iteration $k = 1$ of the JPW-OP design,

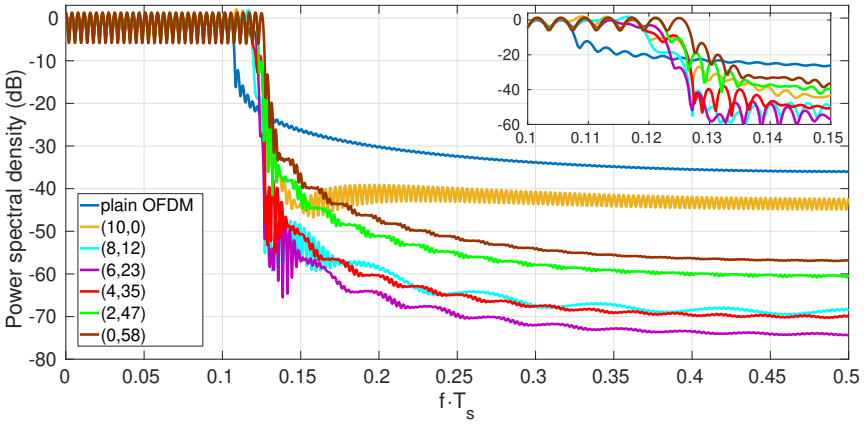

Figure 4.4: PSD of JPW-AIC for different (K_c, H) pairs. $\eta = 84.6\%$. Spectral peak is limited to 2 dB. $N = 256$, $N_{\mathrm{CP}} = N/4$, $K = 65$.

Table 4.2: Online Complexity and OBR (relative to that of plain CP-OFDM with 10 null subcarriers) of JPW-AIC and RC-AIC. $\eta = 84.6\%$, Spectral peak ≤ 2 dB.

(K_c, H)	$(10,0)$	$(8,12)$	$(6,23)$	$(4,35)$	$(2,47)$	$(0,58)$
cm/symb	550	480	400	314	220	116
	100%	87.3%	72.7%	57%	40%	21%
OBR, dBr						
JPW-AIC	−9.9	−28.3	−29.8	−23.6	−10.6	−3.9
RC-AIC	−9.9	−26.5	−27.8	−22.2	−9.0	−2.8

and then stopping. (We denote "RC-AIC" the analogous strategy for AIC precoders). Whereas JPW-OP and RC-OP have the same online complexity for a given (K_c, H) pair, it is seen that jointly optimizing the precoder and the pulse improves OBR performance, *e.g.,* by 5.5 dB for $(K_c, H) = (8, 12)$. Nevertheless, the RC-OP design may be attractive in dynamic spectrum access scenarios requiring frequent recomputation of precoder and window parameters due to the varying availability of spectral subbands.

4.5.2. Windowing and AIC precoding

In addition to being transparent to the receiver, AIC is computationally much simpler than orthogonal precoding. Thus, the online complexity of JPW with AIC precoding (JPW-AIC) is significantly lower than that of JPW-OP. Fig. 4.4 shows the corresponding PSDs for $\eta = 84.6\%$. In each case, half of the K_c cancellation subcarriers are placed at each of the

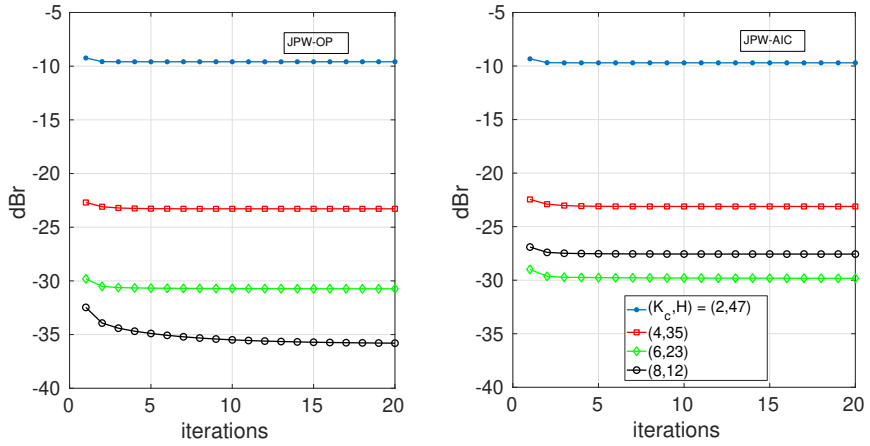

Figure 4.5: Convergence of the proposed designs in terms of OBR in the setting of Figs. 4.1 and 4.4.

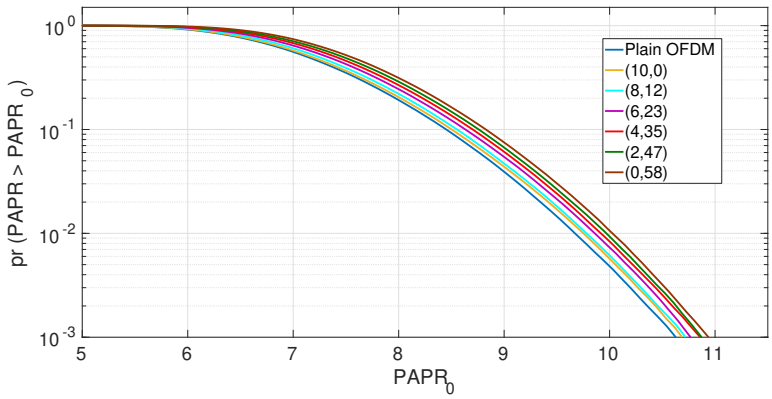

Figure 4.6: PAPR of JPW-AIC for the settings in Fig. 4.4 with 16-QAM modulation.

passband edges, and the regularization parameter γ is adjusted to prevent spectral peaks above 2 dB. It is seen that both AIC precoding without windowing, *i.e.*, $(K_c, H) = (10, 0)$, and windowing without precoding, *i.e.*, $(K_c, H) = (0, 58)$, present serious limitations in terms of sidelobe suppression. By suitably choosing (K_c, H), performance can be significantly improved, as seen in Fig. 4.4 and Table 4.2. As a side benefit, for $K_c \leq 6$, the joint use of windowing and precoding turns out to avoid spectral peaks altogether in this case. Fig. 4.5 shows the convergence of the cyclic scheme (4.14)-(4.16) in this setting. In addition, the JPW-AIC method does not have a significant impact on the PAPR as shown in Fig. 4.6.

Table 4.3: Online Complexity and OBR (relative to plain OFDM with null subcarriers) of different designs. $N = 256$, $K = 65$.

η	90.8%		87.7%		84.6%		81.5%		78.5%	
$N_{\text{CP}} = N/4$	cm/symb	dBr	cm/symb	dBr	cm/symb	dBr	cm/symb	dBr	cm/symb	dBr
OP (K_c)	1488 (6)	−14.5	1952 (8)	−22.8	2400 (10)	−31.8	2832 (12)	−41.4	3248 (14)	−51.1
AIC (K_c)	354 (6)	−6.3	456 (8)	−7.9	550 (10)	−9.8	636 (12)	−11.5	714 (14)	−13.3
W-OFDM (H)	33 (16)	−1.8	90 (45)	−3.2	116 (58)	−3.9	144 (72)	−4.7	176 (88)	−5.6
RC-OP (K_c, H)	1030 (4,11)	−14.5	1510 (6,11)	−23.5	1976 (8,12)	−30.6	2424 (10,12)	−33.0	2858 (12,13)	−37.2
JPW-OP (K_c, H)		−15.6		−24.6		−36.1		−47.1		−49.2
RC-AIC (K_c, H)	266 (4,11)	−12.7	376 (6,11)	−20.9	400 (6,23)	−27.8	504 (8,24)	−31.1	530 (8,37)	−32.3
JPW-AIC (K_c, H)		−14.2		−22.3		−29.8		−42.1		−50.8
$N_{\text{CP}} = N/16$	cm/symb	dBr	cm/symb	dBr	cm/symb	dBr	cm/symb	dBr	cm/symb	dBr
OP (K_c)	1488 (6)	−18.3	1952 (8)	−27.1	2400 (10)	−37.7	2832 (12)	−50.5	3248 (14)	−67.6
AIC (K_c)	354 (6)	−3.5	456 (8)	−4.5	550 (10)	−5.4	636 (12)	−6.9	714 (14)	−7.8
W-OFDM (H)	56 (28)	−1.9	76 (38)	−2.4	98 (49)	−3.1	124 (62)	−3.9	150 (75)	−4.7
RC-OP (K_c, H)	1026 (4,9)	−14.0	1508 (6,10)	−27.1	1528 (6,20)	−30.6	1994 (8,21)	−32.9	2442 (10,21)	−37.7
JPW-OP (K_c, H)		−15.3		−29.0		−35.5		−46.0		−60.3
RC-AIC (K_c, H)	262 (4,9)	−9.4	282 (4,19)	−14.5	394 (6,20)	−21.2	416 (6,31)	−30.4	440 (6,43)	−31.7
JPW-AIC (K_c, H)		−11.1		−16.4		−23.3		−35.4		−42.2

Interestingly, JPW-AIC may be able to provide OBR reduction levels comparable to those obtained with the standard (*i.e.,* no windowing) orthogonal precoder, with much less online complexity. From Tables 4.1 and 4.2, it is seen that for the same efficiency ($\eta = 84.6\%$), JPW-AIC with $(K_c, H) = (6, 23)$ performs only 2 dB worse in terms of OBR than the standard orthogonal precoder, with just $\frac{400}{2400} = 16.7\%$ of the complexity (which is all placed at the transmitter). This is further illustrated in Table 4.3, which shows the results obtained in this setting for two CP lengths ($N/4$ and $N/16$) and for different efficiency values, and where we have picked the pair (K_c, H) corresponding to the largest OBR reduction for JPW-OP and JPW-AIC in each case. For all AIC-based schemes, spectral peaks are kept below 2 dB.

The proposed JPW-AIC shows a similar performance in the cognitive radio scenario. Consider a SU having 107 active subcarriers to transmit with multiple PU bands within the passband which need to be protected. AIC precoding without windowing, *i.e.,* $(K_c, H) = (18, 0)$, has $K_c/6$ cancellation subcarriers located at each of the passband edge, and windowing without precoding is $(K_c, H) = (0, 65)$; both suffer in terms of OBR performance as seen in Fig. 4.7. On the other hand, with $(K_c, H) = (12, 22)$ which has $K_c/6$ subcarriers placed at each edge, OBR performance can be significantly improved.

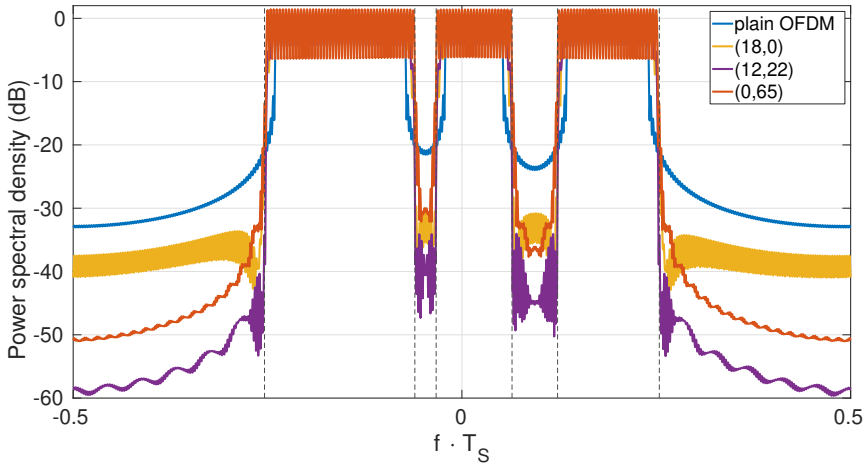

Figure 4.7: PSD of JPW-AIC for different (K_c, H) pairs. $\eta = 83.1\%$. Spectral peak is limited to 2 dB. $N = 256$, $N_{\mathrm{CP}} = N/4$, $K = 107$.

4.6. Conclusion

Energy efficiency is a critical aspect of wireless transceivers, and thus it is important to exploit all available tools at one's disposal to perform a given task with the lowest energy consumption. We have shown that, for multicarrier systems, the combination of spectral precoding and windowing has the potential to provide sidelobe suppression comparable to that of standard precoding while sustaining the same throughput, but with much less online complexity. The proposed design for jointly computing precoder and window coefficients can be run offline, and it can be flexibly adapted to emphasize suppression over a user-selectable frequency range.

Chapter 5

Memory-based spectral precoding

This chapter is adapted with permission of the coauthors and the editorial from IEEE: K. Hussain and R. López-Valcarce, Memory Tricks: Improving Active Interference Cancellation for Out-of-Band Power Reduction in OFDM, in 22nd IEEE International Workshop on Signal Processing Advances in Wireless Communications (SPAWC), 2021, pages 86-90, September 2021 Lucca, Italy. And with permission of the coauthors and the editorial from EURASIP: K. Hussain and R. López-Valcarce, Orthogonal precoding with memory for sidelobe suppression in OFDM, in 30th European Signal Processing Conference (EUSIPCO), 2022, pages , September 2022, Belgrade, Serbia.

5.1. Introduction

This chapter presents novel memory-based frequency-domain techniques to improve the OBR performance by suppressing the sidelobes of OFDM. As discussed in Chapter 1, the OBR problem has been addressed with a variety of techniques, such as: guard band insertion, multiple choice sequence methods, subcarrier weighting, constellation expansion, and phase adjustment, which are either spectrally inefficient or computationally expensive. Spectral precoding [118–124, 126–138] is an effective approach which may distort the original data sequence, so appropriate decoding may be required at the receiver to avoid error rate degradation. In some applications this approach is not feasible, e.g., according to the 3GPP NR specification [45], any operation performed on CP-OFDM at the transmitter side must be re-

ceiver agnostic [152]. In Active interference cancellation (AIC) [113, 116] techniques, the data subcarriers are not modified, and the receiver simply discards the cancellation subcarriers, so that no decoding is needed. Thus, AIC is completely transparent to the receiver [114, 160]. Since the constraint of keeping data subcarriers unaltered leads to a lower reduction in OBR compared to general precoders that allow for some data distortion, it is of interest to investigate improved AIC schemes with better OBR performance.

AIC techniques usually modulate the cancellation subcarriers by some linear combination of the values transmitted in the data subcarriers of the *same* OFDM symbol [139], and thus they can be referred to as *memoryless*. The OBR reduction is achieved at the cost of spectral efficiency: the number of data symbols per block modulated onto K available subcarriers is $K - K_c$, where $K_c \geq 0$ can be thought of as the redundancy of the precoder. It is pertinent to ask whether performance could be improved by introducing memory in AIC precoding, so that the data from OFDM symbols other than the current one affects the computation of the cancellation weights. For example, the design from [128] imposes continuity of the time-domain signal and a certain number of its derivatives at the transition between consecutive symbols, resulting in a memory precoder (a first-order infinite impulse response (IIR) filter applied to the OFDM symbol sequence) which provides good OBR performance but suffers from two drawbacks: it does not allow to give more emphasis to the effect of OBR in a particular frequency region over others; and it tends to yield large overshoot values in the power spectral density (PSD), unless a large fraction of subcarriers is reserved for cancellation purposes. A modification was proposed in [161], which constrains the power of reserved subcarriers; although this may be effective in controlling PSD overshoot, it results in significant performance loss and requires to solve an optimization problem for each OFDM symbol, which has high online complexity.

We present AIC memory precoders based on finite impulse response (FIR) filters. Based on the expression for the PSD under memory precoding, the proposed memory-AIC design minimizes OBR over a user-selectable frequency region and allows for effective control of PSD overshoot. Precoder coefficients are data-independent and can be computed offline. Simulation results illustrate the design tradeoffs involving OBR reduction, spectral efficiency, complexity, and spectral overshoot.

The proposed idea of memory-based AIC is well suited to systems in which complexity at the receiver must be kept at a minimum (it only needs to discard samples received in reserved subcarriers), but its sidelobe suppression is limited. On the other hand, spectral precoding generally provides

good OBR performance, but some appropriate decoding may be required at the receiver side to avoid symbol error rate (SER) degradation. In orthogonal precoding, the precoder matrix is semi-unitary, i.e., with orthonormal columns; due to this property, the receiver can easily invert the precoding operation, avoiding noise enhancement and hence SER degradation. The OBR reduction is achieved at the expense of spectral efficiency, and in scenarios with limited bandwidth orthogonal precoding may not be optimal. Orthogonal precoding belongs to the category of memoryless precoding. N-continuous precoding is a class of memory precoding techniques based on the application of a first-order IIR filter to the data sequence; however these designs are not flexible in the sense that it does not allow to select the frequency range of interest, or to adjust the level of spectral overshoot within the passband. It is pertinent to ask whether spectral precoder performance could be improved by introducing memory in orthogonal precoding, so that the data from OFDM symbols other than the current one can also be used to compute the coefficients.

Thus, we present a novel memory-based extension of orthogonal precoders resulting in finite impulse response (FIR) filtering of the data sequence, with filter coefficients designed to minimize OBR over a selectable frequency region, and with controllable spectral overshoot. A decision-feedback decoder effectively avoids SER degradation at the receiver. Similar to memory-AIC, the proposed design is data-independent. Simulation results show how the introduction of memory in the precoding operation helps improve the tradeoff between sidelobe suppression and spectral efficiency, at the cost of extra computational resources at the transmitter and receiver.

5.2. Signal Model

Following the model from Sec. 1.5, the general form of the power spectral density (PSD) of the multicarrier signal $s(t)$ defined in (1.1)-(1.2) is given by

$$S_s(f) = \frac{|H_{\mathrm{I}}(f)|^2}{LT_s} \boldsymbol{\phi}^H(f) \boldsymbol{S}_x(Lf) \boldsymbol{\phi}(f), \tag{5.1}$$

where $\boldsymbol{S}_x(f) = \sum_\ell \mathbb{E}\{\boldsymbol{x}[m]\boldsymbol{x}^H[m-\ell]\} e^{-j2\pi f T_s \ell}$. We focus on linear time-invariant memory precoders, for which $\boldsymbol{x}[m]$ is generated from the data sequence $\boldsymbol{d}[m]$ as

$$\boldsymbol{x}[m] = \sum_\ell \boldsymbol{G}[\ell] \boldsymbol{d}[m-\ell] \tag{5.2}$$

where $\boldsymbol{G}[\ell] \in \mathbb{C}^{K \times K_d}$. The standard memoryless precoder architecture is obtained if $\boldsymbol{G}[\ell] = \boldsymbol{0}$ for $\ell \neq 0$ in (5.2). Assuming the data sequence is zero-mean and wide-sense stationary with $\mathbb{E}\{\boldsymbol{d}[m]\boldsymbol{d}^H[m-\ell]\} = \delta[\ell]\boldsymbol{I}_{K_d}$, then

$\boldsymbol{S}_x(f)$ in (5.1) becomes $\boldsymbol{S}_x(f) = \boldsymbol{G}(f)\boldsymbol{G}^H(f)$, where

$$\boldsymbol{G}(f) \triangleq \sum_{\ell} \boldsymbol{G}[\ell] e^{-j2\pi f T_s \ell} \tag{5.3}$$

is the precoder transfer function. Hence, (5.1) becomes

$$S_s(f) = \frac{|H_{\mathrm{I}}(f)|^2}{LT_s} \left\| \boldsymbol{G}^H(Lf)\boldsymbol{\phi}(f) \right\|^2. \tag{5.4}$$

For a real-valued nonnegative weighting function $W(f)$, let $\widetilde{W}(f) \triangleq W(f)\frac{|H_{\mathrm{I}}(f)|^2}{LT_s}$. Then, the weighted power of $s(t)$ is

$$\begin{aligned} \mathcal{P}_W &= \int_{-\infty}^{\infty} W(f) S_s(f) df \\ &= \mathrm{tr} \int_{-\infty}^{\infty} \widetilde{W}(f) \boldsymbol{G}^H(Lf)\boldsymbol{\phi}(f)\boldsymbol{\phi}^H(f)\boldsymbol{G}(Lf) df \\ &= \mathrm{tr} \sum_{\ell} \sum_{\ell'} \boldsymbol{G}^H[\ell'] \boldsymbol{\Phi}[\ell - \ell'] \boldsymbol{G}[\ell], \end{aligned} \tag{5.5}$$

where, for integer b, we have introduced the $K \times K$ matrices

$$\boldsymbol{\Phi}[b] \triangleq \int_{-\infty}^{\infty} \widetilde{W}(f) \boldsymbol{\phi}(f) \boldsymbol{\phi}^H(f) e^{-j2\pi L f T_s b} df. \tag{5.6}$$

Thus, (5.5) gives the weighted power $\mathcal{P}_W$ as a quadratic function of the precoder impulse response coefficients $\boldsymbol{G}[\ell]$. More explicitly, and assuming an FIR precoder, let $\boldsymbol{G}[\ell] = \boldsymbol{0}$ for $\ell < -\ell_1$ and $\ell > \ell_2$, with $-\ell_1 \leq 0 \leq \ell_2$. Note that if we define a precoder $\boldsymbol{F}[m] = \boldsymbol{G}[m - \ell_1]$, then $\boldsymbol{F}[m]$ is nonzero only for $m = 0, 1, ..., \ell_1 + \ell_2$, so that it is FIR of the same order and causal. Moreover, it is readily checked that the weighted power (5.5) obtained with $\boldsymbol{F}$ is the same as with $\boldsymbol{G}$. Therefore we can assume without loss of generality that the FIR precoder is causal, i.e., we can take $\ell_1 = 0$ and $\ell_2 = \ell_0$. Let ℓ_0 be the precoder order, and introduce the matrices

$$\boldsymbol{G} \triangleq \begin{bmatrix} \boldsymbol{G}^H[0] & \boldsymbol{G}^H[1] & \boldsymbol{G}^H[2] & \cdots \boldsymbol{G}^H[\ell_0] \end{bmatrix}^H, \tag{5.7}$$

$$\boldsymbol{\Phi} \triangleq \begin{bmatrix} \boldsymbol{\Phi}[0] & \boldsymbol{\Phi}[1] & \cdots & \boldsymbol{\Phi}[\ell_0] \\ \boldsymbol{\Phi}^H[1] & \boldsymbol{\Phi}[0] & \cdots & \boldsymbol{\Phi}[\ell_0 - 1] \\ \vdots & \vdots & \ddots & \vdots \\ \boldsymbol{\Phi}^H[\ell_0] & \boldsymbol{\Phi}^H[\ell_0 - 1] & \cdots & \boldsymbol{\Phi}[0] \end{bmatrix}, \tag{5.8}$$

which have sizes $(\ell_0 + 1)K \times K_d$ and $(\ell_0 + 1)K \times (\ell_0 + 1)K$ respectively. Note that $\boldsymbol{\Phi}$ is block-Toeplitz and Hermitian. Then (5.5) can be rewritten as

$$\mathcal{P}_W = \mathrm{tr}\left\{ \boldsymbol{G}^H \boldsymbol{\Phi} \boldsymbol{G} \right\}. \tag{5.9}$$

5.3. Proposed Memory AIC Precoder

In AIC, the set of active subcarriers is split between data and cancellation subcarriers. Thus, the data vector $\boldsymbol{d}[m]$ is directly mapped to K_d of the K active subcarriers, whereas the remaining $K_c = K - K_d$ subcarriers are used for cancellation. Let $\boldsymbol{S} \in \mathbb{C}^{K \times K_d}$ comprise the K_d columns of the identity matrix $\boldsymbol{I}_K$ corresponding to the indices of the active subcarriers to which the data is directly mapped, and let $\boldsymbol{T} \in \mathbb{C}^{K \times K_c}$ comprise the remaining K_c columns of $\boldsymbol{I}_K$. The impulse response of the memory AIC precoder must be given by

$$\boldsymbol{G}[0] = \boldsymbol{S} + \boldsymbol{T}\boldsymbol{Q}[0], \quad \boldsymbol{G}[\ell] = \boldsymbol{T}\boldsymbol{Q}[\ell] \text{ for } \ell = 1, 2, \ldots, \ell_0, \tag{5.10}$$

where $\boldsymbol{Q}[\ell]$ are $K_c \times K_d$ matrices. Therefore, the precoded vector in (5.2) becomes

$$\boldsymbol{x}[m] = \sum_{\ell} \boldsymbol{G}[\ell]\boldsymbol{d}[m-\ell] = \boldsymbol{S}\boldsymbol{d}[m] + \boldsymbol{T}\sum_{\ell=0}^{\ell_0} \boldsymbol{Q}[\ell]\boldsymbol{d}[m-\ell]. \tag{5.11}$$

Since $\boldsymbol{S}^H\boldsymbol{S} = \boldsymbol{I}_{K_d}$ and $\boldsymbol{S}^H\boldsymbol{T} = \boldsymbol{0}$, it is clear that $\boldsymbol{S}^H\boldsymbol{x}[m] = \boldsymbol{d}[m]$, so that $\boldsymbol{d}[m]$ can be recovered from $\boldsymbol{x}[m]$ by discarding the cancellation subcarriers. For an FIR AIC precoder as in (5.7), $\boldsymbol{G}$ can be written as

$$\boldsymbol{G} = \widetilde{\boldsymbol{S}} + \widetilde{\boldsymbol{T}}\boldsymbol{Q}, \tag{5.12}$$

where $\widetilde{\boldsymbol{T}} = \boldsymbol{I}_{\ell_0+1} \otimes \boldsymbol{T}$ with '$\otimes$' the Kronecker product, and

$$\widetilde{\boldsymbol{S}} = \begin{bmatrix} \boldsymbol{S}^H & \boldsymbol{0}^H_{\ell_0 K \times K_d} \end{bmatrix}^H \tag{5.13}$$

$$\boldsymbol{Q} = \begin{bmatrix} \boldsymbol{Q}^H[0] & \boldsymbol{Q}^H[1] & \boldsymbol{Q}^H[2] & \cdots & \boldsymbol{Q}^H[\ell_0] \end{bmatrix}^H. \tag{5.14}$$

The goal is to pick $\{\boldsymbol{Q}[\ell]\}$ to minimize OBR. The OBR is computed via (5.5) by choosing a weighting function $W(f) > 0$ for $f \in \mathbb{B}$, and $W(f) = 0$ outside $\mathbb{B}$. $\mathbb{B}$ is the set of frequencies over which OBR is to be mitigated, and it may include parts within the passband of data subcarriers. Also, cancellation subcarriers may be located inside and/or outside $\mathbb{B}$. The choice of values of $W(f)$ over $\mathbb{B}$ allows to emphasize OBR reduction in certain subbands over others. The problem can be stated as:

$$\min_{\boldsymbol{Q}} \mathcal{P}_{\mathrm{W}} = \mathrm{tr}\{(\widetilde{\boldsymbol{S}} + \widetilde{\boldsymbol{T}}\boldsymbol{Q})^H \boldsymbol{\Phi} (\widetilde{\boldsymbol{S}} + \widetilde{\boldsymbol{T}}\boldsymbol{Q})\}. \tag{5.15}$$

The problem (5.17) is a convex quadratic problem, and the solution is given by

$$\boldsymbol{Q} = -\left(\widetilde{\boldsymbol{T}}^H \boldsymbol{\Phi} \widetilde{\boldsymbol{T}}\right)^{-1} \left(\widetilde{\boldsymbol{T}}^H \boldsymbol{\Phi} \widetilde{\boldsymbol{S}}\right). \tag{5.16}$$

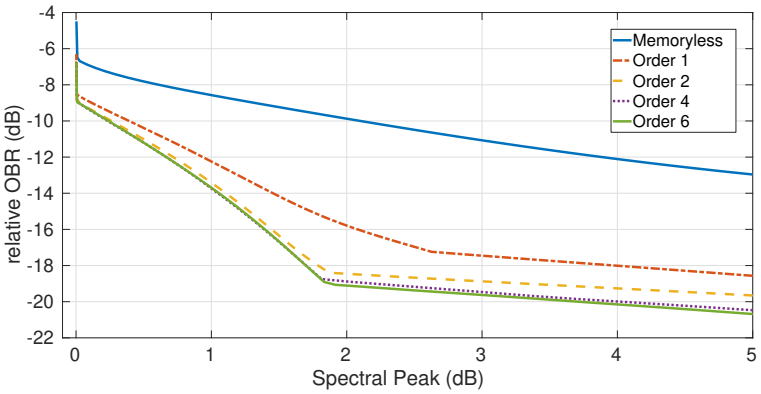

Figure 5.1: OBR achieved with AIC precoders (relative to that of the unprecoded system) as a function of spectral overshoot. $K_d = 53$ data subcarriers.

However, it can also lead to excessive power allocation to cancellation subcarriers, resulting in undesirably high PSD peaks. To mitigate the impact of these peaks, a regularization term is incorporated, similar to the one introduced in Chapter 4. This gives rise to the following problem:

$$\min_{\boldsymbol{Q}} \operatorname{tr}\{(\widetilde{\boldsymbol{S}} + \widetilde{\boldsymbol{T}}\boldsymbol{Q})^H \boldsymbol{\Phi}(\widetilde{\boldsymbol{S}} + \widetilde{\boldsymbol{T}}\boldsymbol{Q})\} + \gamma \|\boldsymbol{Q}\|_F^2, \tag{5.17}$$

where $\gamma \geq 0$ is the regularization parameter. Larger values of γ will result in lower spectral peaks at the cost of higher OBR. The solution is given as

$$\boldsymbol{Q} = -\left[\widetilde{\boldsymbol{T}}^H \boldsymbol{\Phi} \widetilde{\boldsymbol{T}} + \gamma \boldsymbol{I}_{(\ell_0+1)K_c}\right]^{-1} \left[\widetilde{\boldsymbol{T}}^H \boldsymbol{\Phi} \widetilde{\boldsymbol{S}}\right]. \tag{5.18}$$

5.3.1. Results and Discussion

Consider a CP-OFDM scenario with IFFT size $N = 128$ and CP length $N/16$. The interpolation filter is taken as an ideal lowpass filter with $H_{\mathrm{I}}(f) = 1$ for $|f| \leq \frac{1}{2T_s}$ and zero otherwise. Transmission is intended in the passband $|f| \leq \frac{1}{4T_s} + \frac{\Delta f}{2}$, in which a maximum of $\frac{N}{2} + 1 = 65$ subcarriers can be accommodated; thus, $K_d \leq 65$. The OBR is to be minimized over the region

$$\mathcal{B} = \left\{ f \;\middle|\; \frac{1}{4T_s} + \frac{\Delta f}{2} \leq |f| \leq \frac{1}{2T_s} \right\}, \tag{5.19}$$

with $W(f) = 1$ for $f \in \mathbb{B}$, and zero elsewhere. The number of active subcarriers is K (thus including those in $\mathbb{B}$), so that the number of cancellation subcarriers is $K_c = K - K_d$. Data subcarriers are located symmetrically about the carrier frequency.

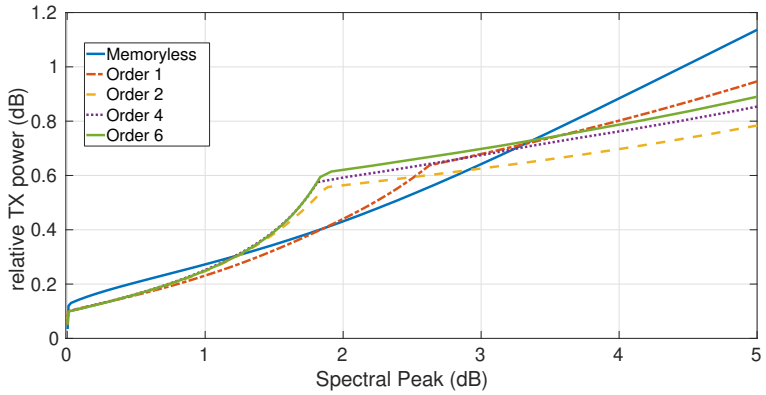

Figure 5.2: Transmit power of AIC precoders (relative to that of the unprecoded system) as a function of spectral overshoot. $K_d = 53$ data subcarriers.

Peak vs OBR

The OBR performance is influenced by the allowed spectral peak. Better performance can be achieved at the cost of large undesirable spectral peaks. As γ approaches 0, more power is available to cancel subcarriers, resulting in effective OBR reduction. However, this may also lead to larger peaks in the Power Spectral Density (PSD) and an increase in transmit power. On the other hand, increasing the regularization parameter γ reduces spectral peaks, but at the cost of OBR performance. This spectral overshoot is undesirable in practice, because spectral emission masks place upper bounds on the PSD relative to its maximum value. Hence, a tradeoff must be found between OBR performance and spectral overshoot. To illustrate this, consider the setting described above, with data transmission making use of the central $K_d = 53$ subcarriers for an efficiency of $\frac{53}{65} = 81.5\%$. The standard memoryless AIC precoder is considered, together with the proposed FIR designs of first, second and fourth, for which $\ell_0 = 1$, 2, 4 and 6 respectively. The curves of OBR and spectral peak size are shown in Fig. 5.1, and the corresponding curves of transmit power are shown in Fig. 5.2. As γ approaches 0 (right side of the figure), the AIC design achieves good OBR reduction, however the spectral peaks become very large along with an increase in the TX power (less than 1 dB for the spectral peak of 5 dB in this scenario). On the other hand, as γ is increased, the spectral overshoot start decreasing at the expense of OBR. For small spectral overshoot, which is of practical interest, it is clear that a much better tradeoff can be achieved with memory AIC precoders, since their corresponding curves in Fig. 5.1 are much steeper than that of the memoryless AIC precoder. Moreover, the TX power is similar to that of memoryless in the region of interest.

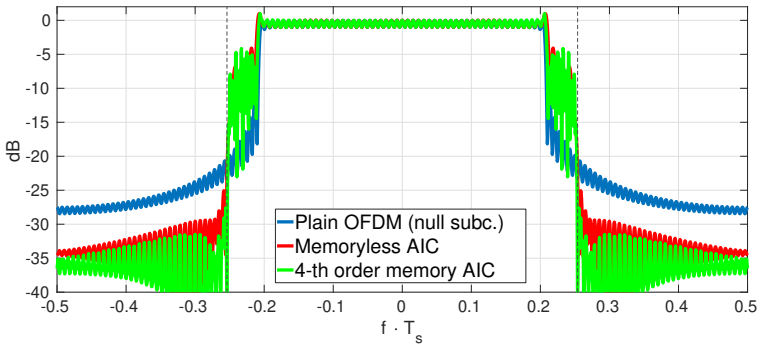

Figure 5.3: PSDs for 1-dB spectral overshoot. $K_d = 53$ data subcarriers. Dashed vertical lines mark the OBR region $\mathbb{B}$.

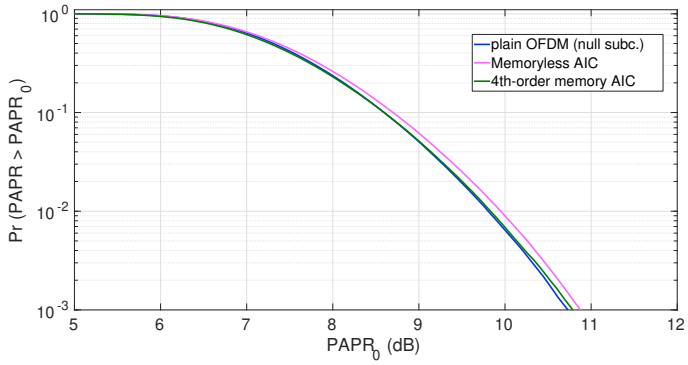

Figure 5.4: PAPR of the different designs in Fig. 5.3 with 16-QAM modulation.

Benefits of memory precoding

Fig. 5.3 shows the PSD obtained in the setting above, and computed via (5.1), again for $K_d = 53$ data subcarriers, and for three cases: an unprecoded system (only K_d subcarriers active), memoryless AIC, and the proposed AIC design of order 4 ($\ell_0 = 4$). For both AIC schemes, γ was set for a 1-dB spectral peak. The memory-based design clearly improves upon the standard memoryless AIC scheme; in terms of OBR reduction the improvement is ≈ 5 dB in this example. Additionally, the proposed AIC design does not result in an increase in peak-to-average power ratio (PAPR). Fig. 5.4 show the PAPR of the above three cases with 16-QAM modulation.

The memory-based AIC design also improves the OBR performance in cognitive radio scenarios. Three different cognitive scenarios are considered in the same settings as before. Scenario 1 has $K = 58$ subcarriers which are located symmetrically around the passband. Scenario 2 has $K = 62$

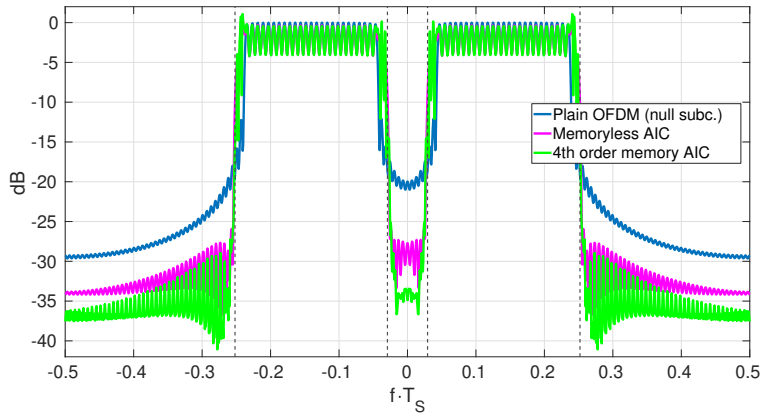

Figure 5.5: PSDs in cognitive radio Scenario 1. Spectral overshoot is limited to 1-dB.

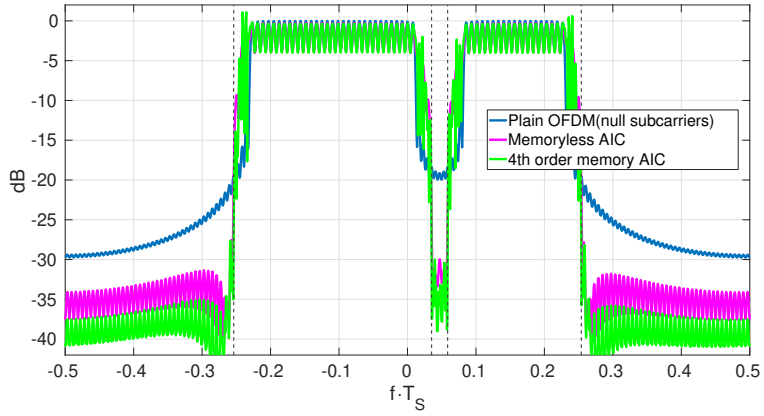

Figure 5.6: PSDs in cognitive radio Scenario 2. Spectral overshoot is limited to 1-dB.

subcarriers, which are located asymmetrically around the PU band. Finally, Scenario 3 has multiple PU subbands within the passband that needs to be protected and SU can transmit on $K = 55$ subcarriers. In all scenarios, $K - K_d = 12$ cancellation subcarriers are used for OBR reduction, which are equally divided and located on each spectrum edge. The spectral peak is limited to 1-dB. The spectral weighting function $W(f) = 1$ for $f \in \mathbb{B}$, and zero otherwise; and the OBR regions are specified in the figures for each scenario.

Fig. 5.5 shows the PSD of the proposed AIC design of order 4 ($\ell_0 = 4$) and memoryless AIC, along with unprecoded system in Scenario 1. Clearly the memory AIC design improves OBR performance ($\approx$ 3.8 dB) as compared to the standard memoryless AIC scheme. In Fig. 5.6, the PSD of the

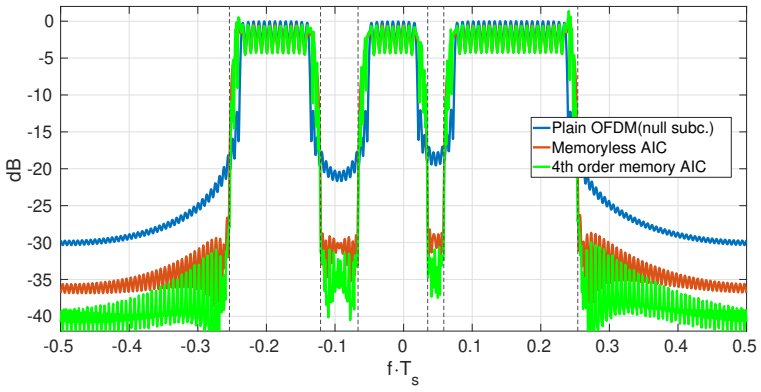

Figure 5.7: PSDs in cognitive radio Scenario 3. Spectral overshoot is limited to 1-dB.

4-th order memory AIC design ($\ell_0 = 4$) along with memoryless AIC and unprecoded system are shown in cognitive radio Scenario 2. The introduction of memory improves OBR performance by ≈ 3.2 dB. Lastly, the cognitive radio Scenario 3 is shown in Fig. 5.7, where the SU needs to protect multiple PU bands. As shown in the figure, the proposed 4-th order memory AIC design ($\ell_0 = 4$) provides more protection to the PU subbands as compared to the memoryless AIC; and the improvement in this case is ≈ 4 dB.

For a given value of the maximum spectral peak, the only way to further reduce OBR with the memoryless AIC scheme is to increase the number of cancellation subcarriers, at the expense of reducing the spectral efficiency of the system. As shown in Fig. 5.3, the introduction of memory provides an alternative, by which OBR performance can be improved without degrading spectral efficiency.

This fact is further illustrated in Fig. 5.8, which represents the OBR performance in the same setting of Fig. 5.3 as a function of the order of the memory AIC precoder (zeroth-order corresponds to the standard memoryless design), and for different values of the number of data subcarriers K_d, when the spectral peak is limited to 1 dB. It is seen that for a given precoder order, performance improves as the number of cancellation subcarriers increases, as expected. In addition, for a given value of K_d, performance also improves as the precoder order is increased. The obtained gains eventually saturate, since the contribution of symbols far away from the current one becomes less significant; therefore, there seems to be little incentive to consider memory precoders of order larger than four. This trend has also been observed in other settings in all experiments conducted. Fig. 5.8 also shows the spectral efficiency savings that can be obtained by introducing memory in the AIC precoder: for example, the performance of the memoryless pre-

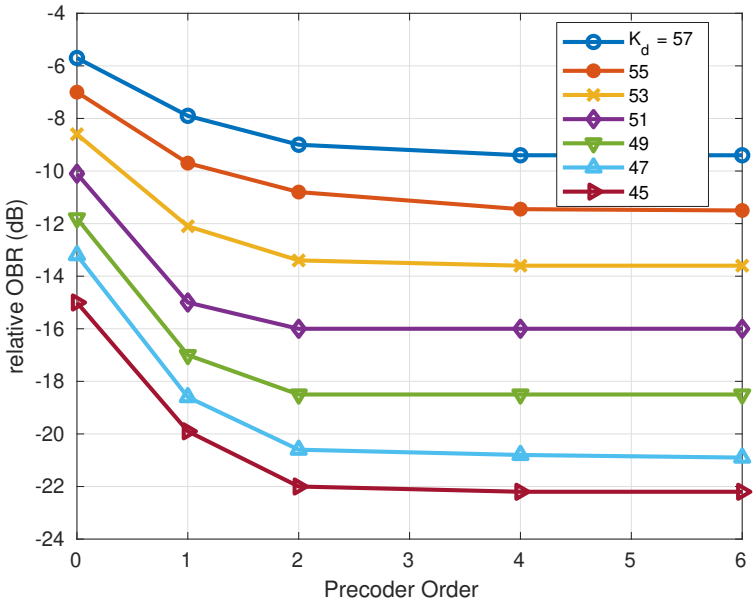

Figure 5.8: OBR (relative to that of the unprecoded system) with memory AIC precoders of different orders, and for different number of data subcarriers K_d. Spectral overshoot is kept at 1 dB in all cases.

coder with $K_d = 47$ (efficiency $\frac{47}{65} = 72.3\%$) can be achieved either with a second-order design and $K_d = 53$ (81.53%). Analogously, the performance of the memoryless precoder with $K_d = 45$ (69.2%) can be achieved with a first-order design and $K_d = 51$ (78.4%).

Computational complexity

The design of the AIC precoder coefficients is data-independent, and thus it can be performed offline; although in DSS scenarios in which spectral occupancy by other users changes dynamically, it may become necessary to recompute the precoders on the fly. Computation of the coefficients via (5.18) is dominated by the inversion of matrix of size $(\ell_0+1)K_c \times (\ell_0+1)K_c$ in (5.18). Thus, offline computational complexity is $O((\ell_0+1)^3 K_c^3)$. On the other hand, online operation is determined by (5.11), with complexity $O(\ell_0(K-K_d)K_d)$; this cost is incurred at the transmitter side. Therefore, the benefits of introducing memory in AIC precoders come at the price of increased computational complexity, both offline (cubic in the precoder order ℓ_0) and online (linear in ℓ_0).

5.4. Proposed Orthogonal Memory Precoder

The memory AIC design in section 5.3 does not modify the data subcarriers, and the receiver simply discards the cancellation subcarriers. On the other hand, the orthogonal memory precoder design modifies the data subcarriers to improve the OBR performance. The goal is to minimize the OBR over some region $\mathbb{B}$. The OBR is defined as $\mathcal{P}_W = \mathrm{tr}\left\{\boldsymbol{G}^H\boldsymbol{\Phi}\boldsymbol{G}\right\}$ for some $W(f) \in \mathbb{B}$ and zero elsewhere. The problem can be stated as

$$\min_{\boldsymbol{G}} \mathcal{P}_W \quad \text{s.to} \quad \boldsymbol{G}^H[0]\boldsymbol{G}[0] = \boldsymbol{I}_{K_d}, \tag{5.20}$$

where $K_c = K - K_d$ is the redundancy of the precoder. Letting $\widetilde{\boldsymbol{G}} = \left[\boldsymbol{G}^H[1]\ \boldsymbol{G}^H[2]\ \cdots\ \boldsymbol{G}^H[\ell_0]\right]^H$, problem (5.20) becomes

$$\min_{\boldsymbol{G}=\left[\boldsymbol{G}^H[0]\ \widetilde{\boldsymbol{G}}^H\right]^H} \mathrm{tr}\{\boldsymbol{G}^H\boldsymbol{\Phi}\boldsymbol{G}\} \quad \text{s.to} \quad \boldsymbol{G}^H[0]\boldsymbol{G}[0] = \boldsymbol{I}_{K_d}. \tag{5.21}$$

Note that the presence of $\widetilde{\boldsymbol{G}}$ may result in undesirably large PSD peaks; thus, to control the size of these peaks, a regularization term can be introduced, and the problem becomes:

$$\min_{\boldsymbol{G}=\left[\boldsymbol{G}[0]\ \ \widetilde{\boldsymbol{G}}\right]} \mathrm{tr}\{\boldsymbol{G}^H\boldsymbol{\Phi}\boldsymbol{G}\} + \gamma\|\tilde{\boldsymbol{G}}\|_F^2 \quad \text{s.to} \quad \boldsymbol{G}^H[0]\boldsymbol{G}[0] = \boldsymbol{I}_{K_d}, \tag{5.22}$$

where larger values of the regularization parameter $\gamma \geq 0$ will result in lower spectral peak. The problem (5.22) is not convex due to the orthonormality constraint on the columns of $\boldsymbol{G}[0]$. Note that $\widetilde{\boldsymbol{G}}$ is not affected by the constraint in (5.21); thus, for $\boldsymbol{G}[0]$ given, $\widetilde{\boldsymbol{G}}$ is the solution to

$$\min_{\tilde{\boldsymbol{G}}} \mathrm{tr}\{\boldsymbol{G}^H\boldsymbol{\Phi}\boldsymbol{G}\} + \gamma\|\tilde{\boldsymbol{G}}\|_F^2. \tag{5.23}$$

Let $c = \mathrm{tr}\{\boldsymbol{G}^H[0]\boldsymbol{\Phi}[0]\boldsymbol{G}[0]\}$, and define the submatrices

$$\boldsymbol{Y} = \begin{bmatrix} \boldsymbol{\Phi}[0] & \boldsymbol{\Phi}[1] & \cdots & \boldsymbol{\Phi}[\ell_0-1] \\ \boldsymbol{\Phi}^H[1] & \boldsymbol{\Phi}[0] & \cdots & \boldsymbol{\Phi}[\ell_0-2] \\ \vdots & \vdots & \ddots & \vdots \\ \boldsymbol{\Phi}^H[\ell_0-1] & \boldsymbol{\Phi}^H[\ell_0-1] & \cdots & \boldsymbol{\Phi}[0] \end{bmatrix} \tag{5.24}$$

$$\boldsymbol{X} = \begin{bmatrix} \boldsymbol{\Phi}[1] & \boldsymbol{\Phi}[2] & \cdots & \boldsymbol{\Phi}[\ell_0] \end{bmatrix} \tag{5.25}$$

so that

$$\boldsymbol{\Phi} = \begin{bmatrix} \boldsymbol{\Phi}[0] & \boldsymbol{X} \\ \boldsymbol{X}^H & \boldsymbol{Y} \end{bmatrix}. \tag{5.26}$$

Then (5.23) becomes

$$\min_{\widetilde{\boldsymbol{G}}} \operatorname{tr}\{\widetilde{\boldsymbol{G}}^H(\boldsymbol{Y}+\gamma \boldsymbol{I}_{\ell_0 K})\widetilde{\boldsymbol{G}}\} + 2Re\operatorname{tr}\{\widetilde{\boldsymbol{G}}^H \boldsymbol{X}\boldsymbol{G}[0]\} + c \tag{5.27}$$

The solution to (5.27) is given by

$$\widetilde{\boldsymbol{G}} = -\boldsymbol{M}_\gamma \boldsymbol{G}_0, \tag{5.28}$$

$$\boldsymbol{M}_\gamma = (\boldsymbol{Y}+\gamma \boldsymbol{I}_{\ell_0 K})^{-1}\boldsymbol{X}. \tag{5.29}$$

Now, with $\boldsymbol{M}_\gamma$ as in (5.29), let us introduce the $K \times K$ matrices

$$\boldsymbol{A}_\gamma = \boldsymbol{\Phi}[0] - \boldsymbol{X}^H\boldsymbol{M}_\gamma - \boldsymbol{M}_\gamma^H\boldsymbol{X} + \boldsymbol{M}_\gamma^H(\boldsymbol{Y}+\gamma \boldsymbol{I}_{\ell_0 K})\boldsymbol{M}_\gamma. \tag{5.30}$$

Then, after substituting the expression in (5.27) of the optimal $\tilde{\boldsymbol{G}}$ into the cost function, the optimization problem (5.21) can be rewritten as

$$\min_{\boldsymbol{G}_0} \operatorname{tr}\{\boldsymbol{G}_0^H \boldsymbol{A}_\gamma \boldsymbol{G}_0\} \text{ s. to } \boldsymbol{G}_0^H\boldsymbol{G}_0 = \boldsymbol{I}_{K_d}. \tag{5.31}$$

The solution to (5.31) for a given γ, $\boldsymbol{G}_0$ comprises the K_d least dominant eigenvectors of $\boldsymbol{A}_\gamma$ [159]. If $\boldsymbol{G}_{0,\gamma}$ does not satisfy the desired peak levels, then it remains to determine the regularization parameter γ. This can be done by a one-dimensional search over the scalar parameter γ until the desired peak level is achieved.

5.4.1. Decoder

We constrain $\boldsymbol{G}[0]$ to have orthonormal columns, which allows the following decision feedback (DF) strategy for decoding. Let $\boldsymbol{r}[m]$ be the vector at the receiver after FFT, CP removal, and frequency-domain equalization; then $\boldsymbol{r}[m] = \sum_{\ell=0}^{\ell_0} \boldsymbol{G}[\ell]\boldsymbol{d}[m-\ell] + \boldsymbol{w}[m]$, where $\boldsymbol{w}[m]$ is the noise vector. The estimate of $\boldsymbol{d}[m]$ is obtained as

$$\hat{\boldsymbol{d}}[m] = \mathrm{DEC}\left\{\boldsymbol{G}^H[0]\left(\boldsymbol{r}[m] - \sum_{\ell=1}^{\ell_0}\boldsymbol{G}[\ell]\hat{\boldsymbol{d}}[m-\ell]\right)\right\}, \tag{5.32}$$

where $\mathrm{DEC}\{\cdot\}$ is an entrywise hard-decision operator, returning for each entry its closest point in the constellation. In the absence of error propagation, $\hat{\boldsymbol{d}}[m-\ell] \approx \boldsymbol{d}[m-\ell]$ for $1 \le \ell \le \ell_0$, so that $\boldsymbol{r}[m] - \sum_{\ell=1}^{\ell_0}\boldsymbol{G}[\ell]\hat{\boldsymbol{d}}[m-\ell] \approx \boldsymbol{G}[0]\boldsymbol{d}[m] + \boldsymbol{w}[m]$, and since $\boldsymbol{G}^H[0]\boldsymbol{G}[0] = \boldsymbol{I}_{K_d}$, the decision variable in (5.32) becomes

$$\boldsymbol{G}^H[0]\left(\boldsymbol{r}_m - \sum_{\ell=1}^{\ell_0}\boldsymbol{G}[\ell]\hat{\boldsymbol{d}}[m-\ell]\right) \approx \boldsymbol{d}[m] + \widetilde{\boldsymbol{w}}[m], \tag{5.33}$$

where $\widetilde{\boldsymbol{w}}[m] = \boldsymbol{G}^H[0]\boldsymbol{w}[m]$. Since $\mathbb{E}\{\|\widetilde{\boldsymbol{w}}[m]\|^2\} \le \mathbb{E}\{\|\boldsymbol{w}[m]\|^2\}$, see, e.g. [162], the DF decoder avoids noise enhancement.

5.4.2. Complexity Analysis

The computation of the orthogonal memory precoder can be performed offline. At each iteration, the matrices $\boldsymbol{M}_\gamma$ and $\boldsymbol{A}_\gamma$ must be obtained, followed by an eigenvalue decomposition (EVD) of $\boldsymbol{A}_\gamma$. Complexity is dominated by the matrix inversion required to obtain $\boldsymbol{M}_\gamma$, which is $\mathcal{O}(\ell_0^3 K^3)$ per iteration.

Regarding online complexity, for each OFDM symbol $\boldsymbol{d}[m]$ the transmitter needs to compute $\boldsymbol{x}[m] = \boldsymbol{G}[0]\boldsymbol{d}[m] + \boldsymbol{G}[1]\boldsymbol{d}[m-1] + \cdots + \boldsymbol{G}[\ell_0]\boldsymbol{d}[m-\ell_0]$. Since $\boldsymbol{G}[0]$ has orthonormal columns, the product $\boldsymbol{G}[0]\boldsymbol{d}[m]$ can be obtained with complexity $\mathcal{O}(K^2 - K_d^2)$ by using block reflectors [140]. For $\ell = 1, \ldots, \ell_0$, each of the products $\boldsymbol{G}[\ell]\boldsymbol{d}[m-\ell]$ requires in principle $\mathcal{O}(KK_d)$ operations. However, the matrices $\boldsymbol{G}[1], \ldots, \boldsymbol{G}[\ell_0]$ resulting from the proposed design usually exhibit a significant number of small singular values, suggesting that they can be replaced by their best low-rank approximations with very small performance loss. If the corresponding ranks are $r_1, \ldots, r_{\ell_0}$, then the computation of $\boldsymbol{x}_m$ is $\mathcal{O}((K + K_d)(K - K_d + r))$, where $r = r_1 + \cdots + r_{\ell_0}$. At the receiver side, the decoder (5.32) has to be implemented for each OFDM symbol; it is readily checked that the corresponding complexity is the same as that at the transmitter, i.e., $\mathcal{O}((K + K_d)(K - K_d + r))$.

5.4.3. Numerical examples

Consider a CP-OFDM setting with IFFT size $N = 256$ and $N_{cp} = N/4$. A rectangular pulse is adopted, i.e., $h_{\mathrm{P}}[n] = 1$ for $0 \leq n \leq L-1$, and zero otherwise. The interpolation filter is an ideal lowpass filter: $H_{\mathrm{I}}(f) = 1$ for $|f| \leq \frac{1}{2T_s}$ and zero otherwise. A total of $K = 129$ active subcarriers are used and located symmetrically about the carrier frequency. The OBR region is $\mathcal{B} = \left\{ \frac{0.25}{T_s} + \frac{\Delta f}{2} \leq |f| \leq \frac{1}{2T_s} \right\}$. We consider a flat weighting function $W(f) = 1$ for $f \in \mathcal{B}$, and zero otherwise. As benchmarks, we consider (i) an unprecoded system with $K_c/2$ null subcarriers at each edge of the passband; (ii) the memoryless ($\ell_0 = 0$) orthogonal design with a redundancy of K_c [123, 124], in which $\boldsymbol{G}[0]$ comprises the $K_d = K - K_c$ least dominant eigenvectors of $\boldsymbol{\Phi}[0]$.

OBR vs. spectral peak

OBR performance depends on the allowed spectral peaks. Better OBR is achieved at the cost of larger undesirable spectral peaks within the passband.

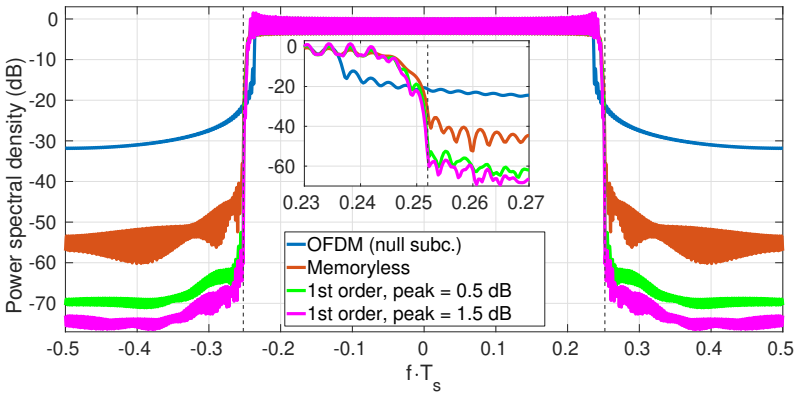

Figure 5.9: PSDs of different precoder designs. $N = 256$, $N_{cp} = N/4$, $K = 129$, $K_d = 121$.

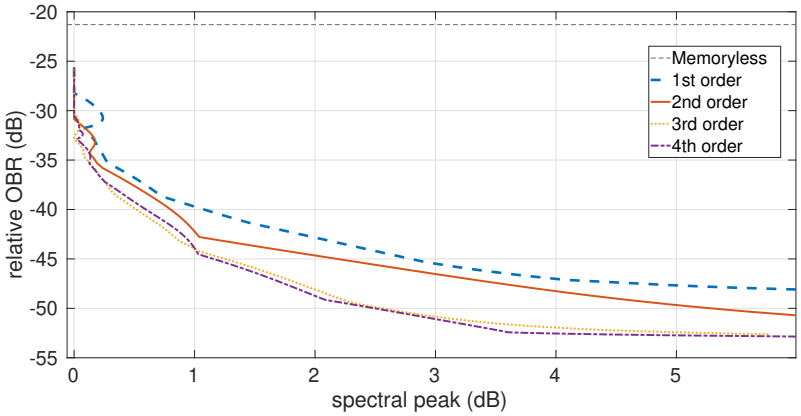

Figure 5.10: OBR (relative to that of the unprecoded system) as a function of spectral peak. $N = 256$, $N_{cp} = N/4$, $K = 129$, $K_d = 121$.

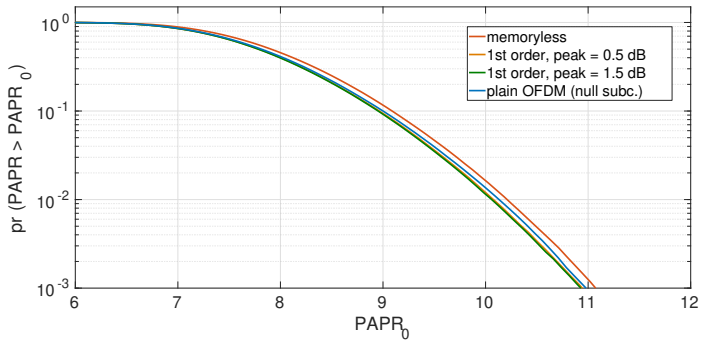

Figure 5.11: PAPR of the proposed design with 16-QAM modulation.

Hence, an OBR/spectral overshoot tradeoff must be found by selecting γ. To illustrate this, consider the application of the memoryless ($\ell_0 = 0$) and first-order ($\ell_0 = 1$) precoders with redundancy $K_c = 8$ in the setting described above. Fig. 5.9 shows the corresponding PSD curves. The total OBR (5.9) of the memoryless precoder is 21.3 dB below that of the unprecoded scheme with null subcarriers; for the 1st-order precoder with spectral peak of 0.5 and 1.5 dB, the corresponding figures are 36.8 and 41.4 dB, respectively. This tradeoff is further illustrated in Fig. 5.10, which shows the relative OBR as a function of the spectral peak[1], for memory precoders up to 4th order. Higher order memory precoders offer better suppression of a given spectral peak. For example, for a peak of 2 dB, 4th-order precoder improves the performance as compared memoryless and lower order designs. Additionally, the proposed-memory precoder design does not suffer from PAPR issues as illustrated in Fig. 5.11.

Similarly in the cognitive radio scenarios, the proposed-memory precoder provides better performance. We consider three different cognitive radio scenarios with the above settings. Scenario 1 has $K = 114$ available subcarriers which are located symmetrically about the PU band. In Scenario 2, the SU can transmit on $K = 122$ subcarriers located asymmetrically about the PU band. Lastly, Scenario 3 contains multiple PU and SU subbands with $K = 107$ active subcarriers for SU. For all the scenarios, the redundancy is set to be $K_{=}12$ and $W(f) = 1$ for $f \in \mathcal{B}$, and zero otherwise. For the unprecoded systems, $K_c = 12$ null subcarriers are used, evenly distributed at the spectrum edges.

Fig. 5.12 shows the PSDs of the proposed first-order ($\ell_0 = 1$) memory precoder along with memoryless design and unprecoded scheme with null subcarriers in the cognitive radio Scenario 1. The memoryless design provides 17.8 dB reduction as compared to that of unprecoded system. On the other hand, the first-order memory precoder with a peak of 0.5 and 2 dB provides 25.6 and 33.9 dB of OBR reduction respectively. Fig. 5.13 shows the PSDs of the three designs in cognitive radio Scenario 2. The memoryless design provides 18.6 dB reduction, whereas the first-order memory precoder with peak of 0.5 dB provides 26.3 dB reduction. Using first-order memory precoder with peak 2 dB, the OBR reduction can be further increased to 35.1 dB. Finally, the cognitive radio Scenario 3 is shown in Fig. 5.14. The introduction of memory improves the OBR performance and provides better protection to the PU subbands. Particularly, in terms of OBR reduction, first-order memory precoder with peak of 0.5 and 2 dB provides 16.8 and 23.1 dB of OBR reduction respectively, as compared to the memoryless design which provides 10.77 dB.

[1]The memoryless precoder does not actually generate spectral peaks, but we show its OBR value for reference in Fig. 5.10.

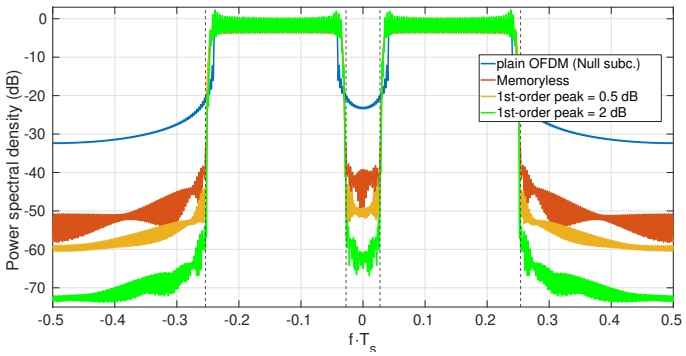

Figure 5.12: PSDs of different precoder designs in cognitive radio Scenario 1. $N = 256$, $N_{cp} = N/4$, $K = 114$, $K_c = 12$.

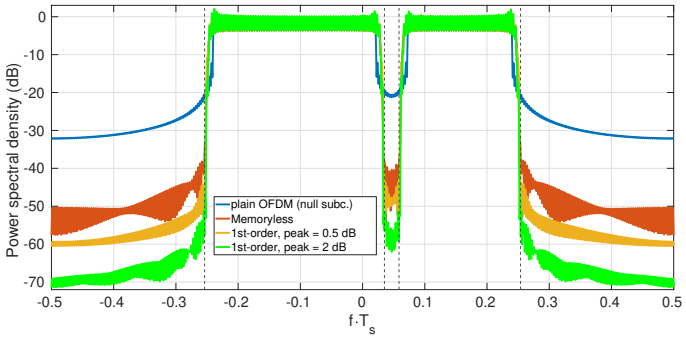

Figure 5.13: PSDs of different precoder designs in cognitive radio Scenario 2. $N = 256$, $N_{cp} = N/4$, $K = 122$, $K_c = 12$.

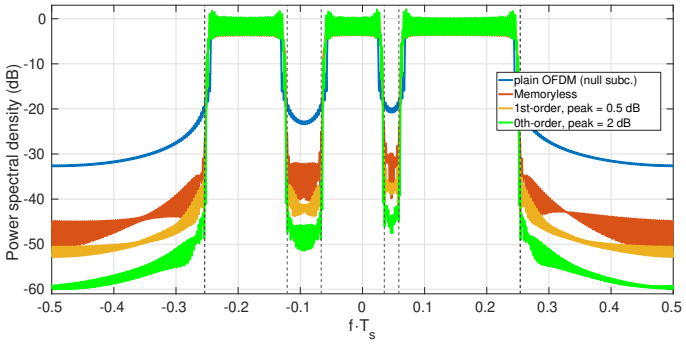

Figure 5.14: PSDs of different precoder designs in cognitive radio Scenario 3. $N = 256$, $N_{cp} = N/4$, $K = 107$, $K_c = 12$.

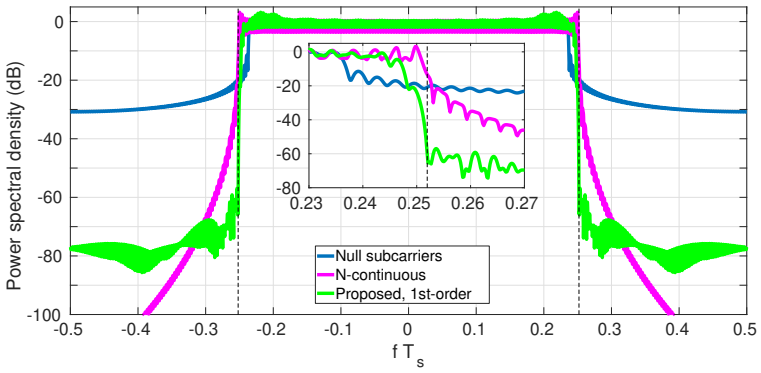

Figure 5.15: PSDs of different designs. $N = 256$, $N_{cp} = N/4$, $K = 129$, $K_d = 121$. Spectral peak is 3.2 dB for N-continuous and proposed precoders.

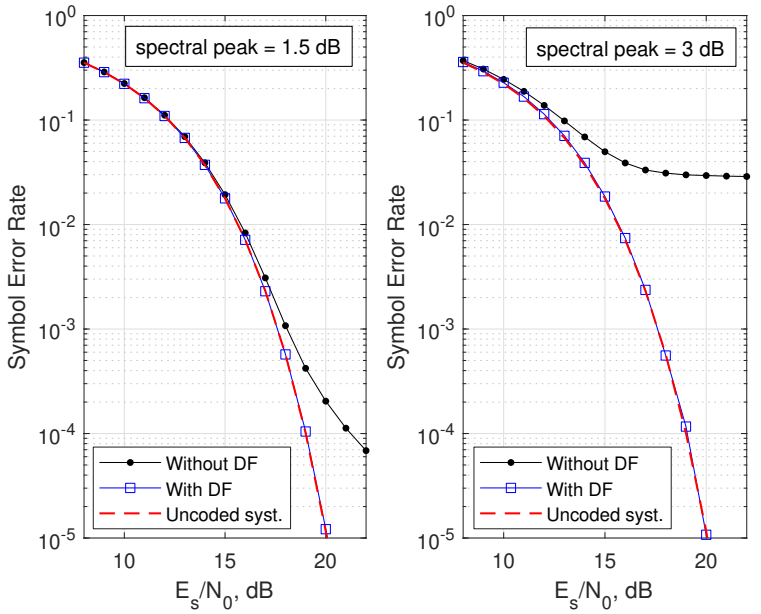

Figure 5.16: SER of 1st-order memory precoder for 16-QAM in AWGN channel. $N = 256$, $N_{cp} = N/4$, $K = 129$, $K_d = 121$.

To compare with other designs incorporating memory, consider the same parameter values as of Fig. 5.9. The N-continuous precoder from [127] imposes K_c continuity conditions at the boundaries of each OFDM block. The PSD, which can be computed as outlined in [151], yields a relative OBR of only -8.8 dB, with a spectral peak of 3.2 dB. Its PSD is shown in Fig. 5.15, together with that of the proposed precoder (order $\ell_0 = 1$) adjusted to yield the same spectral peak value. Although the N-continuous precoder achieves very low PSD values far away from the passband, the proposed design yields a much sharper PSD near the passband edges. The

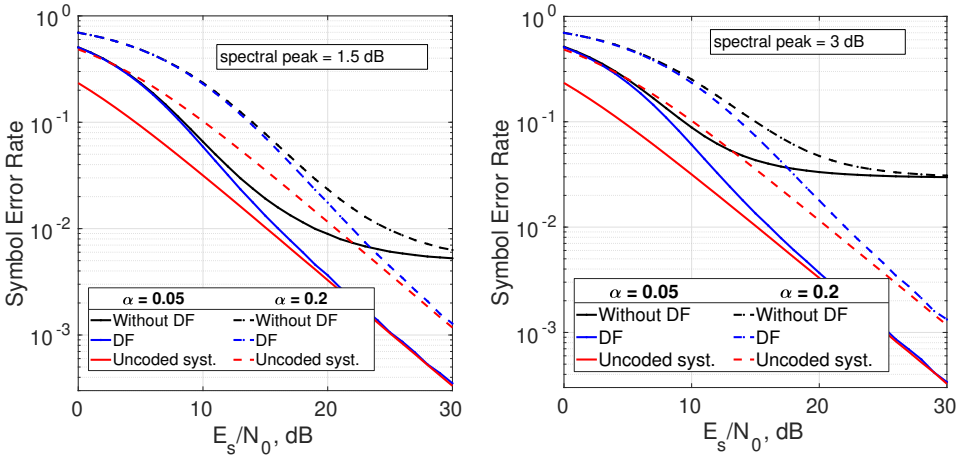

Figure 5.17: SER of 1st-order memory precoder for 16-QAM in multipath channel. $N = 256$, $N_{cp} = N/4$, $K = 129$, $K_d = 121$.

performance of the N-continuous precoder can be improved by increasing the number of continuity conditions K_c, at the expense of spectral efficiency and larger spectral peaks. Thus, the only way to control the spectral peak level in the N-continuous design is by changing its redundancy, whereas the proposed design can achieve different levels of spectral peak by adjusting the regularization parameter γ.

Symbol error rate

The impact of precoding at the receiver is illustrated now. Fig. 5.16 shows the SER attained in AWGN channel (with the same settings as for Fig. 5.15) with the DF-based decoder (5.32), and also with a reduced-complexity decoder which directly estimates the data as $\hat{\boldsymbol{d}}[m] = \text{DEC}\{\boldsymbol{G}^H[0]\boldsymbol{r}[m]\}$. Although this reduced-complexity decoder exhibits an error floor, it may be an attractive choice in low-distortion (i.e., small spectral peak) scenarios. On the other hand, the DF-based decoder successfully removes the inter-block interference introduced by the precoder. Although one may expect some SER degradation due to error propagation, we have only observed this effect for very large spectral peak values. A similar behavior is seen in multipath channel, where DF-based decoder effectively eliminates the inter-block interference that was caused by the precoding process. Fig. 5.17 shows the SER (in the same settings as above) in multipath channel. A N_{cp} tap channel (equal to CP length) is considered with exponential power delay profiles with two decaying constant $\alpha = 0.05$ and $\alpha = 0.2$. The channel taps are random, zero mean Gaussian, and uncorrelated, with independent channel realizations for different OFDM symbols. There is some

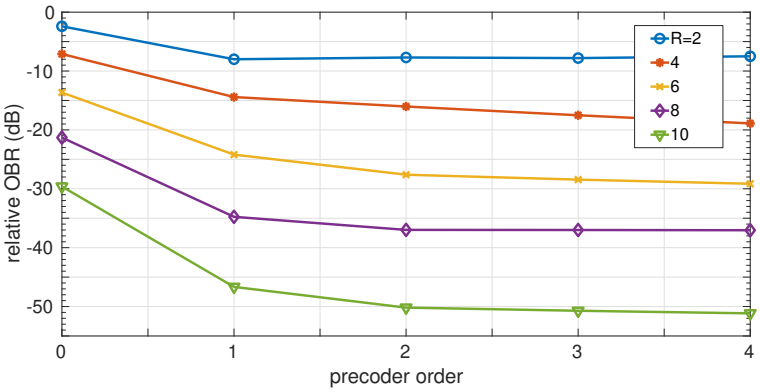

Figure 5.18: OBR (relative to that of the unprecoded system) of the proposed design, for different values of order ℓ_0 and redundancy K_c. Spectral peak is set to 1 dB in all cases.

SER degradation for a low SNR, but at high SNR levels, the DF decoder can be effective in reducing interference and mitigating SER degradation, thereby bridging the SER gap to the uncoded system.

Effect of precoder order

For a memoryless precoder, the only way to improve performance is to increase redundancy, at the expense of sacrificing spectral efficiency. With the introduction of memory, this degradation can be ameliorated at the cost of additional computational complexity. To illustrate this fact, Fig. 5.18 shows the relative OBR as a function of memory precoder order ℓ_0, and for different redundancy values K_c, for 1-dB spectral peak, using the same settings as for Fig. 5.15. Clearly, for a given redundancy K_c, performance improves as the precoder order is increased; however, the performance gain eventually saturates, since the contribution of faraway symbols becomes less significant. The savings in spectral efficiency obtained with memory precoding can be seen in Fig. 5.18: for example, the performance of the memoryless precoder with $K_c = 10$ (efficiency $\frac{119}{129} = 92.25\%$) can be achieved with a fourth-order precoder and $K_c = 6$ (95.35%). This trend also holds for other CP lengths, as seen in Table 5.1.

Fig. 5.19 shows the singular values of the precoding matrices $\boldsymbol{G}[\ell]$ for $\ell \geq 0$, for $K_c = 8$ and different precoder orders. It is clear that these matrices can be well approximated by low-rank ones, with the corresponding computational savings when performing the matrix-vactor products $\boldsymbol{G}[\ell]\boldsymbol{d}[m-\ell]$ at the transmitter, see (5.2), or $\boldsymbol{G}[\ell]\hat{\boldsymbol{d}}[m-\ell]$ at the receiver, as in (5.32).

N_{cp}	$N/32$				
$K_c \setminus \ell_0$	0	1	2	3	4
2	-3.1	-8.7	-8.5	-7.8	-8.0
4	-9.8	-19.1	-20.3	-20.7	-21.2
6	-18.4	-30.9	-32.1	-32.6	-32.9
8	-26.1	-42.0	-43.6	-44.6	-45.7
10	-38.9	-55.7	-57.9	-59.0	-59.9
N_{cp}	$N/16$				
$K_c \setminus \ell_0$	0	1	2	3	4
2	-2.6	-8.7	-8.3	-7.5	-7.8
4	-8.3	-18.5	-19.7	-19.3	-19.3
6	-16.7	-29.3	-29.4	-30.8	-32.2
8	-25.2	-40.6	-42.0	-43.7	-43.8
10	-33.4	-53.1	-55.8	-57.5	-58.6
N_{cp}	$N/8$				
$K_c \setminus \ell_0$	0	1	2	3	4
2	-2.3	-8.7	-8.0	-7.5	-7.4
4	-7.2	-16.2	-17.5	-18.4	-18.9
6	-14.8	-26.0	-28.4	-29.2	-29.3
8	-23.4	-36.4	-40.6	-41.4	-43.2
10	-32.0	-50.2	-51.2	-51.7	-54.5

Table 5.1: Relative OBR (in dB) of memory precoders for different orders, redundancies, and CP lengths. $N = 256$, $K = 129$. Spectral peak is set to 1 dB in all cases.

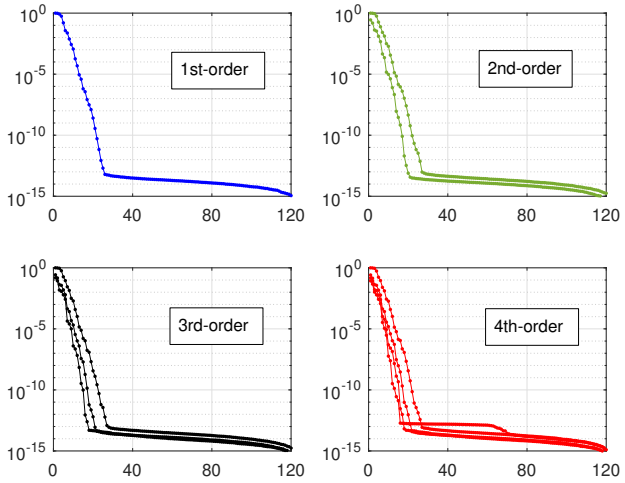

Figure 5.19: Singular values of precoding matrices $\{\boldsymbol{G}_\ell,\ 1 \leq \ell \leq \ell_0\}$. $N = 256$, $N_{cp} = N/4$, $K = 129$, $K_c = 8$. Spectral peak is set to 1 dB in all cases.

5.5. Conclusion

This chapter presented two novel memory-based spectral precoding techniques to reduce out-of-band radiation. A standard memoryless design pays a steep price in spectral efficiency. The introduction of memory alleviates this tradeoff without sacrificing more spectrum at the cost of additional computational complexity at the transmitter. The proposed designs allow to specify the frequency region of interest and to weight the influence of out-of-band emission. Simulation results show that the proposed memory AIC and orthogonal memory precoder designs improve the OBR performance as compared to memoryless AIC and memoryless orthogonal designs respectively. Moreover, the proposed memory orthogonal design shows improvement over other memory-orthogonal designs, such as the N-continuous design from [127].

Chapter 6

Conclusions and Future Work

Orthogonal Frequency Division Multiplexing (OFDM) is a modulation technique widely used in modern digital communication systems. It divides a high-speed data stream into multiple lower-speed subcarriers that are orthogonal to each other, providing several advantages such as its ability to handle multipath interference, high spectral efficiency, and suitability for Multiple-Input Multiple-Output (MIMO) systems. OFDM is extensively used in modern communication systems such as digital television, wireless LANs, and cellular networks. The Third Generation Partnership Project (3GPP) has also chosen it for the 5G new radio (5G-NR) interface.

However, OFDM has some inherent drawbacks, such as sensitivity to frequency offset errors, large sidelobes, and high Peak-to-Average Power Ratio (PAPR). Hence, it is necessary to minimize spectral leakage and PAPR while improving data rates and efficiency to support diverse scenarios in 5G. This thesis focuses on the problem of large sidelobes causing high out-of-band radiation, which is critical for the coexistence of different services and scenarios in 5G and cognitive radio networks. Therefore, the goal is to minimize the radiated power efficiently, reducing adjacent channel interference. Several OBR reduction techniques have been proposed in literature, each with its advantages and drawbacks. The performance of an OBR reduction technique is measured by its ability to suppress out-of-band emissions and key performance indicators (KPIs) such as computational complexity, spectral efficiency, in-band distortion, and spectrum overshoot. The thesis presents various OFDM sidelobe reduction (OBR) techniques to suppress the unwanted emissions.

Chapter 2 introduced a novel time-domain technique to address the problem of OBR in OFDM systems. Although traditional windowing methods are effective in reducing out-of-band radiation, they often rely on fixed ad hoc window functions and lack the flexibility to optimize performance for a given frequency region. In contrast, the proposed technique provides the user with the flexibility to minimize OBR within a specific frequency region, allowing for the assignment of different weights to different subregions. This feature is particularly advantageous in mitigating internumerology interference in 5G systems. The proposed optimal window design is computed offline, resulting in the same online computational complexity as other windowing techniques.

Chapter 3 proposed two innovative designs for spectral precoding, which aim to minimize out-of-band radiation (OBR) in OFDM systems, and thereby prevent adjacent channel interference. Since precoding will introduce signal distortion, appropriate decoding is required at the receiver side. The proposed designs allow for flexible trade-offs between OBR reduction, precoding/decoding complexity, and receiver error rate. This is achieved by a user-selectable parameter that controls the allowable distortion on data subcarriers. An iterative decoding technique is suggested for the receiver, with the number of iterations increasing with the amount of distortion allowed at the transmitter. A significant advantage of the proposed design is that the distortion on each data subcarrier can be individually specified, which can greatly reduce the computational complexity of the receiver. Additionally, the resulting precoding matrices are typically of very low rank, which makes the online implementation of both the precoder and decoder computationally efficient.

In Chapter 4, we introduced a new design that employs both spectral precoding and windowing simultaneously to minimize radiated power. While both, spectral precoding and windowing, are effective at reducing power, they typically come at the cost of reduced throughput and increased computational complexity. By combining these techniques, we show that it is possible to achieve sidelobe suppression comparable to that of standard precoding, while maintaining the same throughput with significantly less online complexity. The proposed design for jointly computing precoder and window coefficients can be performed offline, and can be flexibly adjusted to emphasize suppression over a user-selectable frequency range.

Finally, Memory-based spectral precoding techniques were presented in Chapter 5. Standard memoryless designs pay a steep price in spectral efficiency. The introduction of memory alleviates this tradeoff without sacrificing more spectrum at the cost of additional computational complexity at the transmitter. The proposed designs allow to specify the frequency

region of interest and to weight the influence of out-of-band emission. It is shown that the proposed memory AIC and orthogonal memory precoder designs improve the OBR performance as compared to memoryless AIC and memoryless orthogonal designs respectively.

Now we will discuss some future work related to the topics covered in the previous chapters. The optimal window design discussed in Chapter 2 optimizes the edge samples of the window to reduce out-of-band radiation while leaving the central samples untouched to maintain transparency at the receiver. To further improve OBR performance, we may consider incorporating the central samples into the optimization process, which may involve allowing some distortion in these samples. However, this approach may result in a loss of transparency in the design, which would require appropriate decoding at the receiver to prevent SER degradation. Therefore, further research is needed to determine the best approach for incorporating the central samples into the window design to improve the OBR performance. Additionally, an appropriate decoder needs to be designed to ensure that the benefits of the optimized window design are fully realized in terms of reduced out-of-band radiation and improved OBR performance.

Chapter 3 introduces frequency domain spectral precoder designs for sidelobe suppression, which allow for some distortion in the subcarriers to achieve OBR reduction. The level of distortion on the data subcarriers can be controlled through a user-selectable parameter, while the ability to specify the distortion on each subcarrier individually significantly reduces computational complexity. As shown in Chapter 3, performance can be further improved using a distortion profile, where an arbitrary distortion profile was considered. This demonstrates that a carefully designed distortion profile has the potential to enhance the OBR performance of the spectral precoder. Therefore, the design of a distortion profile warrants further study and investigation in order to optimize OBR performance.

The joint window and precoder design presented in Chapter 4 employs both windowing and spectral precoding techniques to efficiently shape the spectrum. The optimal window design from Chapter 2 is utilized for windowing, while two precoding techniques, namely Active Interference Cancellation (AIC) and orthogonal precoding, are employed for spectral precoding. AIC is simple and transparent at the receiver, but has limited OBR performance, while orthogonal precoding has good OBR performance, but suffers from high complexity. By combining these techniques, the joint design achieves significant online complexity reduction while maintaining good OBR performance. It is worthwhile to investigate whether the flexible spectral precoder designs from Chapter 3 can further enhance the joint window and precoder design by improving OBR performance or reducing online

complexity. Therefore, exploring the integration of the spectral precoder designs from Chapter 3 into the joint window and precoder design represents another promising avenue of research.

The inclusion of memory in Chapter 5 has enhanced the OBR performance compared to the memoryless design. The results indicate that this performance boost does not require sacrificing more spectrum but comes at the expense of additional complexity. Considering the advantages of memory, it would be intriguing to explore the possibility of integrating memory into the flexible spectral precoder introduced in Chapter 3. It is crucial to investigate how memory can be incorporated into the flexible spectral precoder design to improve its performance. Furthermore, since spectral precoder designs are not transparent at the receiver end, an appropriate decoder must also be developed to minimize the SER degradation.

Appendix A

Solution to optimal window design (2.8)

Consider the minimization problem (2.8) of the optimal window design; and let the pulse be $\boldsymbol{h} = [\boldsymbol{h}_1^T \quad \boldsymbol{h}_2^T \quad \boldsymbol{h}_3^T]^T$, where $\boldsymbol{h}_1$ and $\boldsymbol{h}_3$ are the H left and right edge samples, respectively, of the shaping pulse, and $\boldsymbol{h}_2$ comprises the central $L - H$ samples. Thus, the cost function in (2.8) becomes

$$\boldsymbol{h}^H \boldsymbol{Z} \boldsymbol{h} = [\boldsymbol{h}_1^H \quad \boldsymbol{h}_2^H \quad \boldsymbol{h}_3^H] \begin{bmatrix} \boldsymbol{Z}_{11} & \boldsymbol{Z}_{12} & \boldsymbol{Z}_{13} \\ \boldsymbol{Z}_{12}^H & \boldsymbol{Z}_{22} & \boldsymbol{Z}_{23} \\ \boldsymbol{Z}_{13}^H & \boldsymbol{Z}_{23}^H & \boldsymbol{Z}_{33} \end{bmatrix} \begin{bmatrix} \boldsymbol{h}_1 \\ \boldsymbol{h}_2 \\ \boldsymbol{h}_3 \end{bmatrix} \tag{A.1}$$

where the matrix $\boldsymbol{Z}$ is of size $((L+H) \times (L+H))$. The subblocks $\boldsymbol{Z}_{11}, \boldsymbol{Z}_{13}$ and $\boldsymbol{Z}_{33}$ have size $(H \times H)$, $\boldsymbol{Z}_{12}$ and $\boldsymbol{Z}_{23}$ have dimensions $(H \times L - H)$ and $(L - H \times H)$ respectively, and $\boldsymbol{Z}_{22}$ has size $(L - H \times L - H)$. Now note that the constraint $\boldsymbol{D}^H \boldsymbol{h} = \mathbf{1}$ is equivalent to $\boldsymbol{h}_2 = \mathbf{1}$. Let us define the following:

$$\boldsymbol{h}_0 = \begin{bmatrix} \boldsymbol{h}_1 \\ \boldsymbol{h}_3 \end{bmatrix}, \quad \boldsymbol{\vartheta} = \begin{bmatrix} \boldsymbol{Z}_{11} & \boldsymbol{Z}_{13} \\ \boldsymbol{Z}_{13}^H & \boldsymbol{Z}_{33} \end{bmatrix}, \quad \boldsymbol{\varrho} = \begin{bmatrix} \boldsymbol{Z}_{12} \\ \boldsymbol{Z}_{23}^H \end{bmatrix}$$

then (A.1) becomes

$$\boldsymbol{h}^H \boldsymbol{Z} \boldsymbol{h} = \boldsymbol{h}_0^H \boldsymbol{\vartheta} \boldsymbol{h}_0 + \boldsymbol{h}_0^H \boldsymbol{\varrho} \mathbf{1} + \mathbf{1}^H \boldsymbol{\varrho}^H \boldsymbol{h}_0 + \mathbf{1}^H \boldsymbol{Z}_{22} \mathbf{1} \tag{A.2}$$

which is a convex quadratic function of $\boldsymbol{h}_0$. Then, taking the gradient of (A.2) and equating it to zero, the minimizer is found as

$$\boldsymbol{h}_0 = -\boldsymbol{\vartheta}^{-1} \boldsymbol{\varrho} \mathbf{1}. \tag{A.3}$$

Appendix B

Solution to problem (3.7) using GSVD

Consider the problem in (3.7):

$$\min_{\boldsymbol{Q}} \operatorname{tr}\{\boldsymbol{G}^H \boldsymbol{A}_W \boldsymbol{G}\} \quad \text{s.to} \begin{cases} \operatorname{tr}\{\boldsymbol{G}^H \boldsymbol{A}_T \boldsymbol{G}\} & \leq & \beta P_{\text{ref}}, \\ \boldsymbol{S}\boldsymbol{P} + \boldsymbol{T}\boldsymbol{Q} & = & \boldsymbol{G}. \end{cases} \tag{B.1}$$

The unconstrained minimizer of the cost function in problem in (B.1) is given by

$$\hat{\boldsymbol{Q}} = -(\boldsymbol{T}^H \boldsymbol{A}_W \boldsymbol{T})^{-1}(\boldsymbol{T}^H \boldsymbol{A}_W \boldsymbol{S}\boldsymbol{P}). \tag{B.2}$$

If the corresponding transmit power satisfies $P_{LS} = tr\{\boldsymbol{G}^H(\hat{\boldsymbol{Q}})\boldsymbol{A}_T\boldsymbol{G}(\hat{\boldsymbol{Q}})\} \leq \beta P_{\text{ref}}$, then $\hat{\boldsymbol{Q}}$ is the solution to the problem (B.1). On the other hand, if $P_{LS} > \beta P_{\text{ref}}$, then the unconstrained solution (B.2) is not feasible, and at the solution of (B.1) the constraint must hold with equality. To proceed further, let us write the cost function in (B.1) as:

$$\begin{aligned} \operatorname{tr}\{\boldsymbol{G}^H \boldsymbol{A}_W \boldsymbol{G}\} = &\operatorname{tr}\{\boldsymbol{Q}^H \boldsymbol{T}^H \boldsymbol{A}_W \boldsymbol{T}\boldsymbol{Q}\} + 2 \operatorname{tr} Re\{\boldsymbol{Q}^H \boldsymbol{T}^H \boldsymbol{A}_W \boldsymbol{S}\boldsymbol{P}\} \\ &+ \operatorname{tr}\{\boldsymbol{P}^H \boldsymbol{S}^H \boldsymbol{A}_W \boldsymbol{S}\boldsymbol{P}\} \end{aligned} \tag{B.3}$$

The contribution of the data subcarriers to the total power and to the leaked power in band $\mathcal{B}$ can be denoted as:

$$P_{d_{\mathcal{B}}} = \operatorname{tr}\{\boldsymbol{P}^H \boldsymbol{S}^H \boldsymbol{A}_W \boldsymbol{S}\boldsymbol{P}\}, \text{ and } P_{d_{\mathcal{T}}} = \operatorname{tr}\{\boldsymbol{P}^H \boldsymbol{S}^H \boldsymbol{A}_T \boldsymbol{S}\boldsymbol{P}\}. \tag{B.4}$$

Partition $\boldsymbol{P}$ and $\boldsymbol{Q}$ column-wise as

$$\boldsymbol{P} = [\boldsymbol{p}_1\ \boldsymbol{p}_2\ \cdots\ \boldsymbol{p}_{K_d}], \qquad \boldsymbol{Q} = [\boldsymbol{q}_1\ \boldsymbol{q}_2\ \cdots\ \boldsymbol{q}_{K_d}]. \tag{B.5}$$

The objective problem (B.1) can be rewritten as

$$\begin{aligned} \min_{\boldsymbol{q}_i} \quad & P_{d_{\mathcal{B}}} + \sum_{i=1}^{K_d} \left[\boldsymbol{q}_i^H \boldsymbol{T}^H \boldsymbol{A}_W \boldsymbol{T} \boldsymbol{q}_i + 2Re\Big\{ \boldsymbol{q}_i^H (\boldsymbol{T}^H \boldsymbol{A}_W \boldsymbol{S} \boldsymbol{p}_i) \Big\} \right] \\ s.to \quad & P_{d_{\mathcal{T}}} + \sum_{i=1}^{K_d} \left[\boldsymbol{q}_i^H \boldsymbol{T}^H \boldsymbol{A}_T \boldsymbol{T} \boldsymbol{q}_i + 2Re\Big\{ \boldsymbol{q}_i^H (\boldsymbol{T}^H \boldsymbol{A}_T \boldsymbol{S} \boldsymbol{p}_i) \Big\} \right] = \beta P_{\text{ref}} \end{aligned} \tag{B.6}$$

Consider the generalized singular value decomposition (GSVD) [157, Ch. 12] of the following matrices:

$$(\boldsymbol{T}^H \boldsymbol{A}_W \boldsymbol{T})^{1/2} = \boldsymbol{U}_W \boldsymbol{D}_W \boldsymbol{X}^H, \qquad (\boldsymbol{T}^H \boldsymbol{A}_T \boldsymbol{T})^{1/2} = \boldsymbol{U}_T \boldsymbol{D}_T \boldsymbol{X}^H \tag{B.7}$$

where $(\cdot)^{1/2}$ denotes the Hermitian square root matrix, $\boldsymbol{U}_W$, $\boldsymbol{U}_T$ are unitary, $\boldsymbol{D}_W$, $\boldsymbol{D}_T$ are diagional and positive semidefinite with $\boldsymbol{D}_W^2 + \boldsymbol{D}_T^2 = \boldsymbol{I}$, and $\boldsymbol{X}$ is invertible. Let us introduce the following matrices:

$$\boldsymbol{\Xi} = \boldsymbol{X}^{-1} \boldsymbol{T}^H \boldsymbol{A}_W \boldsymbol{S} \boldsymbol{P}, \qquad \boldsymbol{\Theta} = \boldsymbol{X}^{-1} \boldsymbol{T}^H \boldsymbol{A}_T \boldsymbol{S} \boldsymbol{P} \tag{B.8}$$

and denote their i-th columns as $\boldsymbol{\Xi}_i$ and $\boldsymbol{\Theta}_i$. Then (B.6) becomes,

$$\begin{aligned} \min_{\boldsymbol{q}_i} \quad & P_{d_{\mathcal{B}}} + \sum_{i=1}^{K_d} \left[\boldsymbol{q}_i^H \boldsymbol{X} \boldsymbol{D}_W^2 \boldsymbol{X}^H \boldsymbol{q}_i + 2Re\Big\{ \boldsymbol{q}_i^H \boldsymbol{X} \boldsymbol{\Xi}_i \Big\} \right] \\ s.to \quad & P_{d_{\mathcal{T}}} + \sum_{i=1}^{K_d} \left[\boldsymbol{q}_i^H \boldsymbol{X} \boldsymbol{D}_T^2 \boldsymbol{X}^H \boldsymbol{q}_i + 2Re\Big\{ \boldsymbol{q}_i^H \boldsymbol{X} \boldsymbol{\Theta}_i \Big\} \right] = \beta P_{\text{ref}} \end{aligned} \tag{B.9}$$

Using the gradient of the corresponding Lagrangian with respect to $\boldsymbol{q}_j$ and equating to zero, the optimum value of the parameters must satisfy the following conditions for $1 \leq j \leq K_d$, along with the power constraint in (B.9),

$$\boldsymbol{X} \boldsymbol{D}_W^2 \boldsymbol{X}^H \boldsymbol{q}_j + \boldsymbol{X} \boldsymbol{\Xi}_j + \lambda (\boldsymbol{X} \boldsymbol{D}_T^2 \boldsymbol{X}^H \boldsymbol{q}_j + \boldsymbol{X} \boldsymbol{\Theta}_j) = \boldsymbol{0} \tag{B.10}$$

where λ is the Lagrange multiplier. The solution to (B.10) is found to be

$$\boldsymbol{q}_j = -\boldsymbol{X}^{-H} (\boldsymbol{D}_W^2 + \lambda \boldsymbol{D}_T^2)^{-1} (\boldsymbol{\Xi}_j + \lambda \boldsymbol{\Theta}_j) \tag{B.11}$$

for $j = 1, \cdots, K_d$. The value of the Lagrange multiplier can be obtained by substituting (B.11) in the power constraint expression in (B.9) and solving the resulting equation for λ. The total transmit power in (B.9) becomes

$$\begin{aligned} P_T \;=\; & P_{d_{\mathcal{T}}} + \operatorname{tr}\Big\{ (\boldsymbol{\Xi} + \lambda \boldsymbol{\Theta})^H (\boldsymbol{D}_W^2 + \lambda \boldsymbol{D}_T^2)^{-1} \boldsymbol{D}_T^2 (\boldsymbol{D}_W^2 + \lambda \boldsymbol{D}_T^2)^{-1} (\boldsymbol{\Xi} + \lambda \boldsymbol{\Theta}) \Big\} \\ & -2Re \operatorname{tr}\Big\{ (\boldsymbol{\Xi} + \lambda \boldsymbol{\Theta})^H (\boldsymbol{D}_W^2 + \lambda \boldsymbol{D}_T^2)^{-1} \boldsymbol{\Theta} \Big\} \end{aligned} \tag{B.12}$$

Let $\boldsymbol{\xi}_i^H$ and $\boldsymbol{\theta}_i^H$ denote the i-th rows of $\boldsymbol{\Xi}$ and $\boldsymbol{\Theta}$. Similarly, let $d_{W,i}$ and $d_{T,i}$ denote the ith diagonal element of $\boldsymbol{D}_W$ and $\boldsymbol{D}_T$ respectively. Note

that for any $n \times m$ matrices $\boldsymbol{B}$ with rows $\boldsymbol{b}_1^H, \boldsymbol{b}_2^H, \cdots, \boldsymbol{b}_n^H$ and $\boldsymbol{C}$ with rows $\boldsymbol{c}_1^H, \boldsymbol{c}_2^H, \cdots, \boldsymbol{c}_n^H$, and $n \times n$ diagonal $\boldsymbol{D}$ with diagonal elements $d_1, d_2, \cdots, d_n$, one has $\mathrm{tr}\{\boldsymbol{B}^H \boldsymbol{D} \boldsymbol{C}\} = \sum_{k=1}^{n} d_k (\boldsymbol{c}_k^H \boldsymbol{b}_k)$. Then, (B.12) can be written as

$$P_T = P_{d_\mathcal{T}} + \sum_{i=1}^{K_c} \left[\frac{\|d_{T,i}^2 \boldsymbol{\xi}_i - d_{W,i}^2 \boldsymbol{\theta}_i\|^2}{d_{T,i}^2 (d_{W,i}^2 + \lambda d_{T,i}^2)^2} - \frac{\|\boldsymbol{\theta}_i\|^2}{d_{T,i}^2} \right]. \tag{B.13}$$

In particular, we can write the constraint $P_T = \beta P_{\mathrm{ref}}$ as

$$f(\lambda) = \sum_{i=1}^{K_c} \left[\frac{\|d_{T,i}^2 \boldsymbol{\xi}_i - d_{W,i}^2 \boldsymbol{\theta}_i\|^2}{d_{T,i}^2 (d_{W,i}^2 + \lambda d_{T,i}^2)^2} \right] = c \tag{B.14}$$

where $c = \beta P_{\mathrm{ref}} - P_{d_\mathcal{T}} + \sum_{i=1}^{K_c} \left[\frac{\|\boldsymbol{\theta}_i\|^2}{d_{T,i}^2} \right]$.

Note that:

- For $\lambda = 0$, one has $f(0) = \sum_{i=1}^{K_c} \left[\frac{\|d_{T,i}^2 \boldsymbol{\xi}_i - d_{W,i}^2 \boldsymbol{\theta}_i\|^2}{d_{T,i}^2 (d_{W,i}^2)^2} \right]$, and the transmit power $P_T = P_{d_\mathcal{T}} + \sum_{i=1}^{K_c} \left[\frac{\|d_{T,i}^2 \boldsymbol{\xi}_i - d_{W,i}^2 \boldsymbol{\theta}_i\|^2}{d_{T,i}^2 (d_{W,i}^2)^2} - \frac{\|\boldsymbol{\theta}_i\|^2}{d_{T,i}^2} \right]$ is that of unconstrained solution where $\hat{\boldsymbol{Q}}$ is from (B.2). Since we are assuming this solution is unfeasible, it follows that $f(0) > c > 0$.
- $f(\lambda)$ goes to zero as λ goes to infinity.
- the derivative of $f(\lambda)$ is negative i.e., $f'(\lambda) < 0$ for all $\lambda \geq 0$.

These facts show that $f(\lambda)$ is monotonically decreasing in λ for $\lambda \geq 0$ and that the equation $f(\lambda) = c$ has single solution which can be efficiently computed by means of, e.g., the bisection method [163].

Appendix C

Solution to problem (3.8)

Consider the problem in (3.8):

$$\min_{\boldsymbol{P}} \operatorname{tr}\{\boldsymbol{G}^H \boldsymbol{A}_W \boldsymbol{G}\} \quad \text{s.to} \begin{cases} ||\boldsymbol{P} - \boldsymbol{I}_{K_d}||_F^2 & \leq & K_d\epsilon, \\ \boldsymbol{S}\boldsymbol{P} + \boldsymbol{T}\boldsymbol{Q} & = & \boldsymbol{G}. \end{cases} \tag{C.1}$$

The *unconstrained* solution to the problem (C.1) is given by

$$\hat{\boldsymbol{P}} = -(\boldsymbol{S}^H \boldsymbol{A}_W \boldsymbol{S})^{-1}(\boldsymbol{S}^H \boldsymbol{A}_W \boldsymbol{T}\boldsymbol{Q}). \tag{C.2}$$

If the total distotion satisfies $\eta(\hat{\boldsymbol{P}}) = ||\hat{\boldsymbol{P}} - \boldsymbol{I}_{K_d}||_F^2 \leq K_d\epsilon$, then $\hat{\boldsymbol{P}}$ is the solution to the problem (C.1). Alternatively, if $\eta(\hat{\boldsymbol{P}}) > K_d\epsilon$, then the unconstrained solution (C.2) is not feasible, and at the solution of (C.1) the constraint must hold with equality. Problem (C.1) has a constraint with special structure which allows to solve it without using the GSVD. Instead one can use the EVD, as shown below. The cost function in (B.1) can be written as:

$$\begin{aligned} \operatorname{tr}\{\boldsymbol{G}^H \boldsymbol{A}_W \boldsymbol{G}\} &= \operatorname{tr}\{\boldsymbol{P}^H \boldsymbol{S}^H \boldsymbol{A}_W \boldsymbol{S}\boldsymbol{P}\} + 2\operatorname{tr} Re\{\boldsymbol{P}^H \boldsymbol{S}^H \boldsymbol{A}_W \boldsymbol{T}\boldsymbol{Q}\} \\ &\quad + \operatorname{tr}\{\boldsymbol{Q}^H \boldsymbol{T}^H \boldsymbol{A}_W \boldsymbol{T}\boldsymbol{Q}\} \end{aligned} \tag{C.3}$$

Consider the EVD $\boldsymbol{S}^H \boldsymbol{A}_W \boldsymbol{S} = \boldsymbol{U}\boldsymbol{D}\boldsymbol{U}^H$ with $\boldsymbol{U}$ unitary, $\boldsymbol{D}$ diagonal nonnegative. Let d_i be the eigenvalues (i.e., the diagonal elements of $\boldsymbol{D}$). Let $\boldsymbol{B} = \boldsymbol{U}^H \boldsymbol{S}^H \boldsymbol{A}_W \boldsymbol{T}\boldsymbol{Q}\boldsymbol{U}$, then we can rewrite (C.3) as

$$\operatorname{tr}\{\boldsymbol{G}^H \boldsymbol{A}_W \boldsymbol{G}\} = P_{d_{\mathcal{B}}} + \operatorname{tr}\{\boldsymbol{P}^H \boldsymbol{U}\boldsymbol{D}\boldsymbol{U}^H \boldsymbol{P}\} + 2Re\operatorname{tr}\{\boldsymbol{P}^H \boldsymbol{U}\boldsymbol{B}\boldsymbol{U}^H\} \tag{C.4}$$

where $P_{d_{\mathcal{B}}} = \operatorname{tr}\{\boldsymbol{Q}^H \boldsymbol{T}^H \boldsymbol{A}_W \boldsymbol{T}\boldsymbol{Q}\}$. The constraint in (C.1) can be rewritten as

$$||\boldsymbol{P} - \boldsymbol{I}||_F^2 = \operatorname{tr}\{\boldsymbol{P}^H \boldsymbol{P}\} - 2Re\operatorname{tr}\{\boldsymbol{P}^H\} + K_d \tag{C.5}$$

Equating the gradient of the Lagrangian to zero, and using the fact that $\boldsymbol{U}$ is unitary:

$$\boldsymbol{P} = -\boldsymbol{U}(\boldsymbol{D} + \lambda \boldsymbol{I})^{-1}(\boldsymbol{B} - \lambda \boldsymbol{I})\boldsymbol{U}^H, \tag{C.6}$$

where λ is the Lagrange multiplier. Substituting this value of $\boldsymbol{P}$ in the constraint, after some algebra we obtain:

$$f(\lambda) = K_d \epsilon \tag{C.7}$$

where

$$f(\lambda) = \sum_{i=1}^{K_d} \frac{\|\boldsymbol{e}_i^H(\boldsymbol{D} + \boldsymbol{B})\|^2}{(d_i + \lambda)^2}. \tag{C.8}$$

Note that:

- $f(0) = \|\hat{\boldsymbol{P}} - \boldsymbol{I}\|_F^2$, where $\hat{\boldsymbol{P}}$ is the unconstrained solution from (C.2). Since we are assuming this solution is unfeasible, it follows that $f(0) > K_d\epsilon > 0$.
- $f(\lambda)$ goes to zero as λ goes to infinity.
- $f'(\lambda) < 0$ for all $\lambda \geq 0$.

These three facts show that the equation $f(\lambda) = K_d\epsilon$ has a single solution in $\lambda \geq 0$.

Appendix D

Low-rank approximation

Let $\boldsymbol{A} \in \mathbb{R}^{m\times n}$ be any matrix, with singular value decomposition (SVD) given by $\mathbf{A} = \boldsymbol{U}\boldsymbol{\Sigma}\boldsymbol{V}^H$, if $\boldsymbol{U} \in \mathbb{R}^{m\times m}$, $\boldsymbol{V} \in \mathbb{R}^{n\times n}$, then $\boldsymbol{\Sigma}$ must be $m \times n$. The matrices $\boldsymbol{U}$ and $\boldsymbol{V}$ are orthogonal matrices, with the columns of $\boldsymbol{U}$ being the left singular vectors of $\boldsymbol{A}$, and the columns of $\boldsymbol{V}$ being the right singular vectors of $\boldsymbol{A}$. $\boldsymbol{\Sigma}$ is a diagonal matrix with singular values $\sigma_1 \geq \sigma_2 \geq \cdots \geq \sigma_k \geq 0$ on the diagonal where $k = \min(m, n)$. Thus, $\operatorname{rank}(\boldsymbol{A}) = r \leq k$, i.e., $\sigma_r > 0$ and $\sigma_{r+1} = \sigma_{r+2} = \cdots = \sigma_k = 0$.

The SVD of $\boldsymbol{A}$ can also be interpreted as a sum of rank-one matrices, which yields $\mathbf{A} = \sum_{i=1}^{r} \boldsymbol{u}_i \sigma_i \boldsymbol{v}_i^H$, where σ_i are the singular values of $\boldsymbol{A}$, and $\boldsymbol{u}_i$ and $\boldsymbol{v}_i$ are the corresponding left and right singular vectors, respectively. The Eckart–Young theorem [164] states that

$$\min_{\operatorname{rank}(\boldsymbol{B})=\ell} \|\boldsymbol{A} - \boldsymbol{B}\|_q = \begin{cases} \sigma_{\ell+1}, & q = 2, \\ \Big(\sum_{i=\ell+1}^{r} \sigma_i^2 \Big)^{1/2}, & q = F. \end{cases} \tag{D.1}$$

The 2-norm (also known as spectral norm) of a matrix is the largest singular value, and Frobenius norm (similar to the Euclidean norm) is defined as the square root of the sum of the squares of the elements of the matrix. The best rank-ℓ approximation to $\boldsymbol{A}$ in both the 2-norm and the Frobenius norm is given by the truncated SVD

$$\mathbf{A}_\ell = \boldsymbol{U}_\ell \boldsymbol{\Sigma}_\ell \boldsymbol{V}_\ell^H, \tag{D.2}$$

where

$$\begin{aligned} \boldsymbol{U}_\ell &= \boldsymbol{U}_{:,1:\ell}, \\ \boldsymbol{V}_\ell &= \boldsymbol{V}_{:,1:\ell}, \\ \boldsymbol{\Sigma}_\ell &= \operatorname{diag}(\sigma_1, \sigma_2, \cdots, \sigma_\ell). \end{aligned}$$

Appendix E

Solution to problem (3.13)

Consider the problem (3.13) for a fixed $\boldsymbol{Q}$ and $\widetilde{\boldsymbol{p}}_i$ for all $i \neq \ell$, i.e., the minimization is carried out with respect to $\widetilde{\boldsymbol{p}}_\ell$ only: in this way, an LSQI problem is obtained, whose only constraint is $\| \widetilde{\boldsymbol{p}}_\ell - \boldsymbol{e}_\ell\|^2 \leq \epsilon_\ell$, where $\widetilde{\boldsymbol{p}}_\ell \triangleq \boldsymbol{P}^H \boldsymbol{e}_\ell$. This optimization problem can be written as

$$\min_{\widetilde{\boldsymbol{p}}_\ell} \mathrm{tr}\{\boldsymbol{G}^H \boldsymbol{A}_W \boldsymbol{G}\} \quad \text{s.to} \begin{cases} \|\widetilde{\boldsymbol{p}}_\ell - \boldsymbol{e}_\ell\|^2 & \leq & \epsilon_\ell \\ \boldsymbol{S}\boldsymbol{P} + \boldsymbol{T}\boldsymbol{Q} & = & \boldsymbol{G}, \end{cases} \tag{E.1}$$

for $\ell = \{1, \cdots, K_d\}$. In order to proceed further, let us write the cost in (E.1) explicitly in terms of the optimization variable. Let us introduce the following matrices:

$$\boldsymbol{B} = \boldsymbol{S}^H \boldsymbol{A}_W \boldsymbol{S} \qquad \text{and} \qquad \boldsymbol{C} = \boldsymbol{S}^H \boldsymbol{A}_W \boldsymbol{T}\boldsymbol{Q}, \tag{E.2}$$

so that the cost in (E.1) becomes,

$$\mathrm{tr}\{\boldsymbol{G}^H \boldsymbol{A}_W \boldsymbol{G}\} = \mathrm{tr}\{\boldsymbol{Q}^H \boldsymbol{T}^H \boldsymbol{A}_W \boldsymbol{T}\boldsymbol{Q}\} + \mathrm{tr}\{\boldsymbol{P}^H \boldsymbol{C}\} + \mathrm{tr}\{\boldsymbol{C}^H \boldsymbol{P}\} + \mathrm{tr}\{\boldsymbol{P}^H \boldsymbol{B}\boldsymbol{P}\} \tag{E.3}$$

To proceed further, let us write the (E.3) in terms of the optimization variable $\widetilde{\boldsymbol{p}}_\ell$. The first term in (E.3) does not depend on $\boldsymbol{P}$. Note that for any $n \times m$ matrices $\boldsymbol{X}$ with rows $\boldsymbol{x}_1^H, \boldsymbol{x}_2^H, \cdots, \boldsymbol{x}_n^H$ and $\boldsymbol{Z}$ with rows $\boldsymbol{Z}_1^H, \boldsymbol{Z}_2^H, \cdots, \boldsymbol{Z}_n^H$, and $n \times n$ diagonal $\boldsymbol{Y}$ with diagonal elements $y_1, y_2, \cdots, y_n$, one has $\mathrm{tr}\{\boldsymbol{X}^H \boldsymbol{Z}\} = \sum_{k=1}^n (\boldsymbol{x}_k^H \boldsymbol{z}_k)$. Then the second term in (E.3) can be expressed as

$$\mathrm{tr}\{\boldsymbol{P}^H \boldsymbol{C}\} = \sum_{j=1}^{K_d} \widetilde{\boldsymbol{c}}_j^H \widetilde{\boldsymbol{p}}_j \tag{E.4}$$

where $\tilde{\boldsymbol{c}}_j \triangleq \boldsymbol{C}^H \boldsymbol{e}_\ell$. The third term is the conjugate of the second one:

$$\mathrm{tr}\{\boldsymbol{C}^H \boldsymbol{P}\} = \sum_{j=1}^{K_d} \widetilde{\boldsymbol{p}}_j^H \widetilde{\boldsymbol{c}}_j. \tag{E.5}$$

The fourth term can be written as

$$\mathrm{tr}\{\boldsymbol{P}^H\boldsymbol{B}\boldsymbol{P}\} = \sum_{j=1}^{K_d} \boldsymbol{p}_j^H \boldsymbol{B}\boldsymbol{p}_j = \sum_{j=1}^{K_d}\sum_{i=1}^{K_d}\sum_{k=1}^{K_d} p_{kj}^*\; b_{ki}\; p_{ij}, \tag{E.6}$$

where $b_{ki} = \boldsymbol{e}_k^T\boldsymbol{B}\boldsymbol{e}_j$, $\boldsymbol{p}_j \triangleq \boldsymbol{P}\boldsymbol{e}_j$ and $p_{ij} \triangleq \boldsymbol{e}_i^T\boldsymbol{P}\boldsymbol{e}_j$. For any given ℓ with $1 \le \ell \le K_d$, we can write (E.6) in four terms as

$$\begin{aligned}\mathrm{tr}\{\boldsymbol{P}^H\boldsymbol{B}\boldsymbol{P}\} = &\sum_{j=1}^{K_d}\sum_{i\neq\ell}\sum_{k\neq\ell} p_{kj}^*\; b_{ki}\; p_{ij} + \sum_{j=1}^{K_d} b_{\ell\ell}\;|p_{\ell j}|^2 \\ &+ \sum_{j=1}^{K_d}\sum_{i\neq\ell} p_{\ell j}^*\; b_{\ell i}\; p_{ij} + \sum_{j=1}^{K_d}\sum_{k\neq\ell} p_{kj}^*\; b_{k\ell}\; p_{\ell j}\end{aligned} \tag{E.7}$$

Note that $\tilde{\boldsymbol{p}}_\ell = [p_{\ell 1}\; p_{\ell 2}\; \cdots\; p_{\ell K_d}]^H$. Therefore, it is seen that the first term in the right-hand side of (E.7) does not depend on $\widetilde{\boldsymbol{p}}_\ell$. The second and third terms can be respectively written as

$$\sum_{j=1}^{K_d} p_{\ell j}^*\, b_{\ell\ell}\, p_{\ell j} = b_{\ell\ell}\|\widetilde{\boldsymbol{p}}_\ell\|^2, \qquad \sum_{j=1}^{K_d}\sum_{i\neq\ell} p_{\ell j}^*\, b_{\ell i}\, p_{ij} = \widetilde{\boldsymbol{p}}_\ell^H\bar{\boldsymbol{P}}_\ell^T\widetilde{\boldsymbol{b}}_\ell, \tag{E.8}$$

where $\widetilde{\boldsymbol{b}}_\ell = \boldsymbol{B}^T\boldsymbol{e}_\ell$, and $\bar{\boldsymbol{P}}_\ell$ is equal to $\boldsymbol{P}$ with its ℓth row zeroed out, thus $\bar{\boldsymbol{P}}_\ell$ does not depend on $\widetilde{\boldsymbol{p}}_\ell$. The fourth term is the conjugate of the third term. Therefore, (E.7) becomes

$$\mathrm{tr}\{\boldsymbol{P}^H\boldsymbol{B}\boldsymbol{P}\} = \sum_{j=1}^{K_d}\sum_{i\neq\ell}\sum_{k\neq\ell} p_{kj}^*\, b_{ki}\, p_{ij} + b_{\ell\ell}\|\widetilde{\boldsymbol{p}}_\ell\|^2 + \widetilde{\boldsymbol{p}}_\ell^H\bar{\boldsymbol{P}}_\ell^T\widetilde{\boldsymbol{b}}_\ell + \widetilde{\boldsymbol{b}}_\ell^H\bar{\boldsymbol{P}}_\ell^*\widetilde{\boldsymbol{p}}_\ell \tag{E.9}$$

Consequently, for each $1 \le \ell \le K_d$, (E.3) can be rewritten as

$$\mathrm{tr}\{\boldsymbol{G}^H\boldsymbol{A}_W\boldsymbol{G}\} = \gamma_\ell + (\widetilde{\boldsymbol{c}}_\ell + \bar{\boldsymbol{P}}_\ell^T\widetilde{\boldsymbol{b}}_\ell)^H\widetilde{\boldsymbol{p}}_\ell + \widetilde{\boldsymbol{p}}_\ell^H(\widetilde{\boldsymbol{c}}_\ell + \bar{\boldsymbol{P}}_\ell^T\widetilde{\boldsymbol{b}}_\ell) + b_{\ell\ell}\widetilde{\boldsymbol{p}}_\ell^H\widetilde{\boldsymbol{p}}_\ell \tag{E.10}$$

where γ_ℓ does not depend on $\widetilde{\boldsymbol{p}}_\ell$. The optimization problem (E.1) can be rewritten as

$$\min_{\widetilde{\boldsymbol{p}}_\ell} \quad 2Re\{(\widetilde{\boldsymbol{c}}_\ell + \bar{\boldsymbol{P}}_\ell^T\widetilde{\boldsymbol{b}}_\ell)^H\widetilde{\boldsymbol{p}}_\ell\} + b_{\ell\ell}\widetilde{\boldsymbol{p}}_\ell^H\widetilde{\boldsymbol{p}}_\ell \quad \text{s.to} \quad \|\widetilde{\boldsymbol{p}}_\ell - \boldsymbol{e}_\ell\|^2 \le \epsilon_\ell \tag{E.11}$$

The unconstrained solution of problem (E.11) is given by

$$\widetilde{\boldsymbol{p}}_\ell = -\frac{\boldsymbol{f}_\ell}{b_{\ell\ell}}, \tag{E.12}$$

where $\boldsymbol{f}_\ell = \widetilde{\boldsymbol{c}}_\ell + \bar{\boldsymbol{P}}_\ell^T\widetilde{\boldsymbol{b}}_\ell$. The solution given by (E.12) is feasible only if $\boldsymbol{f}_\ell^H\boldsymbol{f}_\ell + b_{\ell\ell}^2 + 2b_{\ell\ell}Re\{\boldsymbol{e}_\ell^H\boldsymbol{f}_\ell\} \le b_{\ell\ell}^2\epsilon_\ell$. Otherwise, at the the solution of (E.11)

the constraint must hold with equality. Using Lagrange multiplier λ , the corresponding gradient of the Lagrangian can be written as

$$b_{\ell\ell}\widetilde{\boldsymbol{p}_\ell} + \boldsymbol{f}_\ell + \lambda(\widetilde{\boldsymbol{p}_\ell} - \boldsymbol{e}_\ell) \tag{E.13}$$

Equating the gradient (E.13) to zero, the solution can be found to be

$$\widetilde{\boldsymbol{p}_\ell} = -\frac{\boldsymbol{f}_\ell - \lambda \boldsymbol{e}_\ell}{(\lambda + b_{\ell\ell})} \tag{E.14}$$

The value of Lagrange multiplier can be found by substituting (E.14) in the constraint $\|\tilde{\boldsymbol{p}}_\ell - \boldsymbol{e}_\ell\|^2 = \epsilon_\ell$ of (E.11). A quadratic equation in λ is obtained, which has two solutions, and the one that gives the minimum value of the cost of (E.11) is used. The resulting value of Lagrange multiplier is

$$\lambda = \frac{1}{\sqrt{\epsilon_\ell}}||\boldsymbol{f}_\ell + b_{\ell\ell}\boldsymbol{e}_\ell|| - b_{\ell\ell} \tag{E.15}$$

Substituting the value of Lagrange multiplier (E.15) in (E.14), the constrained solution to (E.11) can be compactly written as

$$\widetilde{\boldsymbol{p}_\ell} = \boldsymbol{e}_\ell - \frac{\sqrt{\epsilon_\ell}(\boldsymbol{f}_\ell + b_{\ell\ell}\boldsymbol{e}_\ell)}{\|\boldsymbol{f}_\ell + b_{\ell\ell}\boldsymbol{e}_\ell\|}. \tag{E.16}$$

Bibliography

[1] "IMT traffic estimates for the years 2020 to 2030." document ITU-RM.2370-0, 2015.

[2] "5G NR, physical channels and modulation; TS38.211 : version 16.2.0 (Release 16)," 2020.

[3] "Ericsson mobility report." Sweden, Ericsson, 2019.

[4] E. Dahlman, S. Parkvall, and J. Skold, *5G NR: The Next Generation Wireless Access Technology*. London, UK: Academic Press, 2018.

[5] G. A. Akpakwu, B. J. Silva, G. P. Hancke, and A. M. Abu-Mahfouz, "A survey on 5G networks for the internet of things: Communication technologies and challenges," *IEEE Access*, vol. 6, pp. 3619–3647, 2018.

[6] O. O. Erunkulu, A. M. Zungeru, C. K. Lebekwe, M. Mosalaosi, and J. M. Chuma, "5G mobile communication applications: A survey and comparison of use cases," *IEEE Access*, vol. 9, pp. 97251–97295, 2021.

[7] A. Osseiran, F. Boccardi, V. Braun, K. Kusume, P. Marsch, M. Maternia, O. Queseth, M. Schellmann, H. Schotten, H. Taoka, H. Tullberg, M. A. Uusitalo, B. Timus, and M. Fallgren, "Scenarios for 5G mobile and wireless communications: the vision of the metis project," *IEEE Communications Magazine*, vol. 52, no. 5, pp. 26–35, 2014.

[8] M. Simsek, A. Aijaz, M. Dohler, J. Sachs, and G. Fettweis, "The 5G-enabled tactile internet: Applications, requirements, and architecture," in *2016 IEEE Wireless Communications and Networking Conference*, pp. 1–6, 2016.

[9] "Study on scenarios and requirements for next generation access technologies." 3GPP, Tech Rep, TR38.913, 2022.

[10] M. Bellenger, "FBMC physical layer: a primer," tech. rep., Phydyas report, 2010.

[11] D. R1-162199, "Waveform candidates." Qualcomm Inc., Busan, South Korea, Apr. 2016.

[12] M. Bellanger, "Efficiency of filter bank multicarrier techniques in burst radio transmission," in *2010 IEEE Global Telecommunications Conference GLOBECOM 2010*, pp. 1–4, 2010.

[13] B. Farhang-Boroujeny, "OFDM versus filter bank multicarrier," *IEEE Signal Processing Magazine*, vol. 28, no. 3, pp. 92–112, 2011.

[14] R. Zakaria and D. Le Ruyet, "A novel filter-bank multicarrier scheme to mitigate the intrinsic interference: Application to MIMO systems," *IEEE Transactions on Wireless Communications*, vol. 11, no. 3, pp. 1112–1123, 2012.

[15] C. Kim, K. Kim, Y. H. Yun, Z. Ho, B. Lee, and J.-Y. Seol, "QAM-FBMC: A new multi-carrier system for post-OFDM wireless communications," in *2015 IEEE Global Communications Conference (GLOBECOM)*, pp. 1–6, 2015.

[16] V. Vakilian, T. Wild, F. Schaich, S. ten Brink, and J.-F. Frigon, "Universal-filtered multi-carrier technique for wireless systems beyond LTE," in *2013 IEEE Globecom Workshops (GC Wkshps)*, pp. 223–228, 2013.

[17] V. Vakilian, T. Wild, F. Schaich, S. ten Brink, and J.-F. Frigon, "Universal-filtered multi-carrier technique for wireless systems beyond LTE," in *2013 IEEE Globecom Workshops (GC Wkshps)*, pp. 223–228, 2013.

[18] G. Fettweis, M. Krondorf, and S. Bittner, "GFDM - generalized frequency division multiplexing," in *VTC Spring 2009 - IEEE 69th Vehicular Technology Conference*, pp. 1–4, 2009.

[19] N. Michailow, M. Matthé, I. S. Gaspar, A. N. Caldevilla, L. L. Mendes, A. Festag, and G. Fettweis, "Generalized frequency division multiplexing for 5th generation cellular networks," *IEEE Transactions on Communications*, vol. 62, no. 9, pp. 3045–3061, 2014.

[20] R. Datta, N. Michailow, M. Lentmaier, and G. Fettweis, "GFDM interference cancellation for flexible cognitive radio PHY design," in *2012 IEEE Vehicular Technology Conference (VTC Fall)*, pp. 1–5, 2012.

[21] D. Guimarães, "Contributions to the understanding of the MSK modulation," vol. 11, pp. 1–13, 05 2008.

[22] K. Murota and K. Hirade, "GMSK modulation for digital mobile radio telephony," *IEEE Transactions on Communications*, vol. 29, no. 7, pp. 1044–1050, 1981.

[23] D. Falconer, S. Ariyavisitakul, A. Benyamin-Seeyar, and B. Eidson, "Frequency domain equalization for single-carrier broadband wireless systems," *IEEE Communications Magazine*, vol. 40, no. 4, pp. 58–66, 2002.

[24] G. Berardinelli, K. I. Pedersen, T. B. Sorensen, and P. Mogensen, "Generalized DFT-spread-OFDM as 5G waveform," *IEEE Communications Magazine*, vol. 54, no. 11, pp. 99–105, 2016.

[25] A. Sahin, R. Yang, E. Bala, M. C. Beluri, and R. L. Olesen, "Flexible DFT-s-OFDM: Solutions and challenges," *IEEE Communications Magazine*, vol. 54, no. 11, pp. 106–112, 2016.

[26] G. Berardinelli, F. M. L. Tavares, T. B. Sorensen, P. Mogensen, and K. Pajukoski, "Zero-tail DFT-spread-OFDM signals," in *2013 IEEE Globecom Workshops (GC Wkshps)*, pp. 229–234, 2013.

[27] G. Huang, A. Nix, and S. Armour, "Impact of radio resource allocation and pulse shaping on PAPR of SC-FDMA signals," in *2007 IEEE 18th International Symposium on Personal, Indoor and Mobile Radio Communications*, pp. 1–5, 2007.

[28] J. Abdoli, M. Jia, and J. Ma, "Filtered OFDM: A new waveform for future wireless systems," in *2015 IEEE 16th International Workshop on Signal Processing Advances in Wireless Communications (SPAWC)*, pp. 66–70, 2015.

[29] X. Zhang, M. Jia, L. Chen, J. Ma, and J. Qiu, "Filtered-OFDM - enabler for flexible waveform in the 5th generation cellular networks," in *2015 IEEE Global Communications Conference (GLOBECOM)*, pp. 1–6, 2015.

[30] G. Matz, D. Schafhuber, K. Grochenig, M. Hartmann, and F. Hlawatsch, "Analysis, optimization, and implementation of low-interference wireless multicarrier systems," *IEEE Transactions on Wireless Communications*, vol. 6, no. 5, pp. 1921–1931, 2007.

[31] H. Boelcskei, "Efficient design of pulse-shaping filters for OFDM systems," in *Wavelet Applications in Signal and Image Processing VII* (M. A. Unser, A. Aldroubi, and A. F. Laine, eds.), vol. 3813, pp. 625 – 636, International Society for Optics and Photonics, SPIE, 1999.

[32] Z. Zhao, M. Schellmann, Q. Wang, X. Gong, R. Boehnke, and W. Xu, "Pulse shaped OFDM for asynchronous uplink access," in *2015 49th Asilomar Conference on Signals, Systems and Computers*, pp. 3–7, 2015.

[33] M. Huemer, C. Hofbauer, A. Onic, and J. B. Huber, "Design and analysis of UW-OFDM signals," *AEU - International Journal of Electronics and Communications*, vol. 68, no. 10, pp. 958–968, 2014.

[34] A. Sahin, R. Yang, M. Ghosh, and R. L. Olesen, "An improved unique word DFT-spread OFDM scheme for 5G systems," in *2015 IEEE Globecom Workshops (GC Wkshps)*, pp. 1–6, 2015.

[35] H. Lin, "Flexible configured OFDM for 5G air interface," *IEEE Access*, vol. 3, pp. 1861–1870, 2015.

[36] M. Bellanger, "FS-FBMC: A flexible robust scheme for efficient multicarrier broadband wireless access," in *2012 IEEE Globecom Workshops*, pp. 192–196, 2012.

[37] F. Schaich, T. Wild, and Y. Chen, "Waveform contenders for 5G - suitability for short packet and low latency transmissions," in *2014 IEEE 79th Vehicular Technology Conference (VTC Spring)*, pp. 1–5, 2014.

[38] I. Parvez, A. Rahmati, I. Guvenc, A. I. Sarwat, and H. Dai, "A survey on low latency towards 5G: Ran, core network and caching solutions," *IEEE Communications Surveys & Tutorials*, vol. 20, no. 4, pp. 3098–3130, 2018.

[39] G. Wunder, P. Jung, M. Kasparick, T. Wild, F. Schaich, Y. Chen, S. T. Brink, I. Gaspar, N. Michailow, A. Festag, L. Mendes, N. Cassiau, D. Ktenas, M. Dryjanski, S. Pietrzyk, B. Eged, P. Vago, and F. Wiedmann, "5GNOW: non-orthogonal, asynchronous waveforms for future mobile applications," *IEEE Communications Magazine*, vol. 52, no. 2, pp. 97–105, 2014.

[40] M. Van Eeckhaute, A. Bourdoux, P. De Doncker, and F. Horlin, "Performance of emerging multi-carrier waveforms for 5G asynchronous communications," *EURASIP Journal on Wireless Communications and Networking*, vol. 2017, no. 1, 2017.

[41] X. Zhang, L. Chen, J. Qiu, and J. Abdoli, "On the waveform for 5G," *IEEE Communications Magazine*, vol. 54, no. 11, pp. 74–80, 2016.

[42] Q. Zheng, F. Wang, X. Chen, Y. Liu, D. Miao, and Z. Zhao, "Comparison of 5G waveform candidates in high speed scenario," in *2017 XXXIInd General Assembly and Scientific Symposium of the International Union of Radio Science (URSI GASS)*, pp. 1–4, 2017.

[43] R. Gerzaguet, N. Bartzoudis, L. Baltar, V. Berg, J.-B. Doré, D. Ktenas, O. Font-Bach, X. Mestre, M. Payaro, M. Färber, and K. Roth,

"The 5G candidate waveform race: a comparison of complexity and performance," *EURASIP Journal on Wireless Communications and Networking*, vol. 2017, 01 2017.

[44] A. A. Zaidi, R. Baldemair, H. Tullberg, H. Bjorkegren, L. Sundstrom, J. Medbo, C. Kilinc, and I. Da Silva, "Waveform and numerology to support 5G services and requirements," *IEEE Communications Magazine*, vol. 54, no. 11, pp. 90–98, 2016.

[45] G. R. A. Network, "TS38.211: NR; Physical channels and modulation (Release 15)." `https://portal.3gpp.org/desktopmodules/Specifications/SpecificationDetails.aspx?specificationId=3213`, Mar. 2018.

[46] R. W. Chang, "Synthesis of band-limited orthogonal signals for multichannel data transmission," *The Bell System Technical Journal*, vol. 45, no. 10, pp. 1775–1796, 1966.

[47] R. Chang and R. Gibby, "A theoretical study of performance of an orthogonal multiplexing data transmission scheme," *IEEE Transactions on Communication Technology*, vol. 16, no. 4, pp. 529–540, 1968.

[48] M. Zimmerman and A. Kirsch, "The an/gsc-10 (kathryn) variable rate data modem for hf radio," *IEEE Transactions on Communication Technology*, vol. 15, no. 2, pp. 197–204, 1967.

[49] A. Peled and A. Ruiz, "Frequency domain data transmission using reduced computational complexity algorithms," in *ICASSP '80. IEEE International Conference on Acoustics, Speech, and Signal Processing*, vol. 5, pp. 964–967, 1980.

[50] L. Cimini, "Analysis and simulation of a digital mobile channel using orthogonal frequency division multiplexing," *IEEE Transactions on Communications*, vol. 33, no. 7, pp. 665–675, 1985.

[51] J. Bingham, "Multicarrier modulation for data transmission: an idea whose time has come," *IEEE Communications Magazine*, vol. 28, no. 5, pp. 5–14, 1990.

[52] S. Weinstein and P. Ebert, "Data transmission by frequency-division multiplexing using the discrete fourier transform," *IEEE Transactions on Communication Technology*, vol. 19, no. 5, pp. 628–634, 1971.

[53] E. Casas and C. Leung, "OFDM for data communication over mobile radio fm channels. i. analysis and experimental results," *IEEE Transactions on Communications*, vol. 39, no. 5, pp. 783–793, 1991.

[54] ETSI, "Radio broadcasting systems: Digital audio broadcasting (DAB) to mobile, portable and fied receduers." ETS 300401, 1997.

[55] ETSI, "Digital video broadcasting (DVB): Framing structure, channel coding and modulation for digital terrestrial television." EN 300744, 1997.

[56] ETSI, "Broadband radio access networks (BRAN),hiperlan type 2." TR 101683, 2000.

[57] M. S. Yousuf and M. El-Shafei, "Power line communications: An overview - part i," in *2007 Innovations in Information Technologies (IIT)*, pp. 218–222, 2007.

[58] H. Ferreira, H. Grove, O. Hooijen, and J. Vinck, "Power line communications: an overview," pp. 558 – 563 vol.2, 10 1996.

[59] M. S. Yousuf, S. Z. Rizvi, and M. El-Shafei, "Power line communications: An overview - part ii," in *2008 3rd International Conference on Information and Communication Technologies: From Theory to Applications*, pp. 1–6, 2008.

[60] "IEEE standard for low-frequency (less than 500 khz) narrowband power line communications for smart grid applications," *IEEE Std 1901.2-2013*, pp. 1–269, 2013.

[61] "Narrowband orthogonal frequency division multiplexing power line communication transceivers for G3-PLC networks," Aug. 2017.

[62] "Unified high-speed wire-line based home networking transceivers – system architecture and physical layer specification," Noc. 2018.

[63] P. Achaichia, M. Le Bot, and P. Siohan, "Windowed OFDM versus OFDM/OQAM: A transmission capacity comparison in the homeplug av context," in *2011 IEEE International Symposium on Power Line Communications and Its Applications*, pp. 405–410, 2011.

[64] K. M. Rabie, E. Alsusa, A. D. Familua, and L. Cheng, "Constant envelope OFDM transmission over impulsive noise power-line communication channels," in *2015 IEEE International Symposium on Power Line Communications and Its Applications (ISPLC)*, pp. 13–18, 2015.

[65] S. Gault, P. Ciblat, and W. Hachem, "An OFDMA based modem for powerline communications over the low voltage distribution network," in *International Symposium on Power Line Communications and Its Applications, 2005.*, pp. 42–46, 2005.

[66] K. M. Rabie and E. Alsusae, "On improving communication robustness in plc systems for more reliable smart grid applications," *IEEE Transactions on Smart Grid*, vol. 6, no. 6, pp. 2746–2756, 2015.

[67] M. Kuhn, S. Berger, I. Hammerstrom, and A. Wittneben, "Power line enhanced cooperative wireless communications," *IEEE Journal on Selected Areas in Communications*, vol. 24, no. 7, pp. 1401–1410, 2006.

[68] L. Díez, J. A. Cortés, F. J. Cañete, E. Martos-Naya, and S. Iranzo, "A generalized spectral shaping method for OFDM signals," *IEEE Transactions on Communications*, vol. 67, no. 5, pp. 3540–3551, 2019.

[69] M. Jiang and L. Hanzo, "Multiuser MIMO-OFDM for next-generation wireless systems," *Proceedings of the IEEE*, vol. 95, no. 7, pp. 1430–1469, 2007.

[70] H. Bolcskei, "MIMO-OFDM wireless systems: basics, perspectives, and challenges," *IEEE Wireless Communications*, vol. 13, no. 4, pp. 31–37, 2006.

[71] H. Yang, "A road to future broadband wireless access: MIMO-OFDM-based air interface," *IEEE Communications Magazine*, vol. 43, no. 1, pp. 53–60, 2005.

[72] G. Stuber, J. Barry, S. McLaughlin, Y. Li, M. Ingram, and T. Pratt, "Broadband MIMO-OFDM wireless communications," *Proceedings of the IEEE*, vol. 92, no. 2, pp. 271–294, 2004.

[73] H. Sampath, S. Talwar, J. Tellado, V. Erceg, and A. Paulraj, "A fourth-generation MIMO-OFDM broadband wireless system: design, performance, and field trial results," *IEEE Communications Magazine*, vol. 40, no. 9, pp. 143–149, 2002.

[74] A. PAULRAJ, D. GORE, R. NABAR, and H. BOLCSKEI, "An overview of MIMO communications - a key to gigabit wireless," *Proceedings of the IEEE*, vol. 92, no. 2, pp. 198–218, 2004.

[75] L. Lu, G. Y. Li, A. L. Swindlehurst, A. Ashikhmin, and R. Zhang, "An overview of massive MIMO: Benefits and challenges," *IEEE Journal of Selected Topics in Signal Processing*, vol. 8, no. 5, pp. 742–758, 2014.

[76] Y. Wu, X. Gao, S. Zhou, W. Yang, Y. Polyanskiy, and G. Caire, "Massive access for future wireless communication systems," *IEEE Wireless Communications*, vol. 27, no. 4, pp. 148–156, 2020.

[77] T. Jiang and Y. Wu, "An overview: Peak-to-average power ratio reduction techniques for OFDM signals," *IEEE Transactions on Broadcasting*, vol. 54, no. 2, pp. 257–268, 2008.

[78] S. H. Han and J. H. Lee, "An overview of peak-to-average power ratio reduction techniques for multicarrier transmission," *IEEE Wireless Communications*, vol. 12, no. 2, pp. 56–65, 2005.

[79] A. M. Rateb and M. Labana, "An optimal low complexity PAPR reduction technique for next generation OFDM systems," *IEEE Access*, vol. 7, pp. 16406–16420, 2019.

[80] Y. A. Al-Jawhar, K. N. Ramli, A. Mustapha, S. A. Mostafa, N. S. Mohd Shah, and M. A. Taher, "Reducing PAPR with low complexity for 4g and 5G waveform designs," *IEEE Access*, vol. 7, pp. 97673–97688, 2019.

[81] T. Schmidl and D. Cox, "Robust frequency and timing synchronization for OFDM," *IEEE Transactions on Communications*, vol. 45, no. 12, pp. 1613–1621, 1997.

[82] J. van de Beek, M. Sandell, and P. Borjesson, "Ml estimation of time and frequency offset in OFDM systems," *IEEE Transactions on Signal Processing*, vol. 45, no. 7, pp. 1800–1805, 1997.

[83] J. Chen, Y.-c. Wu, S. Ma, and T.-s. Ng, "Ml joint CFO and channel estimation in OFDM systems with timing ambiguity," *IEEE Transactions on Wireless Communications*, vol. 7, no. 7, pp. 2436–2440, 2008.

[84] Y. Yao and G. Giannakis, "Blind carrier frequency offset estimation in SISO, MIMO, and multiuser OFDM systems," *IEEE Transactions on Communications*, vol. 53, no. 1, pp. 173–183, 2005.

[85] A. Al-Dweik, "Robust non data-aided frequency offset estimation technique," in *2004 IEEE 15th International Symposium on Personal, Indoor and Mobile Radio Communications (IEEE Cat. No.04TH8754)*, vol. 2, pp. 1365–1369 Vol.2, 2004.

[86] X. N. Zeng and A. Ghrayeb, "A blind carrier frequency offset estimation scheme for OFDM systems with constant modulus signaling," *IEEE Transactions on Communications*, vol. 56, no. 7, pp. 1032–1037, 2008.

[87] A. Al-Dweik, A. Hazmi, S. Younis, B. Sharif, and C. Tsimenidis, "Carrier frequency offset estimation for OFDM systems over mobile radio channels," *IEEE Transactions on Vehicular Technology*, vol. 59, no. 2, pp. 974–979, 2010.

[88] H. Minn, V. Bhargava, and K. Letaief, "A robust timing and frequency synchronization for OFDM systems," *IEEE Transactions on Wireless Communications*, vol. 2, no. 4, pp. 822–839, 2003.

[89] H. Minn, M. Zeng, and V. Bhargava, "On timing offset estimation for OFDM systems," *IEEE Communications Letters*, vol. 4, no. 7, pp. 242–244, 2000.

[90] D. B. Leeson, "A simple model of feedback oscillator noise spectrum," 1966.

[91] J. Vihriälä, A. A. Zaidi, V. Venkatasubramanian, N. He, E. Tiirola, J. Medbo, E. Lähetkangas, K. Werner, K. Pajukoski, A. Cedergren, and R. Baldemair, "Numerology and frame structure for 5G radio access," in *2016 IEEE 27th Annual International Symposium on Personal, Indoor, and Mobile Radio Communications (PIMRC)*, pp. 1–5, 2016.

[92] A. A. Zaidi, R. Baldemair, V. Moles-Cases, N. He, K. Werner, and A. Cedergren, "OFDM numerology design for 5G new radio to support IoT, eMBB, and MBSFN," *IEEE Communications Standards Magazine*, vol. 2, no. 2, pp. 78–83, 2018.

[93] X. Zhang, L. Zhang, P. Xiao, D. Ma, J. Wei, and Y. Xin, "Mixed numerologies interference analysis and inter-numerology interference cancellation for windowed OFDM systems," *IEEE Transactions on Vehicular Technology*, vol. 67, no. 8, pp. 7047–7061, 2018.

[94] J. Mao, L. Zhang, P. Xiao, and K. Nikitopoulos, "Interference analysis and power allocation in the presence of mixed numerologies," *IEEE Transactions on Wireless Communications*, vol. 19, no. 8, pp. 5188–5203, 2020.

[95] P. Guan, D. Wu, T. Tian, J. Zhou, X. Zhang, L. Gu, A. Benjebbour, M. Iwabuchi, and Y. Kishiyama, "5G field trials: OFDM-based waveforms and mixed numerologies," *IEEE Journal on Selected Areas in Communications*, vol. 35, no. 6, pp. 1234–1243, 2017.

[96] FCC, "Spectrum policy task force report (ET docket no. 02-135)," Nov. 2002.

[97] J. Mitola and G. Maguire, "Cognitive radio: making software radios more personal," *IEEE Personal Communications*, vol. 6, no. 4, pp. 13–18, 1999.

[98] S. Haykin, "Cognitive radio: brain-empowered wireless communications," *IEEE Journal on Selected Areas in Communications*, vol. 23, no. 2, pp. 201–220, 2005.

[99] J. Mitola, "Cognitive radio for flexible mobile multimedia communications," in *1999 IEEE International Workshop on Mobile Multimedia Communications (MoMuC'99) (Cat. No.99EX384)*, pp. 3–10, 1999.

[100] C.-X. Wang, F. Haider, X. Gao, X.-H. You, Y. Yang, D. Yuan, H. M. Aggoune, H. Haas, S. Fletcher, and E. Hepsaydir, "Cellular architecture and key technologies for 5G wireless communication networks," *IEEE Communications Magazine*, vol. 52, no. 2, pp. 122–130, 2014.

[101] "IEEE standard - information technology-telecommunications and information exchange between systems-wireless regional area networks-specific requirements-part 22: Cognitive wireless RAN MAC and PHY specifications: Policies and procedures for operation in the bands that allow spectrum sharing where the communications devices may opportunistically operate in the spectrum of primary service," *IEEE Std 802.22-2019 (Revision of IEEE Std 802.22-2011)*, pp. 1–1465, 2020.

[102] "5G NR, base station (BS) radio transmission and reception; TS38.104: version 15.2.0 (Release 15)," Mar. 2018.

[103] S. Sasipriya and R. Vigneshram, "An overview of cognitive radio in 5G wireless communications," in *2016 IEEE International Conference on Computational Intelligence and Computing Research (ICCIC)*, pp. 1–5, 2016.

[104] X. Huang, J. A. Zhang, and Y. J. Guo, "Out-of-band emission reduction and a unified framework for precoded OFDM," *IEEE Communications Magazine*, vol. 53, no. 6, pp. 151–159, 2015.

[105] T. Weiss, J. Hillenbrand, A. Krohn, and F. Jondral, "Mutual interference in OFDM-based spectrum pooling systems," in *2004 IEEE 59th Vehicular Technology Conference. VTC 2004-Spring (IEEE Cat. No.04CH37514)*, vol. 4, pp. 1873–1877 Vol.4, 2004.

[106] V. Cosovic, I.and Janardhanam, "Sidelobe suppression in OFDM systems," in *Multi-Carrier Spread-Spectrum* (K. Fazel and S. Kaiser, eds.), (Dordrecht), pp. 473–482, Springer Netherlands, 2006.

[107] I. Cosovic and T. Mazzoni, "Suppression of sidelobes in OFDM systems by multiple-choice sequences," *European Transactions on Telecommunications*, vol. 17, no. 6, pp. 623–630, 2006.

[108] I. Cosovic, S. Brandes, and M. Schnell, "Subcarrier weighting: a method for sidelobe suppression in OFDM systems," *IEEE Communications Letters*, vol. 10, no. 6, pp. 444–446, 2006.

[109] R. Kumar and A. Tyagi, "Extended subcarrier weighting for sidelobe suppression in OFDM based cognitive radio," *Wireless Personal Communications*, vol. 87, pp. 779–796, May 2015.

[110] S. Pagadarai, R. Rajbanshi, A. M. Wyglinski, and G. J. Minden, "Sidelobe suppression for OFDM-based cognitive radios using constellation expansion," in *2008 IEEE Wireless Communications and Networking Conference*, pp. 888–893, 2008.

[111] M. M. Naghsh, E. Haj Mirza Alian, S. Khobahi, and O. Rezaei, "A majorization–minimization approach for reducing out-of-band radiations in OFDM systems," *IEEE Communications Letters*, vol. 21, no. 8, pp. 1739–1742, 2017.

[112] S. Brandes, I. Cosovic, and M. Schnell, "Sidelobe suppression in OFDM systems by insertion of cancellation carriers," in *VTC-2005-Fall. 2005 IEEE 62nd Vehicular Technology Conference, 2005.*, vol. 1, pp. 152–156, 2005.

[113] S. Brandes, I. Cosovic, and M. Schnell, "Reduction of out-of-band radiation in OFDM systems by insertion of cancellation carriers," *IEEE Commun. Lett.*, vol. 10, pp. 420–422, Jun. 2006.

[114] J. F. Schmidt, S. Costas-Sanz, and R. López-Valcarce, "Choose your subcarriers wisely: Active interference cancellation for cognitive OFDM," *IEEE J. Emerg. Sel. Topics Circuits Syst.*, vol. 3, pp. 615–625, Dec. 2013.

[115] D. Qu, Z. Wang, and T. Jiang, "Extended active interference cancellation for sidelobe suppression in cognitive radio OFDM systems with cyclic prefix," *IEEE Transactions on Vehicular Technology*, vol. 59, no. 4, pp. 1689–1695, 2010.

[116] H. Yamaguchi, "Active interference cancellation technique for MB-OFDM cognitive radio," in *34th European Microwave Conference, 2004.*, vol. 2, pp. 1105–1108, 2004.

[117] D. Qu, Z. Wang, T. Jiang, and M. Daneshmand, "Sidelobe suppression using extended active interference cancellation with self-interference constraint for cognitive OFDM system," in *2009 Fourth International Conference on Communications and Networking in China*, pp. 1–5, 2009.

[118] J. Van De Beek, "Sculpting the multicarrier spectrum: a novel projection precoder," *IEEE Communications Letters*, vol. 13, no. 12, pp. 881–883, 2009.

[119] J. A. Zhang, X. Huang, A. Cantoni, and Y. J. Guo, "Sidelobe suppression with orthogonal projection for multicarrier systems," *IEEE Transactions on Communications*, vol. 60, no. 2, pp. 589–599, 2012.

[120] A. Tom, A. Sahin, and H. Arslan, "Mask compliant precoder for OFDM spectrum shaping," *IEEE Communications Letters*, vol. 17, no. 3, pp. 447–450, 2013.

[121] S. Kant, G. Fodor, M. Bengtsson, B. Goransson, and C. Fischione, "Low-complexity OFDM spectral precoding," in *2019 IEEE 20th International Workshop on Signal Processing Advances in Wireless Communications (SPAWC)*, pp. 1–5, 2019.

[122] R. Kumar and A. Tyagi, "Computationally efficient mask-compliant spectral precoder for OFDM cognitive radio," *IEEE Transactions on Cognitive Communications and Networking*, vol. 2, no. 1, pp. 15–23, 2016.

[123] R. Xu and M. Chen, "A precoding scheme for DFT-based OFDM to suppress sidelobes," *IEEE Communications Letters*, vol. 13, no. 10, pp. 776–778, 2009.

[124] M. Ma, X. Huang, B. Jiao, and Y. J. Guo, "Optimal orthogonal precoding for power leakage suppression in DFT-based systems," *IEEE Transactions on Communications*, vol. 59, no. 3, pp. 844–853, 2011.

[125] R. Kumar and A. Tyagi, "Orthogonal spectral precoder for minimizing adjacent channel leakage ratio in OFDM based cognitive radio," *Wireless Communications and Mobile Computing*, vol. 16, no. 18, pp. 3332–3339, 2016.

[126] J. van de Beek, "Orthogonal multiplexing in a subspace of frequency well-localized signals," *IEEE Communications Letters*, vol. 14, no. 10, pp. 882–884, 2010.

[127] Y. Zheng, J. Zhong, M. Zhao, and Y. Cai, "A precoding scheme for N-continuous OFDM," *IEEE Communications Letters*, vol. 16, no. 12, pp. 1937–1940, 2012.

[128] J. Van De Beek and F. Berggren, "Out-of-band power suppression in OFDM," *IEEE Communications Letters*, vol. 12, no. 9, pp. 609–611, 2008.

[129] J. van de Beek and F. Berggren, "N-continuous OFDM," *IEEE Communications Letters*, vol. 13, no. 1, pp. 1–3, 2009.

[130] M. Ohta, M. Okuno, and K. Yamashita, "Receiver iteration reduction of an N-continuous OFDM system with cancellation tones," in *2011 IEEE Global Telecommunications Conference - GLOBECOM 2011*, pp. 1–5, 2011.

[131] M. Ohta, A. Iwase, and K. Yamashita, "Improvement of the error characteristics of an N-continuous OFDM system with low data channels by slm," in *2011 IEEE International Conference on Communications (ICC)*, pp. 1–5, 2011.

[132] J. van de Beek and F. Berggren, "EVM-constrained OFDM precoding for reduction of out-of-band emission," in *2009 IEEE 70th Vehicular Technology Conference Fall*, pp. 1–5, 2009.

[133] M. Mohamad, R. Nilsson, and J. van de Beek, "Minimum-EVM N-continuous OFDM," in *2016 IEEE International Conference on Communications (ICC)*, pp. 1–5, 2016.

[134] L. Dan, C. Zhang, J. Yuan, P. Wen, and B. Fu, "Improved N-continuous OFDM using adaptive power allocation," in *2018 IEEE 8th Annual Computing and Communication Workshop and Conference (CCWC)*, pp. 937–940, 2018.

[135] C.-D. Chung, "Correlatively coded OFDM," *IEEE Transactions on Wireless Communications*, vol. 5, no. 8, pp. 2044–2049, 2006.

[136] C.-D. Chung, "Spectrally precoded OFDM," *IEEE Transactions on Communications*, vol. 54, no. 12, pp. 2173–2185, 2006.

[137] C.-D. Chung, "Spectral precoding for rectangularly pulsed OFDM," *IEEE Transactions on Communications*, vol. 56, no. 9, pp. 1498–1510, 2008.

[138] X. Zhou, G. Y. Li, and G. Sun, "Low-complexity spectrum shaping for OFDM-based cognitive radio systems," *IEEE Signal Processing Letters*, vol. 19, no. 10, pp. 667–670, 2012.

[139] J. F. Schmidt, D. Romero, and R. López-Valcarce, "Active interference cancellation for OFDM spectrum sculpting: Linear processing is optimal," *IEEE Commun. Lett.*, vol. 18, pp. 1543–1546, Sep. 2014.

[140] I. V. L. Clarkson, "Orthogonal precoding for sidelobe suppression in DFT-based systems using block reflectors," in *2017 IEEE International Conference on Acoustics, Speech and Signal Processing (ICASSP)*, pp. 3709–3713, 2017.

[141] H. Kawasaki, K. Ishizu, and F. Kojima, "Computationally efficient orthogonal precoding for sidelobe suppression of OFDM signals," in *2018 IEEE International Conference on Communications (ICC)*, pp. 1–6, 2018.

[142] H. Kawasaki, T. Matsumura, K. Ishizu, and F. Kojima, "Low-complexity orthogonal N-continuous precoding for sidelobe suppression of OFDM signals," in *2019 22nd International Symposium on Wireless Personal Multimedia Communications (WPMC)*, pp. 1–6, 2019.

[143] M. Faulkner, "The effect of filtering on the performance of OFDM systems," *IEEE Transactions on Vehicular Technology*, vol. 49, no. 5, pp. 1877–1884, 2000.

[144] H. A. Mahmoud and H. Arslan, "Sidelobe suppression in OFDM-based spectrum sharing systems using adaptive symbol transition," *IEEE Communications Letters*, vol. 12, no. 2, pp. 133–135, 2008.

[145] E. H. M. Alian and P. Mitran, "A phase adjustment approach for interference reduction in OFDM-based cognitive radios," *IEEE Transactions on Wireless Communications*, vol. 12, no. 9, pp. 4668–4679, 2013.

[146] R. Zayani, Y. Medjahdi, H. Shaiek, and D. Roviras, "WOLA-OFDM: A potential candidate for asynchronous 5G," in *2016 IEEE Globecom Workshops (GC Wkshps)*, pp. 1–5, 2016.

[147] S.-Y. Lien, S.-L. Shieh, Y. Huang, B. Su, Y.-L. Hsu, and H.-Y. Wei, "5G new radio: Waveform, frame structure, multiple access, and initial access," *IEEE Communications Magazine*, vol. 55, no. 6, pp. 64–71, 2017.

[148] I. Budiarjo, H. Nikookar, and L. P. Ligthart, "Cognitive radio modulation techniques," *IEEE Signal Processing Magazine*, vol. 25, no. 6, pp. 24–34, 2008.

[149] L. Yu, B. D. Rao, L. B. Milstein, and J. G. Proakis, "Reducing out-of-band radiation of OFDM-based cognitive radios," in *2010 IEEE 11th International Workshop on Signal Processing Advances in Wireless Communications (SPAWC)*, pp. 1–5, 2010.

[150] S. Brandes, I. Cosovic, and M. Schnell, "Techniques for reducing out-of-band radiation in ofdm based transmission systems," *European Transactions on Telecommunications*, vol. 21, no. 2, pp. 142–153, 2010.

[151] R. López-Valcarce, "General form of the power spectral density of multicarrier signals," *IEEE Communications Letters*, vol. 26, no. 8, pp. 1755–1759, 2022.

[152] A. Zaidi, F. Athley, J. Medbo, U. Gustavsson, G. Durisi, and X. Chen, *5G Physical Layer: Principles, Models and Technology Components*. London, UK: Academic Press, 2018.

[153] J. G. Andrews, S. Buzzi, W. Choi, S. V. Hanly, A. Lozano, A. C. K. Soong, and J. C. Zhang, "What will 5G be?," *IEEE J. Sel. Areas Commun.*, vol. 32, pp. 1065–1082, June 2014.

[154] E. Guvenkaya, E. Bala, R. Yang, and H. Arslan, "Time-asymmetric and subcarrier-specific pulse shaping in OFDM-based waveforms," *IEEE Trans. Veh. Technol.*, vol. 64, pp. 5070–5082, Nov 2015.

[155] "IEEE standard for information technology– telecommunications and information exchange between systemslocal and metropolitan area networks– specific requirements–part 11: Wireless lan medium access control (MAC) and physical layer (PHY) specifications–amendment 4: Enhancements for very high throughput for operation in bands below 6 ghz.," *IEEE Std 802.11ac-2013 (Amendment to IEEE Std 802.11-2012, as amended by IEEE Std 802.11ae-2012, IEEE Std 802.11aa-2012, and IEEE Std 802.11ad-2012)*, pp. 1–425, 2013.

[156] M. Rumney, *LTE and the Evolution to 4G Wireless - Design and Measurement Challenges, Second Edition.* John Wiley & Sons, Ltd, 2013.

[157] G. H. Golub and C. F. Van Loan, *Matrix Computations (3rd Ed.).* Baltimore, MD, USA: Johns Hopkins University Press, 1996.

[158] T. Taheri, R. Nilsson, and J. van de Beek, "Hybrid spectral precoding/windowing for low-latency OFDM," in *2017 IEEE 85th Vehicular Technology Conference (VTC Spring)*, pp. 1–5, 2017.

[159] E. Kokiopoulou, J. Chen, and Y. Saad, "Trace optimization and eigenproblems in dimension reduction methods," *Numerical Linear Algebra with Applications*, vol. 18, no. 3, pp. 565–602, 2011.

[160] S.-G. Huang and C.-H. Hwang, "Improvement of active interference cancellation: avoidance technique for OFDM cognitive radio," *IEEE Transactions on Wireless Communications*, vol. 8, no. 12, pp. 5928–5937, 2009.

[161] J. Haber-Kucharsk, E. Haj Mirza Alian, and P. Mitran, "On the reserved sub-carrier approach to achieving N-continuity for side-lobe reduction in OFDM," in *2013 13th Canadian Workshop on Information Theory*, pp. 209–213, 2013.

[162] R. Kumar, K. Hussain, and R. López-Valcarce, "Mask-compliant orthogonal precoding for spectrally efficient OFDM," *IEEE Trans. Commun.*, vol. 69, no. 3, pp. 1990–2001, 2021.

[163] R. Burden, J. Faires, and A. Burden, *Numerical Analysis.* Cengage Learning, 2015.

[164] C. Eckart and G. Young, "The approximation of one matrix by another of lower rank," *Psychometrika*, 1936.